

---

# SPECTRAL FLOW ON THE MANIFOLD OF SPD MATRICES FOR MULTIMODAL DATA PROCESSING

---

A PREPRINT

**Ori Katz**

Viterbi Faculty of Electrical Engineering  
Technion – Israel Institute of Technology, Israel  
orikats@campus.technion.ac.il

**Roy R. Lederman**

Department of Statistics and Data Science  
Yale University  
roy.lederman@yale.edu

**Ronen Talmon**

Viterbi Faculty of Electrical Engineering  
Technion – Israel Institute of Technology, Israel  
ronen@ee.technion.ac.il

September 18, 2020

## ABSTRACT

In this paper, we consider data acquired by multimodal sensors capturing complementary aspects and features of a measured phenomenon. We focus on a scenario in which the measurements share mutual sources of variability but might also be contaminated by other measurement-specific sources such as interferences or noise. Our approach combines manifold learning, which is a class of nonlinear data-driven dimension reduction methods, with the well-known Riemannian geometry of symmetric and positive-definite (SPD) matrices. Manifold learning typically includes the spectral analysis of a kernel built from the measurements. Here, we take a different approach, utilizing the Riemannian geometry of the kernels. In particular, we study the way the spectrum of the kernels changes along geodesic paths on the manifold of SPD matrices. We show that this change enables us, in a purely unsupervised manner, to derive a compact, yet informative, description of the relations between the measurements, in terms of their underlying components. Based on this result, we present new algorithms for extracting the common latent components and for identifying common and measurement-specific components.

**Keywords** Manifold Learning · Multimodal Data Analysis · Riemannian Geometry · Symmetric Positive Definite Matrices ·

## 1 Introduction

Often, a single data acquisition method is not capable of capturing the entire complexity and characteristics of a complex phenomenon, and it may be prone to noise and interferences. Therefore, modern data collection consists of multiple types of sensors. The availability of multimodal data calls for the development of analysis and processing tools, which appropriately combine data from the different sensors and are capable of handling the inherent challenges. One particular challenge is related to the heterogeneity of the data acquired by different modalities; datasets acquired by different sensors may comprise different sources of variability, while only few are relevant to the phenomenon of interest. This particular challenge as well as many others have been the subject of many recent studies on multimodal data fusion [1, 2, 3].

Recently, this problem has been investigated from the view point of manifold learning. Manifold learning is a class of dimension reduction techniques, often kernel-based, which rely on the assumption that the high-dimensional data at hand lie on a low dimensional manifold [4, 5, 6, 7, 8]. The vast majority of manifold learning techniques embed the high dimensional data into a lower dimensional space using the spectral decomposition of a kernel matrix. Of

particular interest are Laplacian eigenmaps [7] and diffusion maps [8], where it is shown that the kernel built from the data approximates the Laplace-Beltrami operator of the underlying manifold. This, combined with the work of Bérard et al. [9] and Jones et al. [10], implies that the constructed embedding encompasses the entire geometric information.

For multimodal data analysis, manifold learning entails particular advantages, since manifold learning methods are unsupervised, data-driven and they require only minimal prior knowledge on the data, circumventing the need to hand-craft specially-designed features and solutions for each specific modality. Indeed, a large body of evidence, e.g., [11, 12, 13, 14, 15], implies that manifold learning facilitates efficient and informative analysis of multimodal data.

In this paper, our main focus is on the problem introduced in [13], consisting of two *aligned* data sets of, possibly multimodal, measurements, residing on two hidden manifolds. These two data sets share mutual components but each might also be contaminated by other measurement-specific components such as interferences or noise. Given the two data sets, our goal is to extract the different components and to characterize whether they are mutual or measurement-specific.

We propose a new approach combining manifold learning with the Riemannian geometry of symmetric and positive-definite (SPD) matrices [16, 17, 18]. The Riemannian geometry of the space of  $n \times n$  SPD matrices, denoted by  $\mathcal{P}(n)$ , is well-known and well-studied. SPD matrices have been shown to be useful features in medical imaging [19], radar signal processing [20, 21] and computer vision applications [22, 23, 24]. In these applications, the constraints induced by the geometric structure were exploited to improve the performance of a multitude of data processing tasks such as interpolation, filtering and completion of missing data. In [18], Pennec proposed to endow the space of SPD matrices with an affine invariant Riemannian metric, which subsequently provided the foundation to many extensions. In [25], the distance induced by this affine invariant metric was used for the classification of EEG signals in brain computer interface (BCI) tasks. In [26], the authors used the geodesic path on  $\mathcal{P}(n)$  between two SPD matrices in order to establish a regularization for tracking covariance matrices of non-stationary time-series. In [27] a new class of probability distributions on the space of SPD matrices, called Riemannian Gaussian distributions, were presented, uncovering the connection between maximum likelihood estimation and the Riemannian center of mass. In [28] the parallel transport along the geodesic path was used to devise an algorithm for unsupervised domain adaptation.

While most studies on SPD matrices focus on covariance matrices, the present work considers the Riemannian geometry of SPD kernel matrices. This facilitates a significant extension of the scope and increases the number of potential applications. For example, in contrast to covariance matrices, SPD kernel matrices can encode nonlinear and local associations and characterize temporal behavior.

In the context of the problem we study, we propose to consider a sequence of SPD matrices along the geodesic path between two SPD kernel matrices that are constructed based on the two given data sets. From this sequence, we construct a representation, which we term *eigenvalues flow diagram*, depicting the variation of the spectra of the matrices along the geodesic path. We show that the variation of the spectra exhibits prototypical characteristics, which are highly informative for the problem at hand. Specifically, we show how the mutual and sensor-specific spectral components can be identified, and how the mutual components can be extracted from the eigenvalues flow diagram.

We test the new approach on simulations and two applications involving real measured data: electronic noise and industrial condition monitoring. Specifically, we demonstrate the characteristics of the eigenvalues flow diagram, and we show how it facilitates an informative spectral analysis.

Our main contributions are as follows. We propose a framework for multimodal data analysis. The proposed framework is unsupervised and data-driven, and does not assume any prior knowledge regarding the modalities of the measurements. The proposed framework combines spectral methods with the Riemannian geometry of SPD matrices, and to the best of our knowledge, it is the first time it is used for multimodal data analysis. We present theoretical analysis and devise concrete algorithms. Our results show, both theoretically and empirically, that the proposed framework successfully manages to provide informative analysis of the measured data such as identifying the sources of variability influencing the measurements and extracting the mutual-relations between these sources. Moreover, it accommodates efficient feature selection, nonlinear filtering, and the recovery of the mutual components.

The remainder of the paper is organized as follows. In section 2 we formulate the problem. In section 3 we provide preliminaries on the Riemannian geometry of SPD matrices and on Diffusion maps. In section 4, we provide an overview of the proposed method using an illustrative toy problem and present a set of algorithms implementing the proposed framework. We demonstrate the results on synthetic data in section 5 and on real measured data in section 6. Finally, in section 7 we conclude and lay out directions for future work.

## 2 Problem formulation

We revisit the problem studied in [13] and in [14]. Consider three intrinsic Riemannian manifolds:  $\mathcal{M}_x$ ,  $\mathcal{M}_y$  and  $\mathcal{M}_z$ . These intrinsic Riemannian manifolds are hidden and are accessed by two measurement functions  $h$  and  $g$ :

$$\begin{aligned} g &: \mathcal{M}_x \times \mathcal{M}_y \rightarrow \mathcal{O}_1 \\ h &: \mathcal{M}_x \times \mathcal{M}_z \rightarrow \mathcal{O}_2 \end{aligned}$$

which are smooth isometric embedding of the respective product manifolds  $\mathcal{M}_x \times \mathcal{M}_y$  and  $\mathcal{M}_x \times \mathcal{M}_z$  into the observable spaces  $\mathcal{O}_1$  and  $\mathcal{O}_2$ . Importantly, the first measurement ignores  $\mathcal{M}_z$  and the second measurement ignores  $\mathcal{M}_y$ . Moreover, the two measurements have a common structure, the intrinsic manifold  $\mathcal{M}_x$ , and each measurement is affected by an additional measurement-specific structure, the intrinsic manifold  $\mathcal{M}_y$  or  $\mathcal{M}_z$ .

Let  $(x_i, y_i, z_i) \in \mathcal{M}_x \times \mathcal{M}_y \times \mathcal{M}_z$  be a realization from some joint distribution defined on the product manifold. This realization is not accessible directly, but gives rise to a pair of aligned measurements  $(s_i^{(1)}, s_i^{(2)})$ , such that  $s_i^{(1)} = g(x_i, y_i)$  and  $s_i^{(2)} = h(x_i, z_i)$ .

Considering  $n$  realizations of the hidden triplets  $\{(x_i, y_i, z_i)\}_{i=1}^n$ , which give rise to two aligned and accessible measurement sets  $\{s_i^{(1)}\}_{i=1}^n$  and  $\{s_i^{(2)}\}_{i=1}^n$ , our main goal is to build an informative representation of the mutual-relationships between the two sets of measurements in an unsupervised fashion. Concretely, we seek a representation from which one could (i) build an embedding of the realizations that represents only the hidden variables  $\{x_i\}_{i=1}^n$  from the common manifold  $\mathcal{M}_x$ , as in [13], (ii) separate and detect both the common and the measurement-specific components, and (iii) devise an unsupervised quality assessment of the measurements based on their number of common and respective measurement-specific components.

We conclude this section with an important remark on the terminology we use throughout the paper. Our approach relies on spectral analysis of samples from  $\mathcal{O}_1$  and  $\mathcal{O}_2$ . We use the term *common (spectral) component* to describe an eigenvector or an eigenvalue that corresponds to  $\mathcal{M}_x$ . We use the term *common eigenvector* to describe an eigenvector shared by the spectral analysis of  $\mathcal{O}_1$  and  $\mathcal{O}_2$ . We assume that a common eigenvector is a common spectral component in our setup, where  $g$  and  $h$  are isometry transformations. Yet, due to various factors, e.g., distortions introduced by the measurement functions  $g$  and  $h$  or different sampling densities, common spectral components may be described also by not strictly common eigenvectors (but rather by similar, not identical eigenvectors). All other spectral components that are not common component, e.g., components corresponding to  $\mathcal{M}_y$  or  $\mathcal{M}_z$ , are termed *measurement-specific components*.

## 3 Preliminaries

### 3.1 On the Riemannian geometry of SPD matrices

The space  $\mathbb{R}^{n \times n}$  is a Hilbert space equipped with the inner product  $\langle \mathbf{A}, \mathbf{B} \rangle = \text{tr}(\mathbf{A}^T \mathbf{B})$ . Let  $\mathcal{S}_n$  denote the set of symmetric matrices in  $\mathbb{R}^{n \times n}$ . A matrix  $\mathbf{K} \in \mathcal{S}_n$  is called an SPD matrix if all its eigenvalues are strictly positive. Let  $\mathcal{P}_n$  denote the subset of SPD matrices, which is an open set in  $\mathcal{S}_n$  and forms a differentiable Riemannian manifold with the following inner product

$$\langle \mathbf{S}_1, \mathbf{S}_2 \rangle_{\mathcal{T}_K \mathcal{P}_n} = \langle \mathbf{K}^{-\frac{1}{2}} \mathbf{S}_1 \mathbf{K}^{-\frac{1}{2}}, \mathbf{K}^{-\frac{1}{2}} \mathbf{S}_2 \mathbf{K}^{-\frac{1}{2}} \rangle \quad (1)$$

where  $\mathcal{T}_K \mathcal{P}_n = \{K\} \times \mathcal{S}_n$  is the tangent space to  $\mathcal{P}_n$  at the point  $\mathbf{K} \in \mathcal{P}_n$ .

The Riemannian manifold  $\mathcal{P}_n$  has a unique geodesic path between any two points  $\mathbf{K}_1, \mathbf{K}_2 \in \mathcal{P}(n)$ , given by [17, Thm 6.1.6]:

$$\gamma(t) = \mathbf{K}_1^{1/2} (\mathbf{K}_1^{-1/2} \mathbf{K}_2 \mathbf{K}_1^{-1/2})^t \mathbf{K}_1^{1/2}, \quad (2)$$

where  $0 \leq t \leq 1$  is a parametrization of the arc-length of the path from the initial point  $\mathbf{K}_1$  ( $t = 0$ ) to the end point  $\mathbf{K}_2$  ( $t = 1$ ).

The manifold of SPD matrices  $\mathcal{P}_n$  entails many useful properties, which make it a popular framework for data analysis [18, 29, 30, 24, 31, 32, 28]. For example, the arc-length of the geodesic path has a closed-form expression, giving rise to the following Riemannian distance

$$\begin{aligned} d_R(\mathbf{K}_1, \mathbf{K}_2) &= \|\log \mathbf{K}_1^{-1/2} \mathbf{K}_2 \mathbf{K}_1^{-1/2}\|_F \\ &= \sqrt{\sum_{i=1}^n \log^2 \left( \lambda_i(\mathbf{K}_1^{-1/2} \mathbf{K}_2 \mathbf{K}_1^{-1/2}) \right)} \end{aligned}$$

where  $\mathbf{K}_1, \mathbf{K}_2 \in \mathcal{P}(n)$ ,  $\|\cdot\|_F$  is the Frobenious norm,  $\log(\mathbf{K})$  is the matrix logarithm, and  $\lambda_i(\mathbf{K})$  is the  $i$ -th eigenvalue of  $\mathbf{K}$ . Additionally, the Logarithmic map and the Exponential map have closed-form expressions, and there are many efficient algorithms for calculating the Riemannian mean (defined using the Fréchet mean) of a set of SPD matrices [31, 33]. For more details on  $\mathcal{P}_n$ , see [17, 18].

### 3.2 Diffusion Maps

Diffusion maps, introduced by Coifman and Lafon [8], is one of the prominent manifold learning methods, which has deep theoretical roots in Riemannian geometry, spectral graph theory, operator theory, and diffusion analysis.

Let  $(\mathcal{M}, d\mu)$  be a measure space, where  $\mathcal{M}$  is a compact smooth Riemannian manifold and  $d\mu(x) = p(x)dx$  is a measure with density  $p(x) \in C^3(\mathcal{M})$ , which is a positive definite function with respect to the volume measure  $dx$  on  $\mathcal{M}$ . Assume that  $\mathcal{M}$  is isometrically embedded in  $\mathbb{R}^d$ , and let  $w_\epsilon : \mathcal{M} \times \mathcal{M} \rightarrow \mathbb{R}$  be a symmetric positive definite kernel given by

$$w_\epsilon(x, y) = \exp\left(-\frac{\|x - y\|^2}{\epsilon}\right)$$

where  $\|\cdot\|$  denotes the Euclidean norm in  $\mathbb{R}^d$ .

Let  $p_\epsilon : \mathcal{M} \rightarrow \mathbb{R}$  be the local measure of the volume, given by

$$p_\epsilon(x) = \int_{\mathcal{M}} w_\epsilon(x, y)p(y)dy$$

and form a new kernel  $k_\epsilon : \mathcal{M} \times \mathcal{M} \rightarrow \mathbb{R}$

$$k_\epsilon(x, y) = \frac{w_\epsilon(x, y)}{p_\epsilon(x)p_\epsilon(y)}$$

This particular kernel normalization allows to mitigate non-uniform distributions (see [8] for details).

Now, apply the weighted graph Laplacian normalization to this kernel and form  $a_\epsilon : \mathcal{M} \times \mathcal{M} \rightarrow \mathbb{R}$

$$a_\epsilon(x, y) = \frac{k_\epsilon(x, y)}{d_\epsilon(x)}$$

where  $d_\epsilon : \mathcal{M} \rightarrow \mathbb{R}$  is given by

$$d_\epsilon(x) = \int_{\mathcal{M}} k_\epsilon(x, y)p(y)dy$$

Define the diffusion operator  $A_\epsilon : L^2(\mathcal{M}, d\mu) \rightarrow L^2(\mathcal{M}, d\mu)$  by

$$A_\epsilon f(x) = \int_{\mathcal{M}} a_\epsilon(x, y)f(y)p(y)dy$$

Theorem 2 in [8] states that the infinite generator corresponding to  $A_\epsilon$  converges to the Laplace-Beltrami operator on  $\mathcal{M}$ , i.e.,

$$\frac{1}{\epsilon}(I - A_\epsilon)f \rightarrow \Delta f \quad (3)$$

in  $L^2$  norm as  $\epsilon \rightarrow 0$ , where  $\Delta$  is the positive semi-definite Laplace-Beltrami operator on  $\mathcal{M}$ , for any smooth function  $f^1$ .

This convergence result implies that  $A_\epsilon$  may be viewed as an approximation of the Laplace-Beltrami operator  $\Delta$ . Since the eigenfunctions of  $\Delta$  bear all the geometric information on the manifold  $\mathcal{M}$  and can be used for embedding the points on the manifold  $x \in \mathcal{M}$  [9, 10], the eigenfunctions of  $A_\epsilon$  may be used for the same purpose.

Suppose that a set  $\{x_i \in \mathcal{M}\}_{i=1}^n \subset \mathbb{R}^d$  of  $n$  points from the manifold is given, sampled from a density  $p(x)$  induced by the measure  $\mu(x)$ . As in [8], we repeat the construction steps described above in a discrete fashion. We build the  $n \times n$  affinity matrix  $\mathbf{W}$  with entries

$$W_{i,j} = \exp\left(-\frac{\|x_i - x_j\|^2}{\epsilon}\right) \quad (4)$$

---

<sup>1</sup>That is  $f$  in the span of the dominant Neumann eigenfunctions of  $\Delta$ .



for  $i, j = 1, \dots, n$ . Then, we apply a two-step normalization. In the first step, we build a diagonal matrix  $\bar{\mathbf{D}} = \text{diag}(\mathbf{W}\mathbf{1})$ , where  $\mathbf{1}$  is a column vector of all ones, and a normalized affinity matrix  $\bar{\mathbf{K}} = \bar{\mathbf{D}}^{-1}\mathbf{W}\bar{\mathbf{D}}^{-1}$ . In the second step, we build another diagonal matrix  $\mathbf{D} = \text{diag}(\bar{\mathbf{K}}\mathbf{1})$ , and form

$$\mathbf{A} = \mathbf{D}^{-1}\bar{\mathbf{K}} \quad (5)$$

The row-stochastic affinity matrix  $\mathbf{A}$  can be viewed as the discrete counterpart of  $A_\epsilon$ , and by Theorem 2 in [8], its eigenvalues and eigenvectors can be used to approximate the eigenvalues and eigenfunctions of the Laplace-Beltrami operator  $\Delta$  on  $\mathcal{M}$ . Specifically, if  $\lambda$  is an eigenvalue of  $\Delta$ , then,

$$\mu = \exp\left(-\frac{\epsilon^2}{4}\lambda\right) \quad (6)$$

is its corresponding eigenvalue of  $\mathbf{A}$  (see to [34, equation 7]).

Finally, define a symmetric positive-definite matrix by

$$\mathbf{K} = \mathbf{D}^{1/2}\mathbf{A}\mathbf{D}^{-1/2} = \mathbf{D}^{-1/2}\bar{\mathbf{K}}\mathbf{D}^{-1/2} \quad (7)$$

that is similar to  $\mathbf{A}$ . As a result,  $\mathbf{K}$  and  $\mathbf{A}$  share the same eigenvalues and if  $\psi$  is a right eigenvector of  $\mathbf{A}$  then  $\varphi = \mathbf{D}^{1/2}\psi$  is an eigenvector of  $\mathbf{K}$ .

Denote the eigenvalues of  $\mathbf{A}$  by  $1 = \mu_1 \geq \mu_2 \geq \dots \geq \mu_n$ , the left eigenvectors by  $\{\phi_i \in \mathbb{R}^n\}_{i=1}^n$  and the right eigenvectors by  $\{\psi_i \in \mathbb{R}^n\}_{i=1}^n$ . This eigen-decomposition gives rise to a family of nonlinear embeddings, known as diffusion maps:

$$\Psi_t(x_i) = (\mu_2^t \psi_2(x_i), \mu_3^t \psi_3(x_i), \dots, \mu_\ell^t \psi_\ell(x_i))^T \quad (8)$$

for any  $x_i, i = 1, \dots, n$ , where  $t > 0$  and  $\ell \in \{2, \dots, n\}$  are adjustable parameters. Perhaps the most useful property of diffusion maps is that it defines an Euclidean space, where the Euclidean distance between the embedded points is the best approximation in  $\ell < n$  dimensions of the following diffusion distance

$$\|\Psi_t(x_i) - \Psi_t(x_j)\|_2^2 \approx \sum_{l=1}^n (p_t(x_i, x_l) - p_t(x_j, x_l))^2 \frac{1}{\phi_0(l)}$$

where  $p_t(x_i, x_j)$  is the  $(i, j)$ -th entry of  $\mathbf{A}^t$ , and equality is obtained for  $\ell = n$ .

Following [13], we will consider here an un-normalized variant of the diffusion distance, which is given by

$$\|\delta_i^T \mathbf{A}^t - \delta_j^T \mathbf{A}^t\|_2 \quad (9)$$

namely, the Euclidean distance between two ‘masses’ after  $t$  steps of a Markov chain initialized at  $x_i$  and  $x_j$ , where  $\delta_i$  and  $\delta_j$  are  $n$ -dimensional vectors, whose  $i$ th and  $j$ th elements equal 1, respectively, and all other elements equal 0.

In this work, we use both the diffusion operator  $\mathbf{A}$  and its symmetric counterpart  $\mathbf{K}$ . We note that recent work, e.g. [35, 36], introduced extensions to diffusion maps and diffusion distance with doubly-stochastic kernels, which are simultaneously both diffusion operators and symmetric.

## 4 Proposed method

### 4.1 Algorithm

We present an algorithm for building a joint spectral representation of the two sets of simultaneous measurements, which we term *eigenvalue flow diagram*. The proposed algorithm consists of three stages. At the first stage, we build two kernels, which are constructed separately from the two sets of measurements, as described in section 3.2. Concretely, given two sets of (aligned)  $n$  measurements:

$$\left\{ (s_i^{(1)}, s_i^{(2)}) \right\}_{i=1}^n \quad (10)$$

we build two affinity matrices  $\mathbf{W}^{(1)}$  and  $\mathbf{W}^{(2)}$  using Gaussian kernels:

$$W_{i,j}^{(1)} = \exp\left(-\frac{\|s_i^{(1)} - s_j^{(1)}\|_{M_1}^2}{\varepsilon^{(1)}}\right); W_{i,j}^{(2)} = \exp\left(-\frac{\|s_i^{(2)} - s_j^{(2)}\|_{M_2}^2}{\varepsilon^{(2)}}\right) \quad (11)$$

for all  $i, j = 1, \dots, n$ , where  $\varepsilon^{(1)}$  and  $\varepsilon^{(2)}$  are tuneable kernel scales, and  $\|\cdot\|_{M_1}$  and  $\|\cdot\|_{M_2}$  are two norms induced by two metrics corresponding to the two observable spaces  $\mathcal{O}_1$  and  $\mathcal{O}_2$ . Next we apply a two-step normalization to  $\mathbf{W}^{(1)}$  and  $\mathbf{W}^{(2)}$  as described in section 3.2, and obtain the row-stochastic matrices  $\mathbf{A}_1$  and  $\mathbf{A}_2$  by eq. (5) and the SPD kernels  $\mathbf{K}_1$  and  $\mathbf{K}_2$  by eq. (7), respectively. Since  $\mathbf{K}_1$  and  $\mathbf{K}_2$  are SPD, their Riemannian geometry is well-known and the closed-form expressions of the metric eq. (1) and of the unique geodesic path eq. (2) presented in section 3.1 can be applied.

At the second stage, the Riemannian geometry of SPD matrices is utilized. Consider a discrete uniform grid of  $N_t$  points from the interval  $[0, 1]$ ,  $\{t_j\}_{j=1}^{N_t}$ , and compute the collection of matrices along the geodesic path connecting  $\mathbf{K}_1$  and  $\mathbf{K}_2$  on this grid (2), which is given by:

$$\gamma(t_j) = \mathbf{K}_1^{1/2} \left( \mathbf{K}_1^{-1/2} \mathbf{K}_2 \mathbf{K}_1^{-1/2} \right)^{t_j} \mathbf{K}_1^{1/2}.$$

At the third stage, we compute the spectra of the matrices  $\gamma(t_j)$ . Note that  $\gamma(t_j)$  is SPD and therefore has a real and positive spectrum. Denote the largest  $K + 1$  eigenvalues of  $\gamma(t_j)$  by  $\{\mu_{t_j}^k\}_{k=1}^{K+1}$ .

The resulting eigenvalue flow diagram is obtained by the scatter plot of the logarithm of the largest  $K$  eigenvalues,  $\{\log(\mu_{t_j}^k)\}_{k=2}^{K+1}$ , ignoring the trivial  $\mu_{t_j}^1$ , as a function of  $t_j$ .

The entire algorithm is summarized in algorithm 1.

---

**Algorithm 1** Computing the eigenvalues flow diagram.

---

**Input:** Two sets of  $n$  (aligned) measurements:

$$\{(s_i^{(1)}, s_i^{(2)})\}_{i=1}^n$$

**Output:** Eigenvalues flow diagram.

**Parameters:**

- $N_t$  – The number of points on the geodesic path determining the resolution of the flow.
- $K$  – The number of eigenvalues comprising the diagram.

1: For each measurement:  $v = 1, 2$ :

a: Construct an affinity matrix:  $\mathbf{W}^{(v)}$  according eq. (11):

$$W_{i,j}^{(v)} = \exp \left( - \frac{\|s_i^{(v)} - s_j^{(v)}\|_{M_v}^2}{\varepsilon^{(v)}} \right)$$

for all  $i, j = 1, \dots, n$ , where  $\varepsilon^{(v)}$  is the chosen kernel scale, and  $\|\cdot\|_{M_v}$  is the norm induced by the metric in the space of the  $v$ th measurement.

b: Compute the kernel  $\mathbf{K}_v$  by applying a two-step normalization to  $\mathbf{W}^{(v)}$  as described in section 3.2.

2: Consider a discrete uniform grid of  $N_t$  points  $\{t_j\}_{j=1}^{N_t}$  in the interval  $[0, 1]$ . For each  $t_j$ :

a: Calculate the point on the geodesic path at  $t_j$  according to eq. (2):

$$\gamma(t_j) = \mathbf{K}_1^{1/2} \left( \mathbf{K}_1^{-1/2} \mathbf{K}_2 \mathbf{K}_1^{-1/2} \right)^{t_j} \mathbf{K}_1^{1/2}$$

b: Apply eigenvalues decomposition to  $\gamma(t_j)$  and obtain the largest  $K + 1$  eigenvalues of  $\gamma(t_j)$ ,  $\{\mu_{t_j}^k\}_{k=1}^{K+1}$ .

c: Scatter plot the logarithm of the obtained non-trivial eigenvalues  $\{\log(\mu_{t_j}^k)\}_{k=2}^{K+1}$  as a function of  $t_j$ .

---

## 4.2 Illustrative toy example

In order to illustrate algorithm 1, we revisit the toy problem from [13]. We begin with a brief description. The problem consists of three objects: Yoda, Bulldog and Bunny that were placed on three rotating displays. These objects were captured simultaneously by snapshots from two cameras, as depicted in fig. 1. Snapshots from the first camera included Yoda and Bulldog, as presented in fig. 1a, and snapshots from the second camera included Bulldog and Bunny, as presented in fig. 1c. With respect to the considered problem setting, the rotation angles of Bulldog, Yoda and Bunny are realizations from a joint distribution on the product manifold:  $(x, y, z) \in \mathcal{M}_x \times \mathcal{M}_y \times \mathcal{M}_z$ , where  $\mathcal{M}_x$ ,  $\mathcal{M}_y$ , and  $\mathcal{M}_z$  equal the 1-sphere, and the snapshots from camera 1 and camera 2 are the measurements  $\mathcal{S}_1 = g(x, y)$

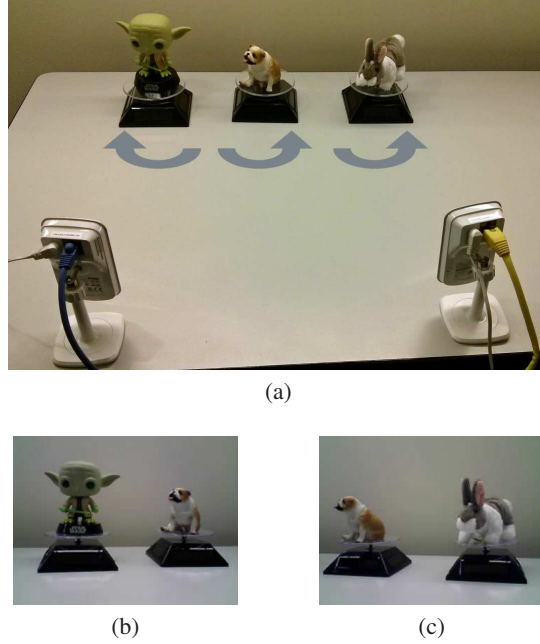


Figure 1: (a) The experiment setup of the toy problem. (b) Sample snapshot taken by camera 1, where only Yoda (the green action figure) and the Bulldog are visible. (c) Sample snapshot taken by camera 2, where only the Bunny and the Bulldog are visible.

and  $\mathcal{S}_2 = h(x, z)$ , respectively. The captured snapshots form a set of  $n$  pairs of measurements:  $\{(s_i^{(1)}, s_i^{(2)})\}_{i=1}^n$ . Each measurement is a column-stack of the captured snapshots, i.e.  $s_i^{(1)}, s_i^{(2)} \in \mathbb{R}^{3 \times N_p}$  where  $N_p$  is the number pixels in each snapshot. Importantly, we note that the proposed approach is data-driven and does not rely on prior knowledge of the specific problem setup; in particular, the knowledge that the hidden variables are rotation angles, that the measurements are images, and that the common variable and the hidden variables appear in separate coordinates (pixels) of the measurements is not taken into account. In [13] the authors demonstrated that point by applying random projections to the captured images, and then processed the projections instead of the original images, which led to comparable results.

We apply algorithm 1 to the two sets of snapshots. For the sake of simplicity of this demonstration, in the computation of the affinity matrices eq. (11), we use the Euclidean distance, and the scales of the kernels are set to be the median of the pairwise distances in each set of measurements. We use a discrete uniform grid of  $N_t = 200$  points  $t_j$  from the interval  $[0, 1]$ , and according to eq. (2), we compute the set of operators  $\{\gamma(t_j)\}_{j=1}^{N_t}$  along the geodesic path connecting  $\mathbf{K}_1$  and  $\mathbf{K}_2$ . Then, for each operator  $\gamma(t_j)$ , we compute the leading  $K = 20$  eigenvalues, denoted by  $\{\mu_{t_j}^k\}_{k=1}^K$ , and their corresponding eigenvectors.

On the left side of fig. 2, we depict the obtained eigenvalue flow diagram. The vertical axis corresponds to the position along the geodesic path  $t_j$ , and the horizontal axis corresponds to values  $\log(\mu_{t_j}^k)$ . Namely, the logarithms of the spectrum of  $\gamma(t_j)$  are plotted horizontally at the vertical coordinate  $t_j$ .

In order to interpret the eigenvalues flow diagram, we pick 3 points along the geodesic path at  $t_j = 0$ ,  $t_j = 0.5$  and  $t_j = 1$ . At each of these points, we take the eigenvectors corresponding to the leading 3 eigenvalues of  $\gamma(t)$  (marked by red circles) and present on the right side of fig. 2 the scatter plots of these eigenvectors as a function the (hidden) angles of the three rotating figures Yoda, Bulldog and Bunny.

We posit that solely by observation, without considering the hidden angles of the rotating figures, the eigenvalues flow diagram in fig. 2 reveals important information about the tasks we aim to accomplish.

First, we can identify the eigenvalues which are associated with the common variables, as the *straight lines* connecting the spectrum of  $\mathbf{K}_1 = \gamma(t_1 = 0)$  and the spectrum of  $\mathbf{K}_2 = \gamma(t_{N_t} = 1)$ . We demonstrate this claim in this example and theoretically support it in the sequel. As can be seen in the depicted insets, the eigenvectors corresponding to eigenvalues that lie on straight lines are highly correlated with the rotation angle of the common Bulldog. Conversely, the eigenvectors corresponding to eigenvalues that do not lie on straight lines correlate with the measurement-specific

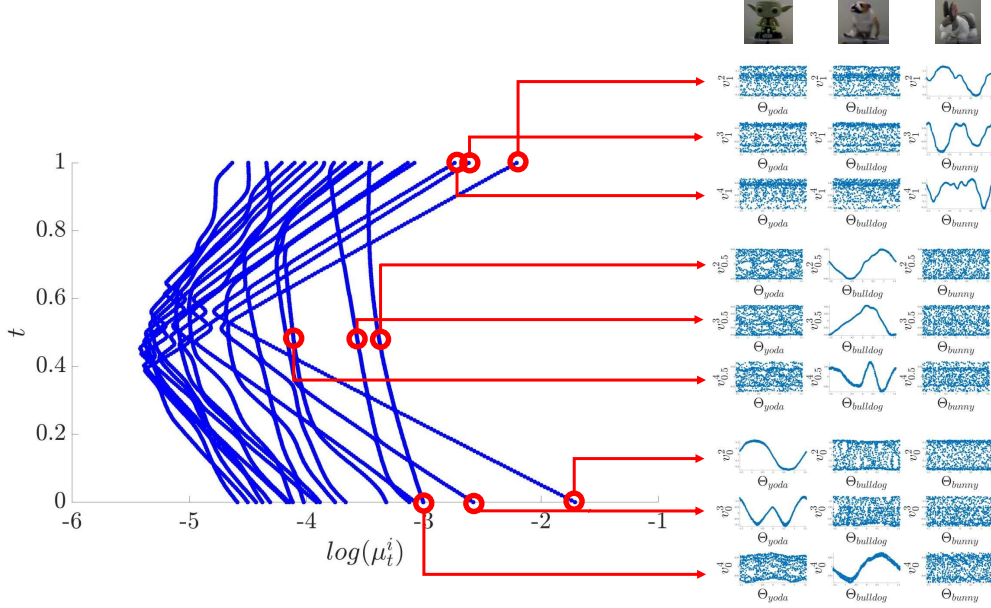


Figure 2: The eigenvalue flow diagram computed for the toy problem. The vertical axis denotes the position on the geodesic path  $t_j \in [0, 1]$ , and the horizontal axis denotes the values of the 20 leading eigenvalues of  $\gamma(t_j)$  in logarithmic scale. The insets that stem from the points within the diagram show the scatter plots of the eigenvectors corresponding to the circled eigenvalues as a function of the puppets’ hidden angles. The puppets’ angles are denoted by  $\Theta_{Yoda}, \Theta_{Bulldog}, \Theta_{Bunny}$ . The eigenvectors of  $\gamma(t_j)$  are denoted by:  $v_{t_j}^k$  where  $k$  is the index of the eigenvector.

variables, namely, the rotation angles of Yoda and Bunny. These eigenvalues can be identified by observation since they do not connect two eigenvalues on the spectra of  $\mathbf{K}_1$  and  $\mathbf{K}_2$ . Further illustration is given in the following video link. The Matlab code for implementing this toy problem is publicly available here (requires code-ocean account) and here (git repository).

Second, the fact that the spectrum of  $\mathbf{K}_1$  (resp.  $\mathbf{K}_2$ ) consists of two types of spectral components, which can be characterized by their distinct flow with respect to  $t$ , enables us to cluster the spectrum of  $\mathbf{K}_1$  (resp.  $\mathbf{K}_2$ ) into two sets. The first set consists of eigenvalues exhibiting a quick decay and therefore corresponding to the measurement-specific variables. The second set consists of eigenvalues exhibiting a log-linear flow and therefore corresponding to the common variables. We remark that there might exist spectral components that correlate both with the common variables and the measurement-specific variables. In this work, we view these components as measurement-specific, namely, non-common.

Third, following the identification of the common and measurement-specific components, we assess the quality of each measurement with respect to the common components. For example, we observe that in camera 1, the measurement-specific component related to Yoda is more dominant than the common component related to Bulldog, which is evident by the spectrum of  $\mathbf{K}_1$ : the eigenvalue corresponding to the rotation angle of Yoda is larger than the eigenvalue corresponding to the rotation angle of Bulldog. Similarly, we observe that in camera 2, the measurement-specific Bunny is more dominant than the common Bulldog. In addition, the ratios between the eigenvalues corresponding to the common object (Bulldog) and the measurement-specific objects in the two cameras imply that the common information in camera 1 is more pronounced than in camera 2. This assessment will be made more concrete in the sequel.

Such an assessment of the common information can be naturally extended from  $\mathbf{K}_1$  and  $\mathbf{K}_2$ , namely, the boundaries of the diagram at  $t_1 = 0$  and  $t_{N_t} = 1$ , to any point  $\gamma(t_j)$ . As a result, the eigenvalue flow diagram can serve as an unsupervised criterion for the identification of an optimal operator  $\gamma(t^*)$ , at which the common spectral components are maximally emphasized. Particularly, in fig. 2, we observe that  $t_j \approx 0.5$  is the optimal point along the geodesic path because the number of components corresponding to the angle of the common Bulldog (with log-linear flows) that appear at the top of the spectrum is maximized at  $t_j \approx 0.5$ . Based on this consideration we propose algorithms for common variable recovery, which extends the framework of alternating diffusion [13]. In the SM in E we further analyze the relationship between alternating diffusion and the current approach.

We conclude this example with a couple important remarks. First, we wish to emphasize that the above results are deduced from the eigenvalues flow diagram, which is computed in a purely unsupervised manner. Second, we note that the empirical results above are obtained by observing the vertical direction of the diagram, namely, the flow of the spectra of the matrices induced by marching along the geodesic path, rather than the horizontal direction, which is the more typical way one would apply spectral analysis.

### 4.3 Spectral flow analysis

Here, we make precise some of the characterizations of the eigenvalues flow diagram made in section 4.2 based on the empirical results. In the following we only state the main results, while the proofs appear in the SM.

**Proposition 1** *If  $v \in \mathbb{R}^n$  is an eigenvector of  $\mathbf{K}_1$  associated with the eigenvalue  $\mu_1$  and an eigenvector of  $\mathbf{K}_2$  associated with the eigenvalue  $\mu_2$ , i.e.  $v$  is a common eigenvector of  $\mathbf{K}_1$  and  $\mathbf{K}_2$ , then  $v$  is also an eigenvector of  $\gamma(t)$  with the corresponding eigenvalue:*

$$\mu_t = \mu_1^{1-t} \mu_2^t \quad (12)$$

Based on proposition 1 we can derive the following corollary.

**Corollary 1** *The flow of the eigenvalues  $\mu_t$  corresponding to common eigenvectors is log-linear with respect to  $t$ , i.e.*

$$\log(\mu_t) = (1 - t) \log(\mu_1) + t \log(\mu_2) \quad (13)$$

This result is demonstrated in the puppets toy example. As can be seen in fig. 2, the eigenvalues which are related to the common spectral components (corresponding to the common Bulldog’s angle) exhibit log-linear behavior.

**Proposition 2** *If  $v \in \mathbb{R}^n$  is an eigenvector of  $\mathbf{K}_1$  but not an eigenvector of  $\mathbf{K}_2$ , then  $v$  is not an eigenvector of  $\gamma(t)$ .*

proposition 2 gives only a partial explanation to the correspondence between the eigenvalues flow diagram and the non-common variables. In order to gain further insight, in B in the SM, we analyze the eigenvalue flow diagram under a different, yet related *discrete* graph model, making use of well-known results in spectral graph theory.

## 4.4 Implementation Remarks

### 4.4.1 Approximate geodesic path

Often, in practice, the kernels  $\mathbf{K}_1$  and  $\mathbf{K}_2$  might have small eigenvalues that due to numerical issues might be quantized to zeros. In these cases the matrices are no longer strictly positive, making the metric, the geodesic path, and the distance, presented in section 3.1, no longer valid. To circumvent the problem, we implement an approximation of the geodesic path for fixed-rank positive semi-definite matrices, proposed in [37]. There, the authors presented a metric, which is derived from a well-chosen Riemannian quotient geometry that generalizes the reductive geometry of the manifold of SPD matrices. Based on the proposed metric, an approximation of the geodesic path is derived. For more details and the close-form expression of the approximate geodesic path, see D in the SM.

### 4.4.2 Post-processing the diagram

We propose three post-processing procedures that can be applied to the eigenvalues flow diagram in order to make the characterization presented in section 4.2 systematic.

The first procedure aims to extract sequences of components (trajectories) along the geodesic flow. From the eigenvalues flow diagram presented in fig. 2, we can identify the sequence of the different components along the geodesic path (along the parameter  $t$ ) simply by observation. Extracting these sequences provides important information, enabling us to identify common and unique spectral components between the two measurements. In particular, equipped with the results presented in section 4.3, eigenvalues lying on log-linear trajectories can be associated with common spectral components, and the remaining eigenvalues can be associated with measurement-specific (or mixed) spectral components. In the SM in section F.1, we present an algorithm that resolves the trajectories.

The second procedure measures the “commonality” of a given spectral component, which is not an accessible information in unsupervised settings. We propose two algorithms for this purpose. The first algorithm relies on the log-linear trajectory of eigenvalues associated with the common components. This algorithm requires to resolve the trajectories by applying the algorithm mentioned above as a prerequisite. The second algorithm utilizes an empirical observation that is demonstrated in section 5.1. The two algorithms for commonality assessment are described in detail in the SM in section F.2.1 and in section F.2.2.



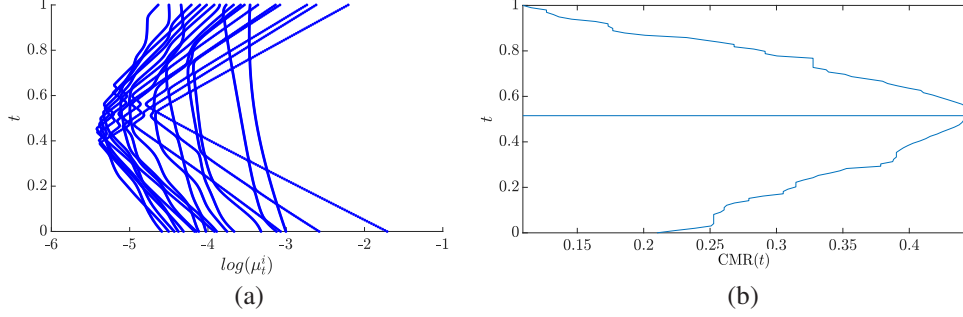


Figure 3: (a) an eigenvalues flow diagram, and (b) the corresponding CMR(t) estimation.

By applying some threshold, the measure of commonality of each spectral component enables us to divide the spectral components into two disjoint sets:  $\mathcal{S}_c$  and  $\mathcal{S}_{nc}$ , where  $\mathcal{S}_c$  denotes the set of indices of common spectral components and  $\mathcal{S}_{nc}$  consists of the remaining indices. Based on these two sets, we define the “Common to Measurement-specific Ratio” (CMR) as:

$$\text{CMR}(t) = \frac{\sum_{i \in \mathcal{S}_c} \mu_t^i}{\sum_{i \in \mathcal{S}_{nc}} \mu_t^i}. \quad (14)$$

fig. 3 illustrates the computed CMR corresponding to the eigenvalue flow diagram of the puppets toy example in section 4.2.

As evident from this figure, there exists  $t^*$  that maximizes the CMR in eq. (14), i.e.:  $t^* = \underset{t}{\operatorname{argmax}} \text{CMR}(t)$ . Then, by computing  $\gamma(t^*)$  and applying spectral analysis to  $\gamma(t^*)$  as in diffusion maps described in section 3.2, we obtain a representation where the spectral components of the underlying common manifold  $\mathcal{M}_x$  are more pronounced. A generalization of this simple procedure appears in the SM in section F.3. The embedding derived from the leading spectral components of  $\gamma(t^*)$  could be viewed as an alternative to the embedding obtained by alternating diffusion [13]. However, a comprehensive comparison between the two methods extends the scope of this paper and will appear in a future work.

## 5 Simulation results

### 5.1 2D flat manifolds

Consider three manifolds  $\mathcal{M}_x = \mathcal{M}_y = \mathcal{M}_z = [-1/2, 1/2]$ , and consider tuples  $\{(x_i, y_i, z_i)\}_{i=1}^n$ , which are  $n$  realizations sampled from some joint distribution on the product manifold  $\mathcal{M}_x \times \mathcal{M}_y \times \mathcal{M}_z$ . These realizations are measured in the following manner:

$$\begin{aligned} s_i^{(1)} &= (\ell_x^{(1)} x_i, \ell_y^{(1)} y_i) \in \mathbb{R}^2 \\ s_i^{(2)} &= (\ell_x^{(2)} x_i, \ell_z^{(2)} z_i) \in \mathbb{R}^2 \end{aligned} \quad (15)$$

where  $\ell_x^{(1)}, \ell_x^{(2)}, \ell_y^{(1)}, \ell_z^{(2)}$  are positive scaling parameters. The scaling parameters enable us to control the relative dominance of each of the hidden variables on the measurements.

Although rather simple, this example is tractable since the eigenvalues of the Laplace-Beltrami operators of the considered manifolds have closed-form expressions. Specifically, the eigenvalues of the Laplace-Beltrami operator with Neumann boundary conditions on the manifolds  $\mathcal{O}_1 = [-\ell_x^{(1)}/2, \ell_x^{(1)}/2] \times [-\ell_y^{(1)}/2, \ell_y^{(1)}/2]$  and  $\mathcal{O}_2 = [-\ell_x^{(2)}/2, \ell_x^{(2)}/2] \times [-\ell_z^{(2)}/2, \ell_z^{(2)}/2]$  are given by (see [34, equation 2]):

$$\begin{aligned} \lambda_1^{(k_x, k_y)} &= \left( \frac{k_x \pi}{\ell_x^{(1)}} \right)^2 + \left( \frac{k_y \pi}{\ell_y^{(1)}} \right)^2 \\ \lambda_2^{(k_x, k_z)} &= \left( \frac{k_x \pi}{\ell_x^{(2)}} \right)^2 + \left( \frac{k_z \pi}{\ell_z^{(2)}} \right)^2 \end{aligned} \quad (16)$$



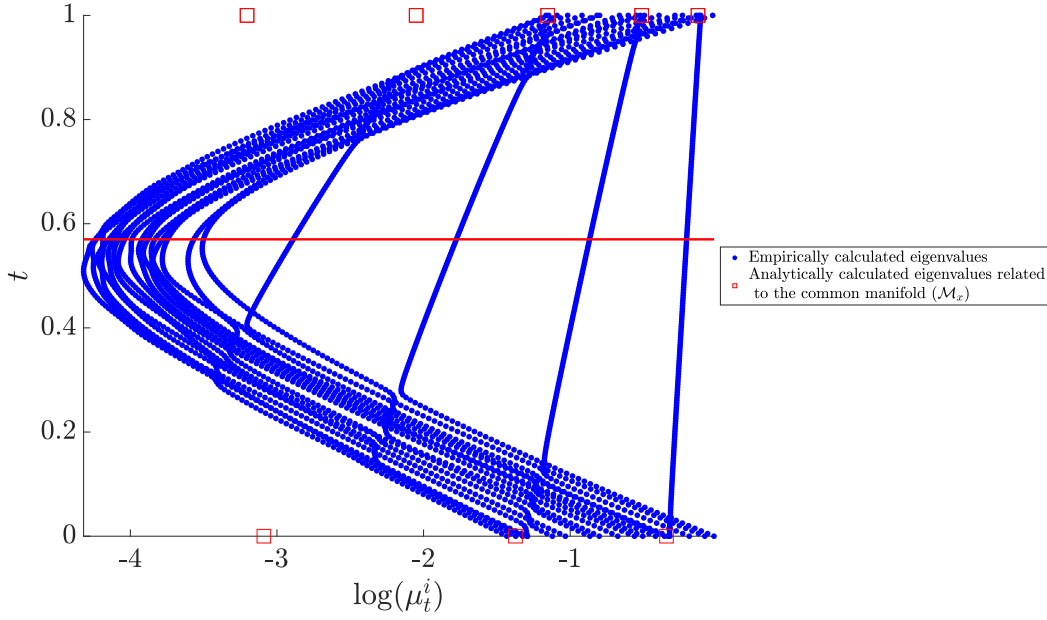


Figure 4: The eigenvalues flow diagram obtained by applying algorithm 1 to  $(s_i^{(1)}, s_i^{(2)})$  in the 2D flat manifolds example. The point  $t$  at which the CMR is maximal is marked by a horizontal line. The analytically calculated eigenvalues at the boundaries of the diagram (at  $t = 0$  and  $t = 1$ ) are computed based on eq. (16).

respectively, where  $k_x, k_y, k_z = 0, 1, 2, \dots$ . Evidently, the common spectral components, i.e. the components which are related only to  $\mathcal{M}_x$ , are given by  $\{\lambda_1^{(k_x, k_y=0)}\}_{k_x=0}^\infty$  and  $\{\lambda_2^{(k_x, k_z=0)}\}_{k_x=0}^\infty$ .

In this simulation we set the following values to the scaling parameters:

$$\begin{aligned}\ell_x^{(1)} &= 2, \ell_x^{(2)} = 2 \\ \ell_y^{(1)} &= 8, \ell_z^{(2)} = 4\end{aligned}$$

making the common variable more dominant in  $\{s_i^{(2)}\}_{i=1}^n$  than in  $\{s_i^{(1)}\}_{i=1}^n$  with respect to the measurement-specific variables. We generate  $n = 1,000$  points  $(x_i, y_i, z_i)$  where  $x_i \in \mathcal{M}_x$ ,  $y_i \in \mathcal{M}_y$ , and  $z_i \in \mathcal{M}_z$  are sampled uniformly and independently from each manifold. Each hidden point  $(x_i, y_i, z_i)$  gives rise to a pair of measurements:  $(s_i^{(1)}, s_i^{(2)})$  according to eq. (15). In the SM in C, we present additional results for different choices of the scaling parameters and non-uniform distributions.

We apply algorithm 1 to the two sets of 1,000 measurements,  $(s_i^{(1)}, s_i^{(2)})$ , and obtain the eigenvalues flow diagram. We set the number of points on the geodesic path to  $N_t = 200$  and the number of eigenvalues to  $K = 20$ . Based on the diagram, according to the procedure described in the SM in algorithm 4, we estimate the CMR at each point along the geodesic path. The resulting eigenvalues flow diagram is depicted in fig. 4, where the point  $t$  along the geodesic path at which the CMR estimation is maximal is marked by a horizontal line. As can be seen, the highest CMR is not obtained at the middle of the geodesic path, but closer to the point  $t = 1$ , which represents the kernel of the set of measurements where the common component is more dominant.

By eq. (6) and eq. (16), we analytically compute the eigenvalues of  $\mathbf{K}_1 = \gamma(0)$  and  $\mathbf{K}_2 = \gamma(1)$  and overlay only the eigenvalues corresponding to common eigenvectors on the diagram in fig. 4 at the boundaries  $t = 0$  and  $t = 1$  (marked by squares). Indeed, we observe that the empirical eigenvalues lying on log-linear trajectories coincide with the common components (squares).

To demonstrate the extraction of the common components, we show the diffusion propagation resulting from  $\gamma(t)$  at different  $t$  values, as described in section 3.2 leading to the variant of the diffusion distance eq. (8).

Let  $i_0$  be the index of the closest measurement to  $(x, y) = (0, 0)$  and let  $\delta_{i_0} \in \mathbb{R}^{1,000}$  be a vector of all-zeros except the  $i_0$ th entry which equals 1. This vector represents a mass on the points initially concentrated entirely at  $i_0$ . In fig. 5, we show the diffusion patterns at four points along the geodesic path, namely, we compute  $[\gamma(t)]^s \delta_{i_0}$  at  $t = 0, 0.3, t^*, 1$ ,

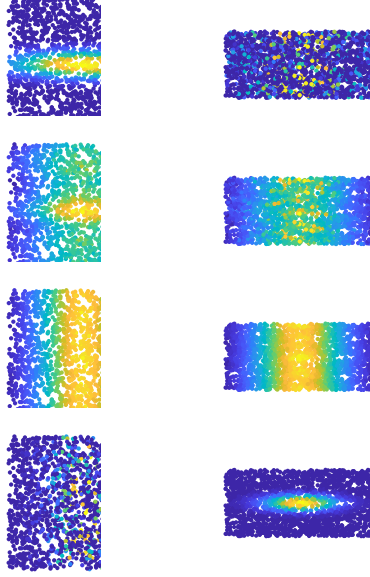


Figure 5: Diffusion patterns for several points along the geodesic path. At the left column, we plot the measurements from  $\mathcal{O}_1$ , and at the right column we plot the measurements from  $\mathcal{O}_2$ . In each column, the horizontal axis is associated with the common variable and the vertical axis with the measure-specific variable. The measurements are colored as follows. The color at the top row corresponds to the diffusion pattern of  $\gamma(0) = \mathbf{K}_1$ , at the second and the third rows to  $\gamma(0.3)$  and  $\gamma(t^*)$ , and at the bottom row to the diffusion pattern of  $\gamma(1) = \mathbf{K}_2$ .

where  $t^* \simeq 0.6$  is the point at which the CMR is maximal, and the number of steps is set to  $s = 2$ . The resulting vectors are then used to color the points.

We observe that at  $t = 0$  and  $t = 1$ , the diffusion patterns are isotropic. When marching on the geodesic path from  $t = 0$  to  $t = 1$ , we observe that the diffusion pattern changes. Specifically, at  $t^*$ , the diffusion pattern saturates along the vertical axis, which represents  $\mathcal{M}_y$  and  $\mathcal{M}_z$ . Moreover, comparing the diffusion pattern at  $t = t^*$  with the diffusion patterns at  $t = 0, 0.3, 1$  demonstrates the importance of finding the optimal point along the geodesic path. In problems in which the CMRs at the two measurements is significantly different, a proper choice of the point along the geodesic path can be crucial. We present such an example in the SM in C. In addition, we repeat this empirical test for 2D tori embedded in 3D, the results are reported in the SM in C.

Next, we compare the eigenvalues flow diagram obtained by algorithm 1 along the geodesic path  $\gamma(t)$  to the eigenvalues flow diagram obtained along the following linear interpolation:

$$\mathbf{L}(t) = (1 - t)\mathbf{K}_1 + t\mathbf{K}_2$$

An immediate difference between the two interpolation schemes is conveyed by observing the resulting eigenvalues corresponding to the common eigenvectors. From the explicit expressions of the  $k_x$ th common eigenvalues of  $\mathbf{K}_1$  and  $\mathbf{K}_2$  given by eq. (6) and eq. (12) and denoted by  $\mu_1^{(k_x,0)}$  and  $\mu_2^{(k_x,0)}$ , the explicit expression of the corresponding eigenvalue of  $\gamma(t)$  can be derived:

$$\begin{aligned} \mu_{\gamma(t)}^{(k_x,0)} &= \left(\mu_1^{(k_x,0)}\right)^t \left(\mu_2^{(k_x,0)}\right)^{1-t} \\ &= \exp\left(-\frac{1}{4}\left((1-t)\left(\epsilon^{(1)}\right)^2 \lambda_1^{(k_x,0)} + t\left(\epsilon^{(2)}\right)^2 \lambda_2^{(k_x,0)}\right)\right) \\ &= \exp\left(-\left(\frac{\pi}{4\ell(\gamma(t))}\right)^2 k_x^2\right) \end{aligned} \quad (17)$$

where  $\ell(\gamma(t))$  is given by

$$\ell(\gamma(t)) = \sqrt{\frac{\ell^{(1)}\ell^{(2)}}{(1-t)\ell^{(1)} + t\ell^{(2)}}} \quad (18)$$

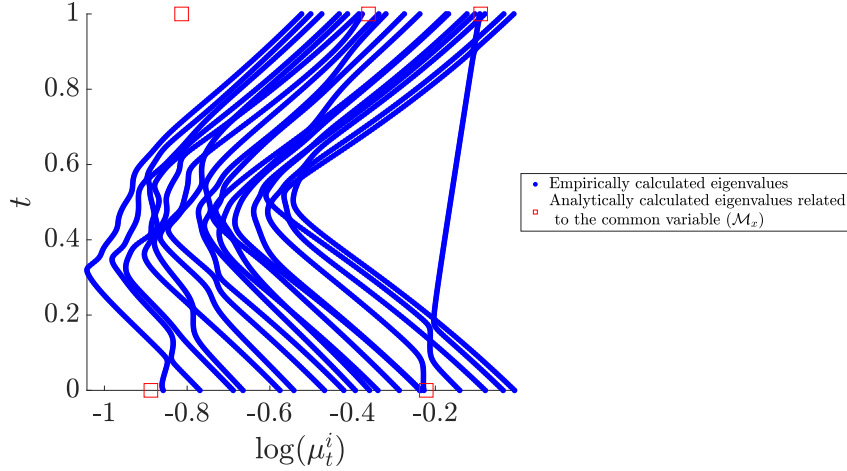


Figure 6: As fig. 4, only the eigenvalues flow diagram is obtained by the linear interpolation.

where  $\ell^{(1)} = \frac{\ell^{(1)}}{\epsilon^{(1)}}$ , and  $\ell^{(2)} = \frac{\ell^{(2)}}{\epsilon^{(2)}}$ . The obtained expression of in eq. (17) corresponds to the  $k_x$ -th eigenvalue of a kernel associated with the Laplacian of the 1D manifold  $[0, \ell^{(\gamma(t))}]$ . In other words, the eigenvalues of  $\gamma(t)$  residing on log-linear trajectories admit Weyl's law, and therefore, reconstructing kernels only from these spectral components could be viewed as kernels corresponding to some effective manifold.

In contrast, if we use the linear interpolation  $\mathbf{L}(t)$ , the  $k_x$ -th eigenvalue of  $\mathbf{L}(t)$  is given by

$$\begin{aligned} \mu_{\mathbf{L}(t)}^{(k_x,0)} &= (1-t)\mu_1^{(k_x,0)} + t\mu_2^{(k_x,0)} \\ &= (1-t) \exp\left(-\frac{(\epsilon^{(1)})^2}{4}\lambda_1^{(k_x,0)}\right) + t \exp\left(-\frac{(\epsilon^{(2)})^2}{4}\lambda_2^{(k_x,0)}\right) \\ &= (1-t) \exp\left(-\left(\frac{\epsilon^{(1)}\pi}{4\ell_x^{(1)}}\right)^2 k_x^2\right) + t \exp\left(-\left(\frac{\epsilon^{(2)}\pi}{4\ell_x^{(2)}}\right)^2 k_x^2\right) \end{aligned} \quad (19)$$

which generally cannot be expressed in an exponential form:  $\exp(-ck_x^2)$ , where  $k_x$  is the eigenvalue index and  $c$  is a certain constant corresponding to the scale of the manifold.

We apply a variant of algorithm 1, where we replace the geodesic path  $\gamma(t)$  with the linear interpolation  $\mathbf{L}(t)$ , to the measurements  $(s_i^{(1)}, s_i^{(2)})$ . The resulting eigenvalues flow diagram is depicted in fig. 6.

By comparing the two eigenvalues flow diagrams in fig. 4 and fig. 6, we observe that at the boundaries ( $\gamma(0) = \mathbf{L}(0) = \mathbf{K}_1$  and  $\gamma(1) = \mathbf{L}(1) = \mathbf{K}_2$ ) the two diagrams coincide. Conversely, as we get farther from the boundaries for  $0 < t < 1$ , the two diagrams look different, especially in terms of the suppression of the measurement-specific components, which results in the discovery of fewer common eigenvectors. For instance, at  $t = 0.5$ , the logarithm of the largest eigenvalues corresponding to the measurement-specific components in the geodesic flow is approximately  $-3.5$  whereas in the linear flow it is approximately  $-0.5$ .

In section 4.3 we showed that the common eigenvectors are preserved when marching along the geodesic path (proposition 1) and that the non-common eigenvectors are not part of the spectra of the geodesic path (proposition 2). Our experimental study reveals a stronger result. Not only that these non-common eigenvectors are not part of the spectra of the geodesic path, their energy is quickly spread over the entire spectrum of matrices along the geodesic path as the interpolation gets further away from the boundaries.

We exemplify this empirical result on the 2D flat manifolds considered here. We pick two eigenvectors of  $\mathbf{K}_1$ , denoted by  $v_c$  and  $v_{nc}$ . Suppose that  $v_c$  is a common eigenvector, and suppose that  $v_{nc}$  is a measurement-specific eigenvector, i.e., it is not an eigenvector of  $\mathbf{K}_2$ , and as a consequence (by proposition 2) it is not an eigenvector of any other matrix along the geodesic  $\gamma(t)$ . We use a discrete uniform grid of  $t \in [0, 1]$ . For each point on the grid  $t$ , we calculate the matrix  $\gamma(t)$  and its set of eigenvectors:  $\{v_t^k\}_{k=1}^n$ . We then calculate the inner products between the vectors  $\{v_t^k\}_{k=1}^n$  and  $v_c$  or  $v_{nc}$ . The obtained inner products  $\{\langle v_c, v_t^k \rangle\}_{k=1}^n$  and  $\{\langle v_{nc}, v_t^k \rangle\}_{k=1}^n$  are the spectral representation of  $v_c$  and  $v_{nc}$ , respectively, since they are the expansion coefficients when using the eigenvectors of  $\gamma(t)$  as a basis.

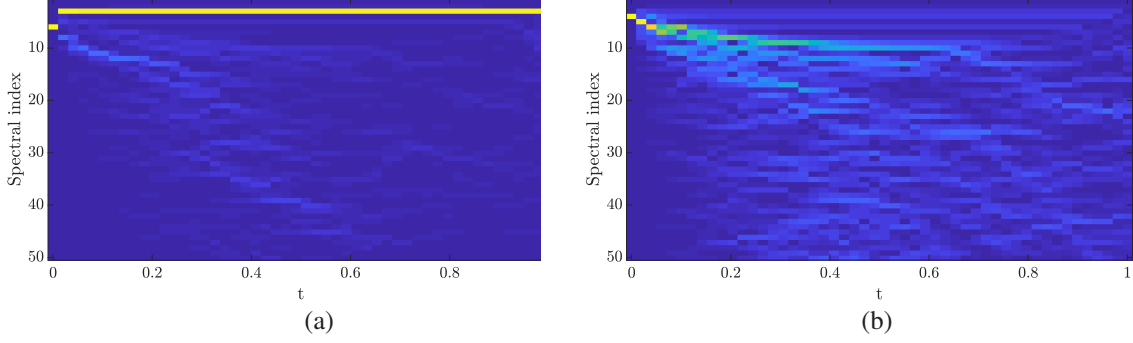


Figure 7: The spectral representation of (a)  $v_c$  and (b)  $v_{nc}$  at each point  $t$  along the geodesic path.

In fig. 7 we show the absolute values of  $\{\langle v_c, v_t^k \rangle\}_{k=1}^n$  and  $\{\langle v_{nc}, v_t^k \rangle\}_{k=1}^n$  in columns, where the horizontal axis denotes  $t$  and the vertical axis denotes the spectral component index  $k$ . The spectral components are sorted in an descending order of their respective eigenvalues (high values on top). We observe that the spectral representation of the common eigenvector  $v_c$  at every point  $t$  along the geodesic path is concentrated only at a single spectral component. Furthermore, this spectral component for  $t \in (\delta, 1 - \delta)$  appears higher in the spectrum, implying that the common components are more pronounced in  $\gamma(t)$  compared to  $\mathbf{K}_1$ . This is an empirical verification of proposition 1. In addition, we observe that the measurement-specific colorcyan eigenvector  $v_{nc}$  admits a completely different behavior. Not only that  $v_{nc}$  is not an eigenvector of the geodesic path, its spectral representation  $\{\langle v_{nc}, v_t^k \rangle\}_{k=1}^n$  quickly spreads over the entire spectrum as  $t$  increases.

## 6 Results on real data

In this section we consider two real-world data sets and demonstrate the applicability of the proposed framework. The data sets we use for demonstration are labeled. Nevertheless, the labels are used only for validating the results which were derived completely in an unsupervised manner.

### 6.1 Artificial olfaction for gas identification

Artificial olfaction, also known as electronic nose (E-Nose), is a relatively new technology. An artificial olfaction system aims to detect, classify or quantify a chemical analyte or odor in the surrounding of the system. Such systems can be used for multiple purposes, e.g., quality control of food [38], detection and diagnosis for medical applications [39], and environmental monitoring and homeland security [40]. In the following, we apply the proposed analysis to an artificial olfaction data set. We remark that our goal here is only to demonstrate the analysis on real data, and we postpone further developments, including comparisons to other methods, to future work.

The dataset we use was taken from [41] and is publicly available. The dataset comprises recordings from six distinct pure gaseous substances: Ammonia, Acetaldehyde, Acetone, Ethylene, Ethanol, and Toluene, each dosed at a wide variety of concentrations. The recordings are acquired by an array of 16 metal-oxide gas sensors. Each record in the dataset is a tuple of measurements and labels corresponding to a single acquisition. In each acquisition, only one gas is being injected at a certain level of concentration. The response of the sensors is a read-out of the resistance across the active layers of each sensor. The resistance from each sensor was aggregated in 8 different manners. Therefore, each measurement is a 128 dimensional vector: a sample from 16 sensors, each aggregated 8 times, and each label vector is a 6 dimensional vector consisting of a single non-zero entry, where the index of this entry indicates which gas was injected during the acquisition and the value of this entry indicates the level of concentration of the injected gas during the acquisition.

In fig. 8 we show the scatter plot of the data acquired by the 5th sensor and the Acetaldehyde concentration for each record of Acetaldehyde injection in the dataset. We observe that the 8 aggregated responses of this sensor, when exposed to the same analyte under identical conditions, are inconsistent. Ideally, these sensor arrays should show the same response when exposed to the same analyte or the same chemical mixture and should return to their baseline level immediately after the analyte or a chemical mixture is removed from the sensors area. However, in practice, especially when these sensors are operated over a long period of time, the sensors responses drift. This phenomenon makes the extraction of the gas from a single channel challenging [42]. Specifically, in an unsupervised setting, without access to the true gas concentrations, it is unknown a-priori which features are correlated with each of the substances.

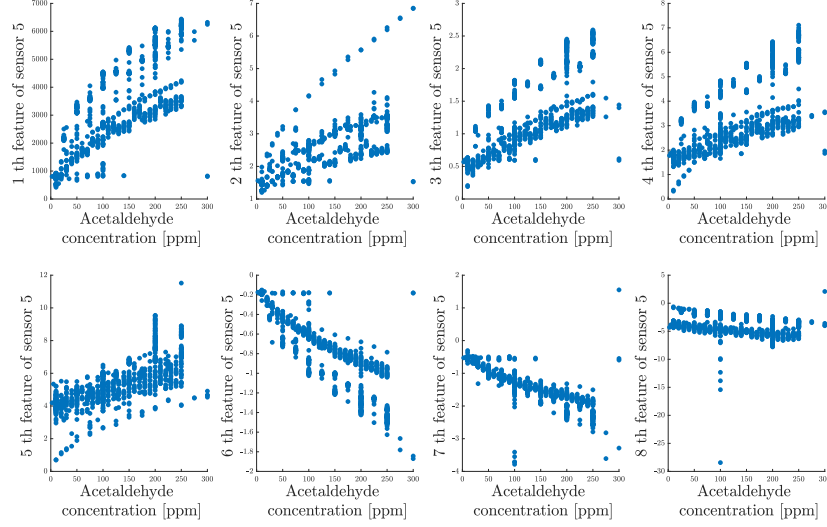


Figure 8: Raw data acquired from the 5th sensor in the sensors array as a function of the Acetaldehyde concentrations. Each one of the 8 features (8 different aggregations) is depicted in a different subplot.

For demonstration purposes, we focus on the 5th and 11th sensors. This particular pair was chosen since our unsupervised empirical analysis revealed that the common components of this pair are not the principal components, and therefore, their identification and extraction is not trivial. Let  $\{s_i^{(5)} \in \mathbb{R}^8\}_{i=1}^n$  and  $\{s_i^{(11)} \in \mathbb{R}^8\}_{i=1}^n$  denote  $n = 1,000$  samples from the sensors, where each sample is embedded in 8 dimensional space.

We apply algorithm 1 to the two sets, and in fig. 9 we present the obtained eigenvalues flow diagram with  $K = 10$  leading eigenvalues and  $N_t = 200$  points on the geodesic path. In addition, as in the puppets toy example, we pick 3 points along the geodesic path at  $t = 0$ ,  $t = 0.5$ , and  $t = 1$ . At each of these points, we take the leading 3 eigenvectors of  $\gamma(t)$ , and scatter plot them against the Acetaldehyde concentration. These scatter plots are presented as insets in fig. 9.

We observe that a common component is revealed at the middle of the geodesic path, as the eigenvector corresponding the largest eigenvalue. Moreover, using the labels, we observe in the insets that the common components are useful because they are strongly associated with the Acetaldehyde concentration. Conversely, the measurement-specific components, i.e. the components which are quickly suppressed, do not exhibit any correlation with the Acetaldehyde concentration and seem to be related to outliers and interferences. In this example, the diagram also reveals that the common components can be directly identified from the spectrum of  $\mathbf{K}_1 = \gamma(0)$  as the second and third eigenvectors,

We emphasize that the entire analysis is unsupervised and that the labels in the insets are used only for the purpose of validation. Further results on this dataset appear in the SM in C.

## 6.2 Condition monitoring

Condition monitoring is a process that aims to assess the condition of a certain machinery for the purpose of early identification of faults and malfunctions [43]. Typically in condition monitoring, incorporating data from two or more sensors is highly beneficial, because it can significantly enhance the robustness to failures of the condition monitoring system itself; since simultaneous failures in more than one sensor are rare, utilizing two or more sensors can help to distinguish between the state of the monitored system and the state of the monitoring sensors.

Here, we examine a dataset consisting of measurements of a hydraulic test rig [44]. The system periodically repeats constant load cycles, each of duration of 60 seconds, and monitors values using 17 sensors, such as pressure, volume flow and temperature sensors. During the monitored period, the condition of the hydraulic test rig quantitatively varies. Each record in the dataset consists of signal acquisitions and their labels. The signals are 17 time-series representing the sensor measurements during one load cycle. Each time series is of different length, which is determined by the sampling rate of the respective sensor. Following the notation of this work, let  $s_i^{(l)} \in \mathbb{R}^{60f_s^{(l)}}$  denote a vector representing the time-series measured during the  $i$ th load cycle by sensor  $l$ , where  $f_s^{(l)}$  is the sampling rate. The labels are 4-dimensional vectors representing the condition of four components of the hydraulic system: cooling efficiency,

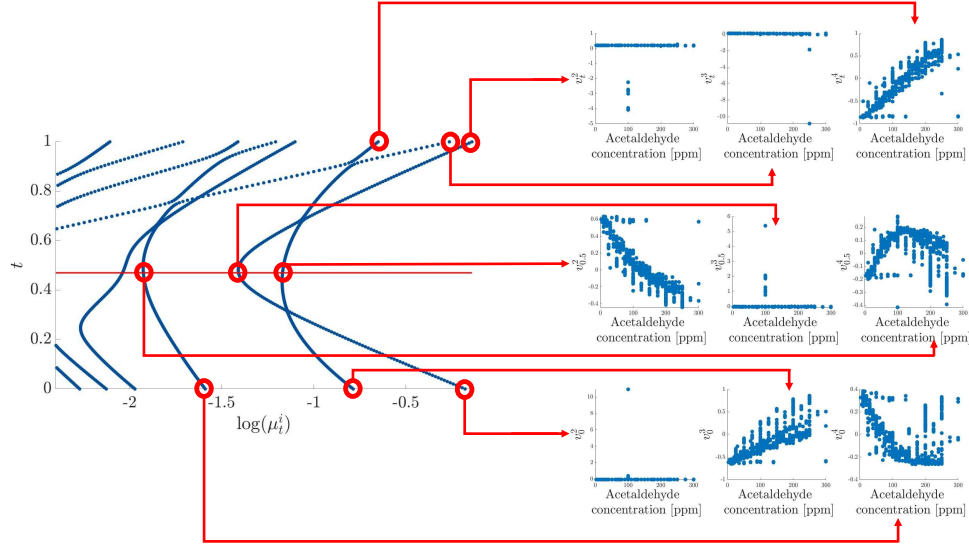


Figure 9: Eigenvalues flow diagram obtained by applying algorithm 1 to the measurements acquired by the 5th and 11th sensors from the E-Nose dataset. The insets display 9 scatter plots of selected eigenvectors as functions of the Acetaldehyde concentration. The point at which the CMR is maximal is marked by a horizontal line.

valve lag, internal pump leakage and the hydraulic accumulator pressure, at each load cycle. For further details on the dataset, see [44, Section 2].

In the first test, we examine the cooling efficiency based on  $n = 1,000$  measurements from the pressure meter, denoted by PS5, and the motor power meter, denoted by EPS1. We choose this pair for demonstration because these particular sensors have hidden common components contaminated by strong measurement-specific sources of variability. In fig. 10, we present the obtained eigenvalues flow diagram by algorithm 1 applied to  $\{s_i^{(PS5)}\}_{i=1}^n$  and  $\{s_i^{(EPS1)}\}_{i=1}^n$ . The figure also contains insets with the correspondence of the eigenvectors to the labels. In contrast to fig. 9, because the ground-truth here is categorical (can be one of 3 levels: full efficiency, reduced efficiency and close to total failure), the insets in fig. 10 depict scatter plots of the 3 leading eigenvectors, colored by the cooling efficiency level.

From the eigenvalues flow diagram, we observe the clear existence of a common component. Moreover, by utilizing the given labels, we observe in the insets that this common component is strongly associated with the cooling efficiency. In addition, the layout of the monitoring system provided with the dataset implies that the pressure meter PS5 is located in close proximity to the cooler, whereas the motor power meter EPS1 is located remotely. This observation coincides with the obtained eigenvalues flow diagram, where the common component indeed seems to be more dominant in the pressure meter (at  $t = 1$ ) compared to the motor power meter (at  $t = 0$ ).

Next we compare the proposed framework to a naïve approach based on the linear interpolation presented in (5.1). We repeat the same procedure and compute the eigenvalues flow diagram corresponding to this linear interpolation. The obtained eigenvalues *linear* flow diagram is depicted in fig. 11. We observe a similar behavior as in fig. 6 presented in section 5.1. The attenuation of the measurement-specific sources of variability is not as significant as in the eigenvalues flow diagram based on the geodesic path, and as a consequence, the identification and extraction of the common components is not as distinct.

In the second test, we predict the lag of the valve lag from the pressure meter, denoted by PS1, and the volume flow meter, denoted by FS1. The eigenvalues flow diagram obtained by applying algorithm 1 to  $\{s_i^{(PS1)}\}_{i=1}^n$  and  $\{s_i^{(FS1)}\}_{i=1}^n$  is presented in fig. 12. As in fig. 10, the ground-truth is categorical (the valve's lag is quantized into 4 possible states: optimal switching behavior, small lag, severe lag and close to total failure), and therefore, the insets depict the scatter plots of the 3 leading eigenvectors colored by the valve's condition.

We observe that the common component is well pronounced by the pressure meter, which is located in close proximity to the valve, but only weakly pronounced by the flow meter which is located remotely. In addition, we observe that the common components are strongly associated with the valve's lag, in contrast to the components that quickly decay.



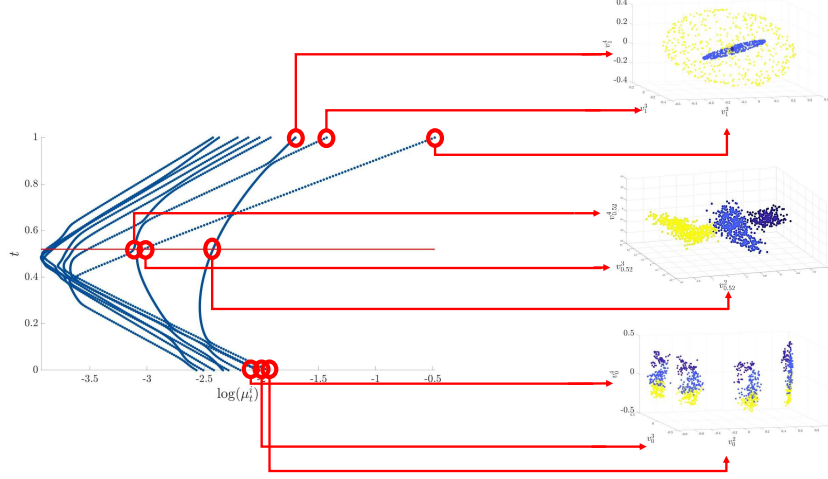


Figure 10: Eigenvalues flow diagram obtained by applying algorithm 1 to measurements from the pressure meter and the motor power meter from the condition monitoring dataset. The 3 insets display the scatter plots the 3 leading eigenvectors colored by the cooling efficiency (yellow – full efficiency, light blue – reduced efficiency, dark blue – close to total failure). The point at which the CMR is maximal is marked by a horizontal line.

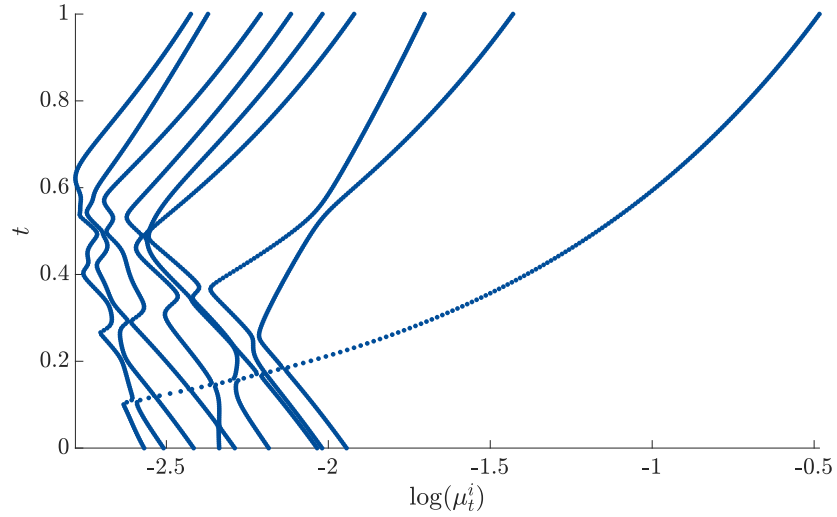


Figure 11: Eigenvalues *linear* flow diagram obtained based on measurements from the pressure meter and the motor power meter from the condition monitoring dataset.

As mentioned above, the monitoring sensors are prone to failures just as the system itself. Since failures are rare to happen simultaneously in two sensors, common components between two (or more) sensors are invariant to such failures and facilitate the ability to distinguish between sensor faults and system faults. The reader may refer to [45] for further description of this problem.

To simulate sensor fault, we repeat the last test, where we artificially add noise to the pressure meter PS1. Specifically, we add a slow sine wave, as in [44]. The obtained eigenvalues flow diagram is presented in fig. 13(a). For comparison we present the eigenvalues flow diagram obtained by the linear interpolation in fig. 13(b). Now, we observe that the common component is no longer the most dominant component in the (noisy) pressure meter, however, marching along the geodesic path towards the other sensor suppresses the influence of the additive sine wave. In addition, we observe that the attenuation of the measurement-specific sources of variability is more significant when using the geodesic path compared to the linear interpolation.

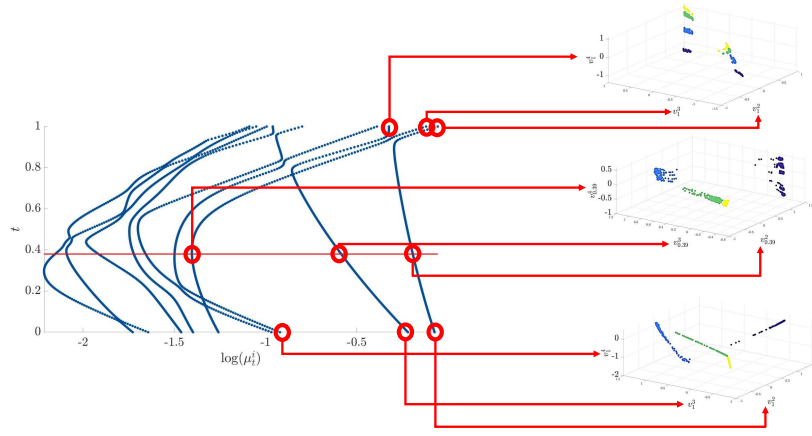


Figure 12: Eigenvalues flow diagram obtained by applying algorithm 1 to measurements from the pressure meter and the volume flow meter from the condition monitoring dataset. The 3 insets display the scatter plots the 3 leading eigenvectors colored by the valve's lag (yellow – optimal switching behavior, green – small lag, light blue – severe lag, dark blue – close to total failure). The point at which the CMR is maximal is marked by a horizontal line.

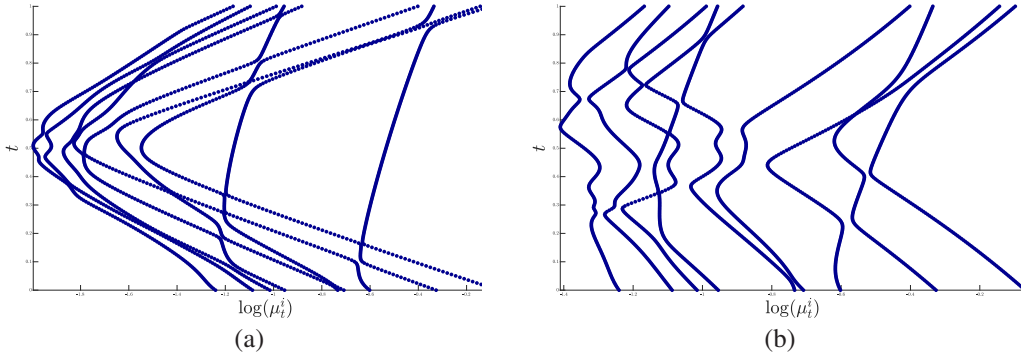


Figure 13: Eigenvalues flow diagrams obtained based on artificially corrupted measurements from the pressure meter and the measurements from the volume flow meter from the condition monitoring dataset. (a) The eigenvalue flow diagram obtained by algorithm 1. (b) The eigenvalues *linear* flow diagram.

## 7 Conclusions

In this paper we presented an unsupervised data-driven framework for multimodal data analysis. The proposed framework combines spectral methods with the well-known geometry of SPD matrices. We presented theoretical analysis and devised a set of algorithms, which were demonstrated on synthetic and real data. Our results show, both theoretically and empirically, that the proposed framework successfully reveals various sources of variability driving the measurements and extracts their mutual relationships.

Our approach is based on a multiscale view of the data, from the micro scale of the raw data, via the mezzo scale of SPD kernels, to the macro scale of the proposed spectral flow. We posit that the micro scale of the raw data, although being the most descriptive form of the measured phenomenon, is very complex, high-dimensional, could be deformed in various ways and might contain multiple sources of variability which are not of interest. Therefore, it is often beneficial to inspect the data in a coarse-grained, mezzo scale. One family of such coarse-grained analysis tools is based on manifold learning, which is particularly suitable for problems with multiple modalities, since it aims to capture the intrinsic geometric structure of the data and circumvents the need to specially tailor a solution for each modality. In manifold learning, the coarse-graining is typically carried out by the spectral analysis of a kernel built from the measurements. Here, we take a different approach by viewing the kernel as a coarse-grained representation of the data, utilizing its well-known Riemannian geometry. In particular, we focus on SPD kernels. The Riemannian geometry of SPD matrices is well-studied and enables us to define an interface for basic operations

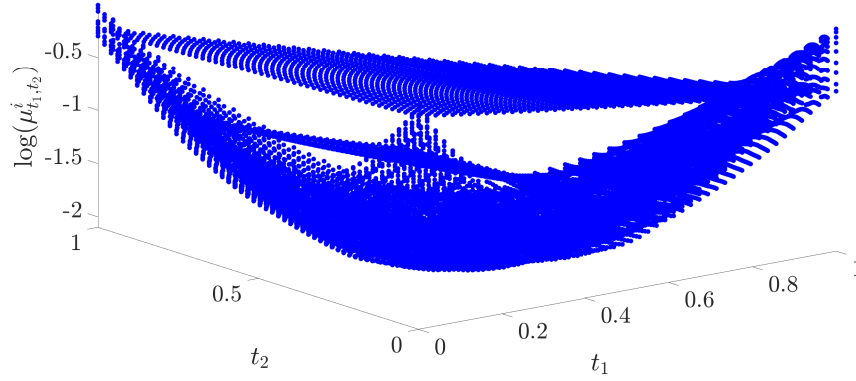


Figure 14: 3D eigenvalues flow diagram illustration for three sets of measurements sharing common eigenvectors .

on kernels. In addition, it facilitates a natural connection between pairs of kernels by considering the geodesic path induced by their Riemannian geometry. At the macro scale, we examine the flow of the spectra of the kernels along the geodesic path. We show that this flow, particularly, the way the spectrum changes along the geodesic, enables us, in a purely unsupervised manner, to derive a compact, yet informative, description of the mutual relationships between the measurements, in terms of their underlying spectral components. Based on this flow, we present new algorithms for extracting the common components and for identifying common and measurement-specific components.

In future work, we plan to extend the proposed framework to support more than two measurements. For instance, consider the kernels of three sets of measurements:  $\mathbf{K}_1$ ,  $\mathbf{K}_2$ , and  $\mathbf{K}_3$ . Instead of considering the geodesic path between two kernels:

$$\gamma_{1 \rightarrow 2}(t) = \mathbf{K}_1^{1/2} \left( \mathbf{K}_1^{-1/2} \mathbf{K}_2 \mathbf{K}_1^{-1/2} \right)^t \mathbf{K}_1^{1/2}$$

we plan to examine the following convex hull of three kernels:

$$\gamma_{1,2,3}(t_1, t_2) = (\gamma_{1 \rightarrow 2}(t_1))^{1/2} \left( (\gamma_{1 \rightarrow 2}(t_1))^{-1/2} \mathbf{K}_3 (\gamma_{1 \rightarrow 2}(t_1))^{-1/2} \right)^{t_2} (\gamma_{1 \rightarrow 2}(t_1))^{1/2}$$

This convex hull gives rise to a 3D eigenvalues flow diagram. An example for such a diagram is depicted in fig. 14. As can be seen, the 1D straight lines are extended to 2D flat planes, thereby, extending the proposed framework to three measurements in a natural way. Such extension schemes will be further studied and justified in future work.

# Supplementary material

## A Proofs

In this section, we provide proofs and justifications for the statements in the paper.

### A.1 Proof of proposition 1

**Proposition 3** *If  $v \in \mathbb{R}^n$  is an eigenvector of  $\mathbf{K}_1$  associated with the eigenvalue  $\mu_1$  and an eigenvector of  $\mathbf{K}_2$  associated with the eigenvalue  $\mu_2$ , i.e.  $v$  is a common eigenvector of  $\mathbf{K}_1$  and  $\mathbf{K}_2$ , then  $v$  is also an eigenvector of  $\gamma(t)$  with the corresponding eigenvalue:*

$$\mu_t = \mu_1^{1-t} \mu_2^t$$

**Proof 1** Let  $\mathbf{M} = \mathbf{K}_1^{-1/2} \mathbf{K}_2 \mathbf{K}_1^{-1/2}$ . By definition,  $v$  is an eigenvector of  $\mathbf{M}$  with eigenvalue:  $(\mu_1)^{-1} \mu_2$ . Therefore,  $v$  is also an eigenvector of  $\mathbf{M}^t$  with eigenvalue:  $\mu_1^{-(1-t)} \mu_2^t$ . Recalling that  $\gamma(t)$ , defined in eq. (2), can be recast as  $\gamma(t) = \mathbf{K}_1^{1/2} \mathbf{M}^t \mathbf{K}_1^{1/2}$  yields:

$$\begin{aligned} \gamma(t)v &= \mathbf{K}_1^{1/2} \mathbf{M}^t \mathbf{K}_1^{1/2} v \\ &= \mu_1^{1/2} \mu_1^{-t} \mu_2^t \mu_2^{1/2} v = \mu_1^{1-t} \mu_2^t v \end{aligned}$$

### A.2 Proof of proposition 2

**Proposition 4** *If  $v \in \mathbb{R}^n$  is an eigenvector of  $\mathbf{K}_1$  but not an eigenvector of  $\mathbf{K}_2$ , then  $v$  is not an eigenvector of  $\gamma(t)$ .*

**Proof 2** We prove by contradiction. Let  $\mu_1$  be the eigenvalue of  $\mathbf{K}_1$  associated with the eigenvector  $v$ . Assume that  $v$  is also an eigenvector of  $\gamma(t)$  with a corresponding eigenvalue  $\mu_t$ . That is

$$\mathbf{K}_1^{1/2} \left( \mathbf{K}_1^{-1/2} \mathbf{K}_2 \mathbf{K}_1^{-1/2} \right)^t \mathbf{K}_1^{1/2} v = \mu_t v$$

Since  $v$  is an eigenvector of  $\mathbf{K}_1$  we have

$$\mu_1^{1/2} \mathbf{K}_1^{1/2} \left( \mathbf{K}_1^{-1/2} \mathbf{K}_2 \mathbf{K}_1^{-1/2} \right)^t v = \mu_t v,$$

which can be recast as

$$\left( \mathbf{K}_1^{-1/2} \mathbf{K}_2 \mathbf{K}_1^{-1/2} \right)^t v = \mu_1^{-1/2} \mathbf{K}_1^{-1/2} \mu_t v = \mu_1^{-1} \mu_t v,$$

This entails that  $\mu_1^{-1} \mu_t$  is an eigenvalue of  $\left( \mathbf{K}_1^{-1/2} \mathbf{K}_2 \mathbf{K}_1^{-1/2} \right)^t$  with the corresponding eigenvector  $v$ . Consequently,  $(\mu_1^{-1} \mu_t)^{1/t}$  is an eigenvalue of  $\mathbf{K}_1^{-1/2} \mathbf{K}_2 \mathbf{K}_1^{-1/2}$ , i.e.

$$\mathbf{K}_1^{-1/2} \mathbf{K}_2 \mathbf{K}_1^{-1/2} v = (\mu_1^{-1} \mu_t)^{1/t} v$$

By exploiting again that  $v$  is an eigenvector of  $\mathbf{K}_1$  we have

$$\mu_1^{-1/2} \mathbf{K}_1^{-1/2} \mathbf{K}_2 v = (\mu_1^{-1} \mu_t)^{1/t} v$$

which gives

$$\mathbf{K}_2 v = \mu_1^{1/2} \mathbf{K}_1^{1/2} (\mu_1^{-1} \mu_t)^{1/t} v = \mu_1 (\mu_1^{-1} \mu_t)^{1/t} v$$

Therefore  $v$  is an eigenvector of  $\mathbf{K}_2$  with the corresponding eigenvalue  $\mu_1^{1-1/t} \mu_t^{1/t}$ .

## B Analyzing the spectral flow in a discrete model

To further the analysis, we examine the spectral flow diagram along the geodesic path in a specific use case involving a discrete graph setting. In the considered use case, the spectral components of the kernels are analytically known and have closed-form expressions, making the spectral flow mathematically tractable. More concretely, it enables us to present the marching along the geodesic path as filtering that preserves the common components and attenuates the influence of the measurement-specific components. In addition, we show that the diffusion induced by the kernel

matrices on the geodesic path is anisotropic, such that the induced diffusion distance exhibits some degree of invariance to the measurement-specific components. We remark that all the proofs of the statements presented in this section appear in section B.1.

We begin with the general description of the setting. Let  $G_x$  be an undirected weighted graph with vertex set  $V_X = \{u_1^x, u_2^x, \dots, u_n^x\}$  and affinity matrix  $\mathbf{A}_x$ , and let  $G_y$  and  $G_z$  be two undirected weighted graphs with vertex sets  $V_Y = \{u_1^y, u_2^y, \dots, u_m^y\}$  and  $V_Z = \{u_1^z, u_2^z, \dots, u_m^z\}$  and with affinity matrices  $\mathbf{A}_y$  and  $\mathbf{A}_z$ , respectively. Consider a permutation:  $\pi : V_Y \rightarrow V_Z$ , so that the vertices of  $G_z$  can be viewed as a permutation of the vertices of  $G_y$ , namely, any  $u^z \in V_Z$  can be written as  $u^z = \pi(u^y)$  for  $u^y \in V_Y$ . Finally, let  $G_{xy}$  be the product graph of  $G_x$  and  $G_y$  with the following affinity matrix

$$\mathbf{A}_{xy} = \mathbf{A}_x \times \mathbf{1}_m + \mathbf{1}_n \times \mathbf{A}_y$$

and let  $G_{xz}$  be the product graph of  $G_x$  and  $G_z$  with the following affinity matrix

$$\mathbf{A}_{xz} = \mathbf{A}_x \times \mathbf{1}_m + \mathbf{1}_n \times \mathbf{A}_z$$

The considered setting here is different than the continuous manifold setting considered in the paper. Yet, we make the following analogy with the problem setting described in Section 2. The graphs  $G_x$ ,  $G_y$ , and  $G_z$  correspond to the hidden manifolds  $\mathcal{M}_x$ ,  $\mathcal{M}_y$ , and  $\mathcal{M}_z$ , and the dependency between the hidden manifolds conveyed by the joint distribution of the samples  $(x, y, z) \in \mathcal{M}_x \times \mathcal{M}_y \times \mathcal{M}_z$  is encoded here by the permutation  $\pi$ . In this discrete setting, a measurement is represented by a triplet  $(x, y, z)$  of nodes, where  $x \in V_X$ ,  $y \in V_Y$  and  $z \in V_Z$ , giving rise to a pair of nodes  $(x, y)$  and  $(x, z)$  in the product graphs  $G_{xy}$  and  $G_{xz}$ , respectively. We remark that for a tighter relationship between the discrete and continuous models, a discrete model consisting of multiple permutations should have been considered, allowing for dependencies between the nodes of  $G_y$  and  $G_z$  with the nodes of  $G_x$ . However, for simplicity, we assume there exists a single fixed permutation  $\pi$ , which does not depend on  $V_X$ . As we will discuss in the sequel, this relaxation makes the problem at hand more challenging. In G we discuss the analogy between the discrete and continuous models in more detail.

To make the analysis simple to present, we focus on a use case involving cycle (ring) graphs. Namely, we consider the following affinity matrix  $\mathbf{A}_x \in \mathbb{R}^{n \times n}$

$$\mathbf{A}_x = \begin{pmatrix} 1 & 1/2 & 0 & \dots & 0 & 1/2 \\ 1/2 & 1 & 1/2 & 0 & \dots & 0 \\ 0 & 1/2 & 1 & 1/2 & \dots & 0 \\ \vdots & \ddots & \ddots & \ddots & \ddots & \vdots \\ 0 & \dots & 0 & 1/2 & 1 & 1/2 \\ 1/2 & 0 & \dots & 0 & 1/2 & 1 \end{pmatrix} \quad (20)$$

where  $\mathbf{A}_y, \mathbf{A}_z \in \mathbb{R}^{m \times m}$  are defined in a similar manner. We remark that our analysis can be extended with only minor modifications to d-regular graphs as well.

We conclude the description of the setting with a convenient notation. For brevity, we will refer to the vertices of  $G_x$ ,  $G_y$  and  $G_z$  by their respective indices, so that  $V_X = \{1, \dots, n\}$ ,  $V_Y = \{1, \dots, m\}$ ,  $V_Z = \{1, \dots, m\}$ , and  $\pi : \{1, \dots, m\} \rightarrow \{1, \dots, m\}$ . Consequently, each vertex in the product graphs can be indexed by a pair  $(x, y) \in \{1, 2, \dots, n\} \times \{1, 2, \dots, m\}$  or by a single index using this column-stack bijective mapping function  $r(x, y) : \{1, 2, \dots, n\} \times \{1, 2, \dots, m\} \rightarrow \{1, 2, \dots, mn\}$ , given by:

$$r(x, y) = (x - 1)m + y. \quad (21)$$

The inverse mapping  $x(r) : \{1, 2, \dots, mn\} \rightarrow \{1, 2, \dots, n\}$  and  $y(r) : \{1, 2, \dots, mn\} \rightarrow \{1, 2, \dots, m\}$  are given by:

$$x(r) = 1 + \left\lfloor \frac{r}{m} \right\rfloor \quad (22)$$

$$y(r) = 1 + r \bmod (r, m). \quad (23)$$

Throughout this section we will use both indices interchangeably.

The first step in the computation of the spectral flow diagram is the construction of the kernels  $\mathbf{K}_{xy}$  and  $\mathbf{K}_{xz}$  by applying a two-step normalization to the affinity matrices  $\mathbf{A}_{xy}$  and  $\mathbf{A}_{xz}$ , respectively, according to section 3.2. In the considered cycle graphs, the sum of the rows and the columns of  $\mathbf{A}_x$ ,  $\mathbf{A}_y$  and  $\mathbf{A}_z$  is fixed and equals 2. By construction, we get that the sum of the rows and the columns of  $\mathbf{A}_{xy}$  and  $\mathbf{A}_{xz}$  is fixed and equals 4. Accordingly, the kernels  $\mathbf{K}_{xy}$  and  $\mathbf{K}_{xz}$  are given by:

$$\mathbf{K}_{xy} = \frac{1}{4} \mathbf{A}_{xy}; \quad \mathbf{K}_{xz} = \frac{1}{4} \mathbf{A}_{xz}$$

Applying EVD to  $\mathbf{K}_{xy}$  yields

$$\mathbf{K}_{xy} = \mathbf{V}_{xy} \mathbf{S}_{xy} \mathbf{V}_{xy}^T,$$

where  $\mathbf{S}_{xy}$  is a diagonal matrix whose entries are the eigenvalues of  $\mathbf{K}_{xy}$ , denoted by  $\mu_{xy}^{(r)}$ , and  $\mathbf{V}_{xy}$  is a matrix whose columns consist of the eigenvectors of  $\mathbf{K}_{xy}$ , denoted by  $v_{xy}^{(r)}$ , for  $r = 1, \dots, nm$ . Note that according to our notation, the index  $r$  can be replaced by a double index  $(k, l)$  such that  $k = x(r)$  and  $l = y(r)$ .

**Lemma 1** *The spectral components of  $\mathbf{K}_{xy}$  are given by:*

$$\begin{aligned} v_{xy}^{(k,l)}(r) &= v_x^k(x(r)) v_y^l(y(r)) \\ \mu_{xy}^{(k,l)} &= \frac{1}{2}(\mu_x^k + \mu_y^l) \end{aligned} \quad (24)$$

for  $r = 1, \dots, nm$ , where  $\{(\mu_x^k, v_x^k)\}_{k=1}^n$  is the set of eigenvalues and eigenvectors of  $\mathbf{K}_x = \frac{1}{2}\mathbf{A}_x$ , and  $\{(\mu_y^l, v_y^l)\}_{l=1}^m$  is the set of eigenvalues and eigenvectors of  $\mathbf{K}_y = \frac{1}{2}\mathbf{A}_y$ .

The proof appears in proof 8.

Since  $G_x$  and  $G_y$  are cycle graphs, the eigenvalues of  $\mathbf{K}_x$  and  $\mathbf{K}_y$  are given by:

$$\begin{aligned} \mu_x^k &= \frac{1}{2} \left( 1 + \cos \left( \frac{2\pi(k-1)}{n} \right) \right) \\ \mu_y^u &= \frac{1}{2} \left( 1 + \cos \left( \frac{2\pi(u-1)}{m} \right) \right) \end{aligned}$$

and the eigenvectors are given by:

$$\begin{aligned} v_x^k(x) &= \alpha(k) \sqrt{\frac{1}{n}} \cos \left( \frac{\pi(k-1)}{n} (x-1) + \phi(k, n) \right) \\ v_y^l(y) &= \alpha(l) \sqrt{\frac{1}{m}} \cos \left( \frac{\pi(l-1)}{m} (y-1) + \phi(l, m) \right) \end{aligned}$$

where  $\alpha(k)$  is a scaling function given by:

$$\alpha(k) = \begin{cases} 1, & k = 1 \\ \sqrt{2}, & k > 1 \end{cases} \quad (25)$$

and  $\phi(k, n)$  is a phase function given by:

$$\phi(k, n) = \frac{\pi}{2} \left\lfloor \frac{k}{\frac{n+1}{2} + 1} \right\rfloor \quad (26)$$

Plugging these explicit expressions into 24 gives explicit expressions to the spectral components of  $\mathbf{K}_{xy}$ .

Suppose that the eigenvalues of  $\mathbf{K}_{xy}$  are ordered according to  $r(k, l)$  in an ascending order. In this order, the eigenvectors with indices  $r = m+1, 2m+1, \dots, (n-1)m+1$ , such that  $y(r) = 1$ , are the (common) eigenvectors of  $\mathbf{K}_x$ , whereas all other eigenvectors of  $\mathbf{K}_{xy}$  consist of non-trivial (measurement-specific) eigenvectors of  $\mathbf{K}_y$ .

Similarly, the EVD of  $\mathbf{K}_{xz}$  is given by:

$$\mathbf{K}_{xz} = \mathbf{V}_{xz} \mathbf{S}_{xz} \mathbf{V}_{xz}^T,$$

where  $\mathbf{S}_{xz} = \mathbf{S}_{xy}$  and

$$\mathbf{V}_{xz} = \mathbf{\Pi} \mathbf{V}_{xy},$$

where  $\mathbf{\Pi}$  is defined by:

$$\mathbf{\Pi} = \mathbf{1}_n \otimes \mathbf{P}_\pi.$$

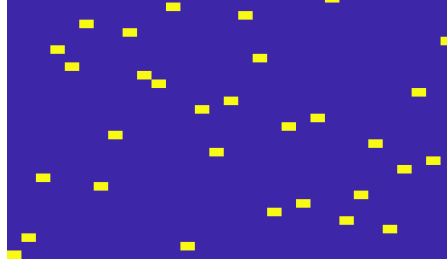
The computation of the spectral flow diagram continues with the construction of a point on the geodesic path on the SPD manifold connecting  $\mathbf{K}_{xy}$  and  $\mathbf{K}_{xz}$ , denoted by  $\gamma(t)$  for  $t \in [0, 1]$ . By definition,  $\gamma(t)$  can be recast as:

$$\gamma(t) = \mathbf{K}_{xy}^{1/2} \mathbf{M}^t \mathbf{K}_{xy}^{1/2}$$

where  $\mathbf{M} \triangleq \mathbf{K}_{xy}^{-1/2} \mathbf{K}_{xz} \mathbf{K}_{xy}^{-1/2}$ . By the EVD of  $\mathbf{K}_{xy}$  and  $\mathbf{K}_{xz}$ ,  $\mathbf{M}$  can be written as:

$$\mathbf{M} = \mathbf{V}_{xy} \mathbf{S}_{xy}^{-\frac{1}{2}} \mathbf{V}_{xy}^T \mathbf{V}_{xz} \mathbf{S}_{xy} \mathbf{V}_{xz}^T \mathbf{V}_{xy} \mathbf{S}_{xy}^{-\frac{1}{2}} \mathbf{V}_{xy}^T$$



Figure 15: The randomly drawn permutation matrix:  $\mathbf{P}_\pi$ .

Recalling that  $\mathbf{V}_{xz} = \Pi \mathbf{V}_{xy}$ , we can further simplify the expression and recast it only using  $\Pi$  and the spectral components of  $G_{xy}$ :

$$\mathbf{M} = \mathbf{V}_{xy} \mathbf{S}_{xy}^{-\frac{1}{2}} \mathbf{V}_{xy}^T \Pi \mathbf{V}_{xy} \mathbf{S}_{xy} \mathbf{V}_{xy}^T \Pi^T \mathbf{V}_{xy} \mathbf{S}_{xy}^{-\frac{1}{2}} \mathbf{V}_{xy}^T$$

For brevity, we discard the subscripts  $xy$ , so that we get:

$$\mathbf{M} = \underbrace{\mathbf{V} \mathbf{S}^{-\frac{1}{2}} \underbrace{\mathbf{V}^T \Pi \mathbf{V} \mathbf{S}}_{\triangleq \mathbf{C}} \underbrace{\mathbf{V}^T \Pi^T \mathbf{V}}_{\triangleq \mathbf{B}^T} \mathbf{S}^{-\frac{1}{2}} \mathbf{V}^T}_{\triangleq \mathbf{C}_S} \quad (27)$$

The notation in eq. (27) prescribes a 5-step calculation:

1. Calculate  $\mathbf{B} \triangleq \mathbf{V}^T \Pi \mathbf{V}$ .
2. Using  $\mathbf{B}$ , compute  $\mathbf{C} \triangleq \mathbf{B} \mathbf{S} \mathbf{B}^T$ .
3. Perform rows and columns multiplication according to the diagonal matrix  $\mathbf{S}^{-\frac{1}{2}}$  in order to compute:  $\mathbf{C}_S \triangleq \mathbf{S}^{-\frac{1}{2}} \mathbf{C} \mathbf{S}^{-\frac{1}{2}}$ .
4. Rotate  $\mathbf{C}_S$  according to  $\mathbf{V}$  in order to obtain  $\mathbf{M} = \mathbf{V} \mathbf{C}_S \mathbf{V}^T$ .
5. Raise  $\mathbf{M}$  to the power of  $t$  and multiply by  $\mathbf{K}^{-\frac{1}{2}}$  from both sides in order to obtain  $\gamma(t) = \mathbf{K}^{-\frac{1}{2}} \mathbf{M}^t \mathbf{K}^{-\frac{1}{2}}$ .

In the sequel, we follow this procedure step-by-step. Throughout the derivation, in addition to general results, we present an illustration based on a specific simulation with the following parameters:

$$m = 31; n = 11$$

and a permutation  $\pi$  that was drawn uniformly at random. The randomly drawn realization of the permutation matrix  $\mathbf{P}_\pi$  is depicted in fig. 15.

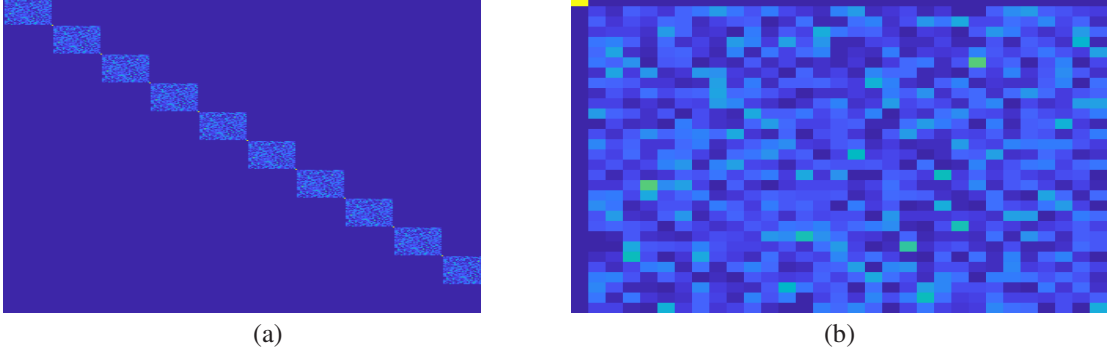
The elements of the matrix  $\mathbf{B} \triangleq \mathbf{V}^T \Pi \mathbf{V}$  are given by:

$$\mathbf{B}_{i,j} = \langle v_{xy}^{(x(i),y(i))}, v_{xz}^{(x(j),z(j))} \rangle.$$

**Proposition 5** *The matrix  $\mathbf{B}$  is block diagonal consisting of  $n$  identical  $m \times m$  matrices  $\mathbf{b}$  so that  $\mathbf{b}_{1,1} = 1$ ,  $\mathbf{b}_{1,i} = 0$  and  $\mathbf{b}_{i,1} = 0$  for  $i > 1$ . In addition, for any  $1 < l, l' \leq m$ , the probability to randomly pick a permutation for which  $|\mathbf{b}_{l,l'}| \leq \alpha$  is upper-bounded by:*

$$P(|\mathbf{b}_{l,l'}| \geq \alpha) \leq \frac{1}{\alpha} \sqrt{\frac{2}{m}}$$

The proof appears in proof 10. The obtained matrix  $\mathbf{B}$  in the simulation is presented in fig. 16 (a) and one of its blocks  $\mathbf{b}$  is presented in fig. 16 (b). We observe that  $\mathbf{B}$  is indeed a block-diagonal matrix consisting of  $n$  identical blocks, where each block admits the structure specified in proposition 5. Namely, the first element of each block is 1, the remaining elements in the first row and column are 0, and the rest of the entries are unstructured and small.

Figure 16: The obtained matrix:  $\mathbf{B}$  (a) and its block's structure (b).

Next, we compute  $\mathbf{C} \triangleq \mathbf{B}^T \mathbf{S} \mathbf{B}$ . Recall that  $\mathbf{S}$  is a diagonal matrix consisting of the eigenvalues of  $\mathbf{K}_{xy}$  and its elements are given according to eq. (24) by:

$$\begin{aligned} \mathbf{S}(r, r) = \mu_{xy}^{(x(r), y(r))} &= \frac{1}{2}(\mu_x^{x(r)} + \mu_y^{y(r)}) \\ &= \frac{1}{2} + \frac{1}{4} \left( \cos \left( \frac{2\pi(x(r)-1)}{n} \right) + \cos \left( \frac{2\pi(y(r)-1)}{m} \right) \right) \end{aligned}$$

fig. 17 presents the diagonal of  $\mathbf{S}$  in the simulation. Since the multiplicity of the eigenvalues of  $\mathbf{K}_x$  and  $\mathbf{K}_y$  is 2, i.e.:

$$\begin{aligned} \mu_x^k &= \mu_x^{n-(k-2)} \\ \mu_y^l &= \mu_y^{m-(l-2)} \end{aligned}$$

the multiplicity of the eigenvalues of  $\mathbf{K}_{xy}$  is 4 :

$$\mu_{xy}^{(x(r), y(r))} = \mu_{xy}^{(n-(x(r)-2), y(r))} = \mu_{xy}^{(x(r), m-(y(r)-2))} = \mu_{xy}^{(n-(x(r)-2), m-(y(r)-2))}$$

Therefore, in fig. 17, as well as in all subsequent similar figures, we depict only 1/4 of the eigenvalues of  $\mathbf{K}_{xy}$ , which are unique. More specifically, we show the diagonal entries of  $\mathbf{S}$  with indices  $r(x, y)$  sorted in ascending order, where  $x = 1, \dots, \frac{n+1}{2}$  and  $y = 1, \dots, \frac{m+1}{2}$ .

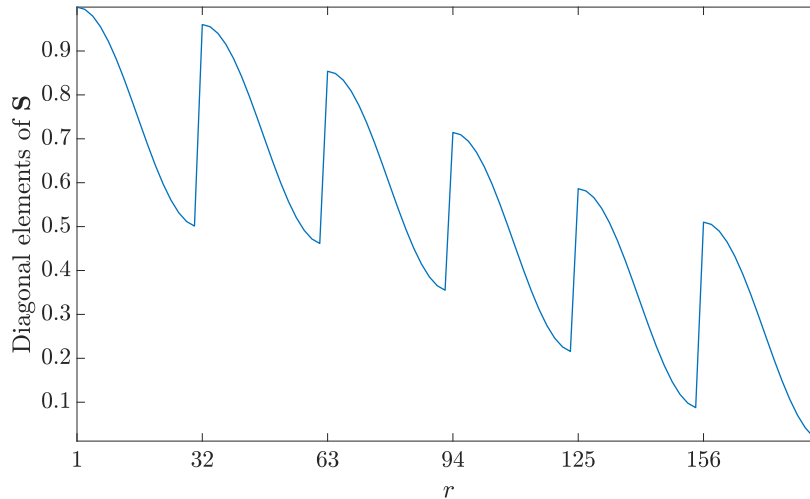
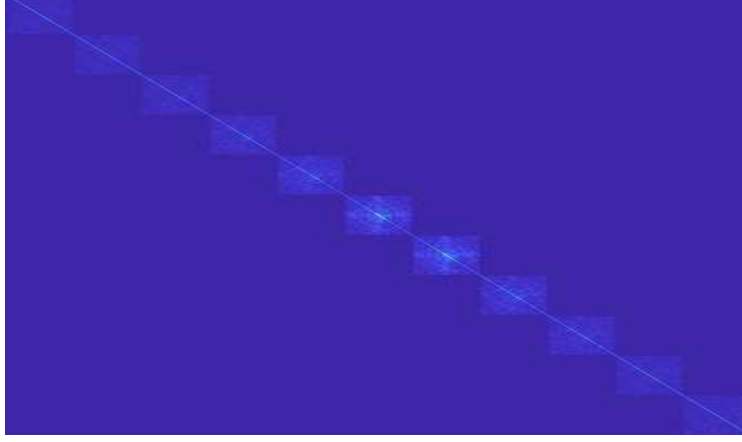
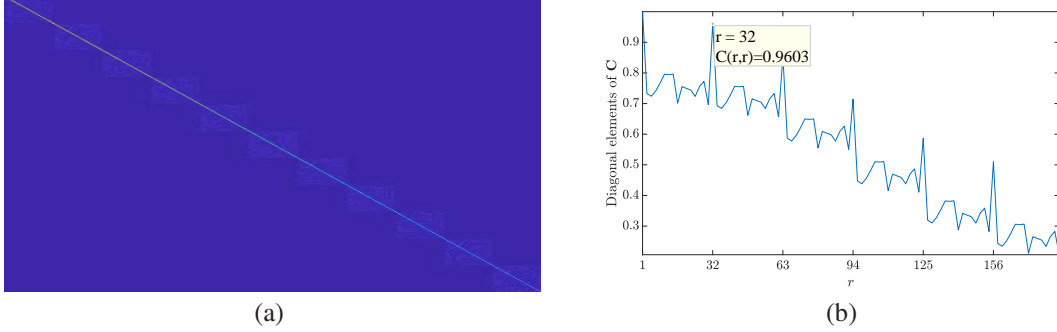
Figure 17: The diagonal entries of  $\mathbf{S}$ , i.e., the eigenvalues of  $\mathbf{K}_{xy}$  sorted according to the mapping  $r(x, y)$  in an ascending order.

fig. 18 (a) depicts the obtained matrix  $\mathbf{C}$  in the simulation and fig. 18 (b) depicts its diagonal elements. We observe that the off-diagonal elements of  $\mathbf{C}$  are significantly smaller than the diagonal elements. Following this empirical results, we approximate  $\mathbf{C}$  as a diagonal matrix.

Figure 19: The obtained matrix  $\mathbf{C}_S$ .Figure 18: (a) The obtained matrix  $\mathbf{C}$ . (b) The diagonal elements of  $\mathbf{C}$ .

Focusing on the diagonal of  $\mathbf{C}$  reveals that the elements corresponding to the common eigenvectors at indices  $m + 1, 2m + 1, \dots, (n - 1)m + 1$  are identical to the values in  $\mathbf{S}$ . For example, the empirical value of the diagonal element at index  $m + 1 = 32$  is  $\mathbf{C}(32, 32) = 0.9603$ . This value admits the analytical expression for  $\mathbf{S}(32, 32)$ , which is given by substituting  $r = 32$  in B:

$$\begin{aligned} \mathbf{S}(32, 32) &= \frac{1}{2} + \frac{1}{4} \left( \cos \left( \frac{2\pi (x(32) - 1)}{11} \right) + \cos \left( \frac{2\pi (y(32) - 1)}{31} \right) \right) \\ &= \frac{1}{2} + \frac{1}{4} \left( \cos \left( \frac{2\pi (2 - 1)}{11} \right) + 1 \right) = 0.9603. \end{aligned}$$

From  $\mathbf{C}$ , we compute the matrix  $\mathbf{C}_S \triangleq \mathbf{S}^{-\frac{1}{2}} \mathbf{C} \mathbf{S}^{-\frac{1}{2}}$ . The resulting matrix is presented in fig. 19. Similarly to  $\mathbf{C}$ , the matrix  $\mathbf{C}_S$  has small off-diagonal elements and is close to a diagonal matrix as well.

The next step is to compute  $\mathbf{M} = \mathbf{V} \mathbf{C}_S \mathbf{V}^T$ , raise it to the power of  $t$ , and then compute the geodesic path  $\gamma(t) = \mathbf{K}^{-\frac{1}{2}} \mathbf{M}^t \mathbf{K}^{-\frac{1}{2}}$ .

**Proposition 6** *The geodesic path  $\gamma(t)$  can be recast as follows:*

$$\gamma(t) = \mathbf{V} \mathbf{F}_t \mathbf{V}^T$$

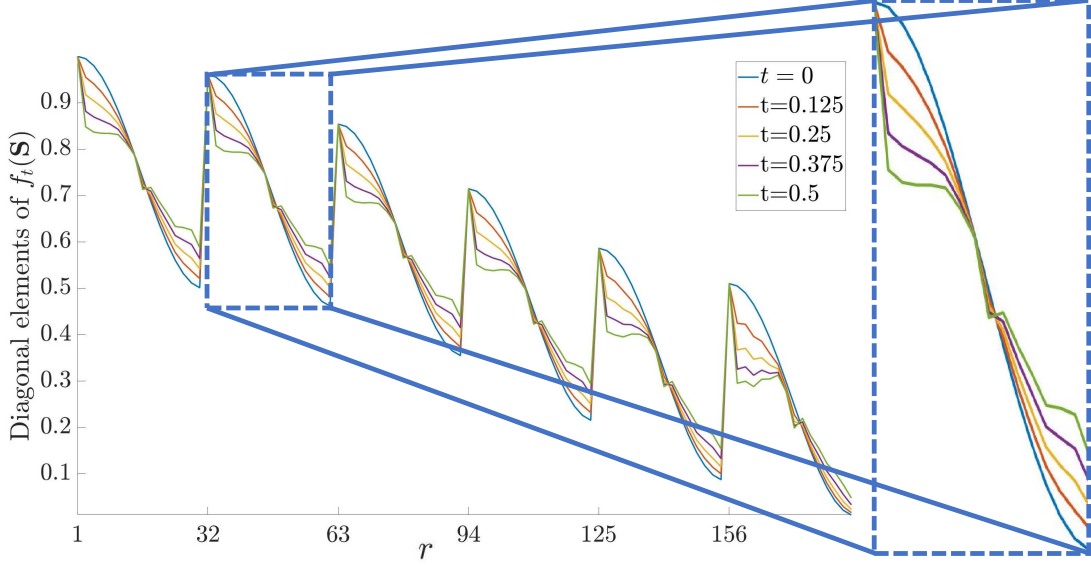
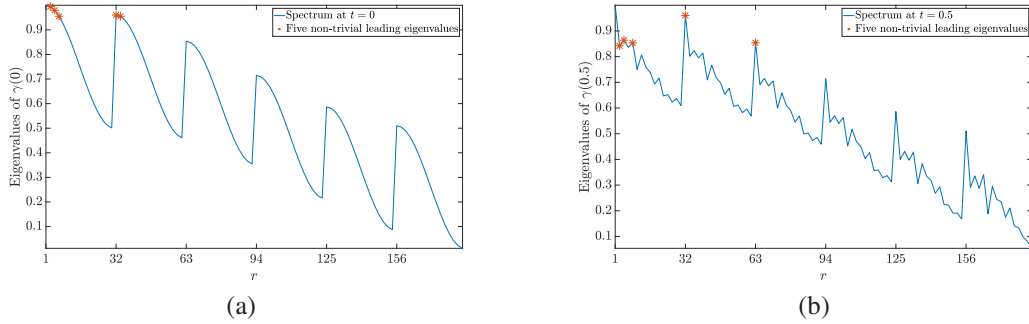
where  $\mathbf{F}_t$  is given by:

$$\mathbf{F}_t \triangleq \mathbf{S}^{\frac{1}{2}} \mathbf{C}_S^t \mathbf{S}^{\frac{1}{2}}$$

The proof appears in proof 11.

In light of the empirical result, assuming that  $\mathbf{C}_S$  is approximately diagonal, by Taylor expansion, we have that  $\mathbf{C}_S^t$  is approximately diagonal for small  $t$  values. Therefore, for small  $t$ ,  $\gamma(t)$  can be approximated by:

$$\gamma(t) \simeq \mathbf{V} \mathbf{C}_S^t \mathbf{V}^T \quad (28)$$

Figure 20: The diagonal elements of  $f_t(\mathbf{S})$  for several values of  $t$ .Figure 21: (a) The spectrum of  $\gamma(0) = \mathbf{K}_{xy}$  and (b) the spectrum of  $\gamma(0.5)$ . The 5 top eigenvalues are marked by red asterisks.

This representation implies that marching along the geodesic path (near  $t = 0$ ) is analogous to spectral graph filtering with a filter  $f_t(\cdot)$  that is applied to the graph spectrum:  $f_t(\mathbf{S}) = \mathbf{S}\mathbf{C}_{\mathbf{S}}^t$ . For illustration, in fig. 20, we pick 5 points along the geodesic path at  $t \in \{0, 0.125, 0.25, 0.375, 0.5\}$  and depict  $f_t(\mathbf{S})$ .

We observe that at  $t = 0$ , the obtained spectrum coincides with the spectrum of  $\mathbf{K}_{xy}$ . In the inset, we also observe that eigenvalues at indices  $r = m + 1, 2m + 1, \dots$ , corresponding to common eigenvectors, remain unchanged when  $t$  increases (in the inset we see it at index  $33 = 1 + m$  since  $m = 32$ ). Conversely, all other eigenvalues, corresponding to eigenvectors with measurement-specific components, vary, where the dominant ones (with indices  $r$  such that  $y(r)$  is small) are attenuated and the others are enhanced.

In fig. 21, we plot the obtained spectrum of  $\gamma(t)$  without using the approximation in eq. (28). In fig. 21 (a) we plot the spectrum for  $t = 0$  and in fig. 21 (b) for  $t = 0.5$ . In each plot, we mark the five top eigenvalues by red asterisks.

We observe that for  $t = 0$ , besides the trivial eigenvalue, only one eigenvalue among the top five eigenvalues corresponds to a common eigenvector. In contrast, for  $t = 0.5$ , two eigenvalues among the top five correspond to common eigenvectors. This implies that  $\gamma(t)$  at  $t = 0.5$  attenuates the non-common eigenvectors, and as a consequence, the common eigenvectors appear higher in the spectrum.

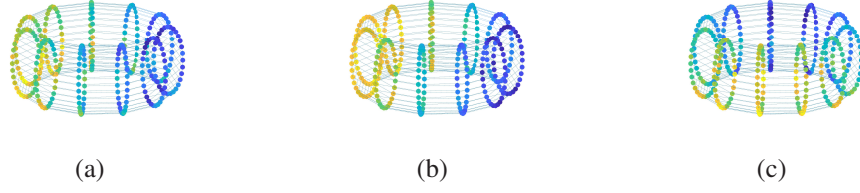


Figure 22: The diffusion patterns displayed on the nodes of  $G_{xy}$ , namely  $V_X \times V_Y$ . Since  $G_x$  and  $G_y$  are cycle graphs, we plot  $G_{xy}$  as a 2-torus in  $\mathbb{R}^3$ . The color in (a), (b), and (c) corresponds to the diffusion pattern obtained by  $\gamma^s(0.25)\delta_{p_1}$ ,  $\gamma^s(0.25)\delta_{p_2}$ , and  $\gamma^s(0.25)\delta_{p_3}$ , respectively.

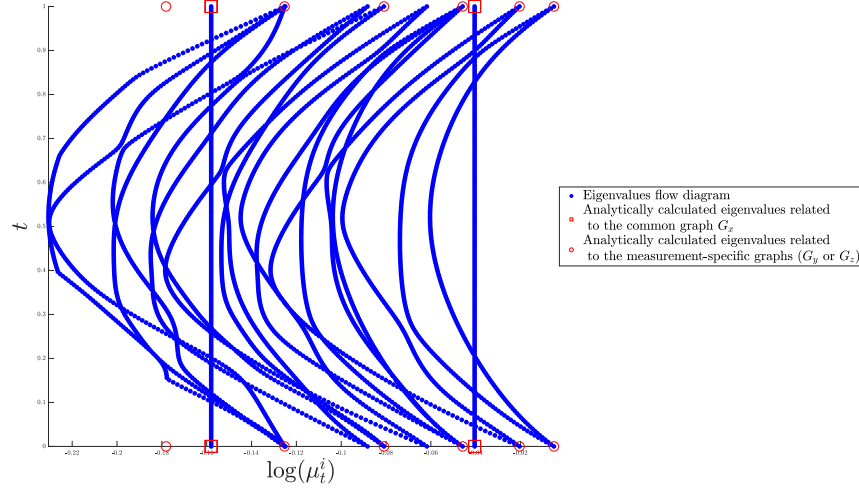


Figure 23: Eigenvalues flow diagram corresponding to the considered use case. The analytic eigenvalues corresponding to the common graph  $G_x$  are marked by squares and the analytic eigenvalues corresponding to the measurement-specific graphs ( $G_y$  or  $G_z$ ) are marked by circles.

Next, we explore the diffusion distance<sup>2</sup> induced by  $\gamma(t)$  in light of the above spectral analysis. The diffusion distance induced by the kernel  $\gamma(t)$  between two graph nodes:  $p_1 = r(x_1, y_1)$  and  $p_2 = r(x_2, y_2)$  is given by

$$D_s^2(p_1, p_2, t) = \|\gamma^s(t)\delta_{p_1} - \gamma^s(t)\delta_{p_2}\|^2, \quad (29)$$

where  $s > 0$  represent the number of diffusion steps, and  $\delta_{p_1}$  and  $\delta_{p_2}$  are vectors, whose elements at  $p_1$  and  $p_2$  equal 1, respectively, and all other elements equal 0.

We pick three points:

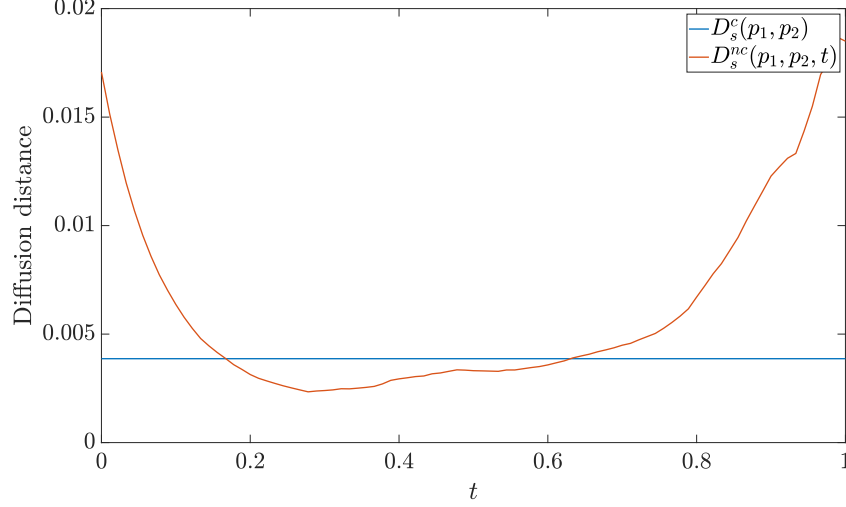
$$\begin{aligned} p_1 &= r(6, 16) \\ p_2 &= r(6, 19) \\ p_3 &= r(9, 16) \end{aligned}$$

We note that  $p_1$  and  $p_2$  share the same vertices with respect to  $G_x$ , whereas  $p_1$  and  $p_3$  share the same vertices with respect to  $G_y$ . We compute  $\gamma^s(0.25)\delta_{p_i}$  for  $i = 1, 2, 3$  and for  $s = 50$ , and display the results in fig. 22.

We observe that the diffusion patterns initialized at  $p_1$  and  $p_2$ , whose common coordinate  $x(p_1) = x(p_2) = 6$  is the same, are similar, leading to small diffusion distance  $D_s^2(p_1, p_2, 0.25)$ . Conversely, the diffusion patterns initialized at  $p_1$  and  $p_3$ , whose common coordinate  $6 = x(p_1) \neq x(p_3) = 9$  are not equal, are different, leading to large diffusion distance  $D_s^2(p_1, p_3, 0.25)$ . This demonstrates the fact that the diffusion distance is more sensitive to distances with respect to  $G_x$  than to distances with respect to  $G_y$ , thereby facilitating the discovery of the common components.

Next, we compute the eigenvalues flow diagram according to algorithm 1 with  $N_t = 200$  and  $K = 20$ . The resulting diagram appears in fig. 23. We observe that the eigenvalues which are associated with the common eigenvectors

<sup>2</sup>We consider the variant of the diffusion distance eq. (9) with respect to  $\gamma(t)$ .

Figure 24:  $D_s^c(p_1, p_2, t)$  and  $D_s^{nc}(p_1, p_2, t)$  along the geodesic path.

are indeed constant with respect to  $t$ , while the rest are highly attenuated. Therefore, we use the EVD of  $\gamma(t) = \mathbf{V}_{\gamma(t)} \mathbf{S}_{\gamma(t)} \mathbf{V}_{\gamma(t)}^T$ , and recast the diffusion distance as:

$$D_s^2(p_1, p_2, t) = \sum_{r=1}^{mn} \mathbf{S}_{\gamma(t)}^2(r, r) (\mathbf{V}_{\gamma(t)}(p_1, r) - \mathbf{V}_{\gamma(t)}(p_2, r))^2.$$

Let  $\mathcal{N}_c(t)$  denote the set of indexes  $r$  corresponding to the common eigenvectors of  $\gamma(t)$ , namely,  $r = 1, m+1, 2m+1, \dots$ . Accordingly,  $D_s^2(p_1, p_2, t)$  can be decomposed as follows:

$$D_s^2(p_1, p_2, t) = D_s^c(p_1, p_2, t) + D_s^{nc}(p_1, p_2, t),$$

where

$$D_s^c(p_1, p_2, t) \triangleq \sum_{r \in \mathcal{N}_c(t)} \mathbf{S}_{\gamma(t)}^2(r, r) (\mathbf{V}_{\gamma(t)}(p_1, r) - \mathbf{V}_{\gamma(t)}(p_2, r))^2,$$

and

$$D_s^{nc}(p_1, p_2, t) \triangleq \sum_{r \notin \mathcal{N}_c(t)} \mathbf{S}_{\gamma(t)}^2(r, r) (\mathbf{V}_{\gamma(t)}(p_1, r) - \mathbf{V}_{\gamma(t)}(p_2, r))^2.$$

This decomposition enables us to examine the contribution of the common and non-common eigenvectors to the diffusion distance, separately. In fig. 24, we plot the resulting  $D_s^c(p_1, p_2, t)$  and  $D_s^{nc}(p_1, p_2, t)$ . We observe that  $D_s^c(p_1, p_2, t)$  is constant with respect to  $t$ , which coincides with the fact that the eigenvalues corresponding to the common eigenvectors are fixed along the geodesic path. Conversely, we observe that  $D_s^{nc}(p_1, p_2, t)$  is highly dependent of  $t$  and attains high values near the boundaries  $t = 0$  and  $t = 1$  and low values in the middle of the geodesic path, implying on some degree of invariance to the measurement-specific eigenvectors.

The consequence of this empirical result is that the diffusion distance computed based on  $\gamma(t = 0)$  and  $\gamma(t = 1)$ , namely,  $\mathbf{K}_{xy}$  and  $\mathbf{K}_{xz}$ , is dominated by the non-common components. In contrast, the diffusion distance based on  $\gamma(t)$  from the middle of the geodesic path is dominated by the common components.

Thus far, the analysis was focused on a specific permutation, but we report that according to our empirical study, similar trends are obtained for different permutation realizations. In the sequel, we derive an expression for the average spectrum that is obtained by taking into account all possible permutations.

Each realization of  $\pi$  induces a kernel  $\mathbf{K}_{xz}$  and a corresponding geodesic path  $\gamma_\pi(t)$ . Each  $\gamma_\pi(t)$  starts at a fixed matrix  $\mathbf{K}_{xy}$  but ends at different  $\mathbf{K}_{xz}$  according to the permutation, where the dependency of  $\mathbf{K}_{xz}$  on  $\pi$  is omitted for simplicity. Suppose now that  $\pi$  is drawn uniformly at random. For generalization, we consider now the “mean path”  $\bar{\gamma}(t)$  that starts at the fixed  $\mathbf{K}_{xy}$  and ends at  $\bar{\mathbf{K}}_{xz}$ , defined by

$$\bar{\gamma}(t) = \frac{1}{m!} \sum_{\pi} \gamma_\pi(t),$$



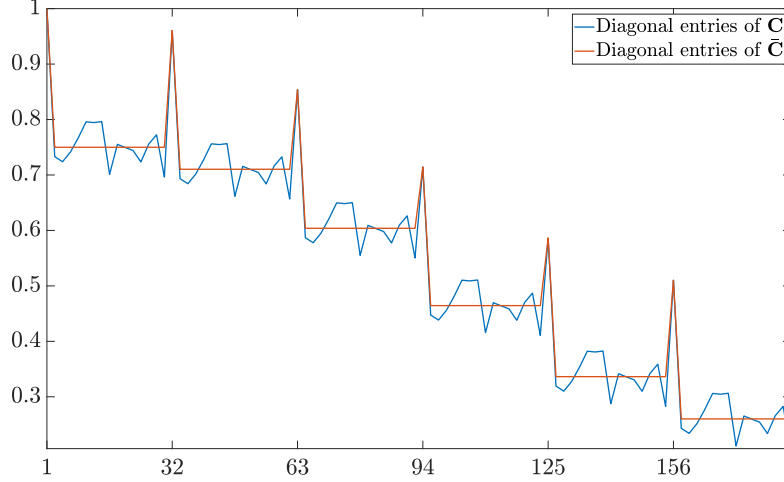


Figure 25: The diagonal elements of  $\mathbf{C}_\pi$  compared with the analytic expression for the diagonal elements of  $\overline{\mathbf{C}}$ .

where

$$\overline{\mathbf{K}}_{xz} = \frac{1}{m!} \sum_{\pi} \mathbf{K}_{xz}.$$

**Proposition 7** *The mean matrix  $\overline{\mathbf{C}}$ , defined by*

$$\overline{\mathbf{C}} = \frac{1}{m!} \sum_{\pi} \mathbf{C}_\pi$$

where  $\mathbf{C}_\pi$  is defined as in steps 1 and 2 with the permutation  $\pi$ , is a diagonal matrix, whose diagonal elements are given by:

$$\bar{c}(r) = \frac{1}{2} + \frac{1}{4} \cos\left(\frac{2\pi(x(r)-1)}{n}\right) + \frac{1}{4} \delta(y(r), 1)$$

where  $1 \leq r \leq mn$ .

The proof appears in proof 12. We note that  $\bar{c}(r)$  is the  $r$ th eigenvalue of a kernel  $\tilde{\mathbf{K}}_x$ , which is the diffusion kernel corresponding to the product graph  $G_x \times Q_m$ , where  $Q_m$  is the complete graph with  $m$  nodes.

In fig. 25 we overlay  $\bar{c}(r)$  on fig. 18(b). As can be seen, the preservation of the common eigenvectors and the attenuation of the non-common eigenvectors are evident when considering the mean as well as when considering a particular permutation.

As we show in the next proposition, the fact that  $\mathbf{C}$  is approximately diagonal can be made more precise.

**Proposition 8** *Let  $\pi$  be a permutation drawn uniformly at random. The off-diagonal entries of  $\mathbf{C}$  satisfy:*

$$P(|\mathbf{C}_{i,j}| \geq \alpha) \leq \frac{1}{\alpha} \sqrt{\frac{1}{32(m-1)}}$$

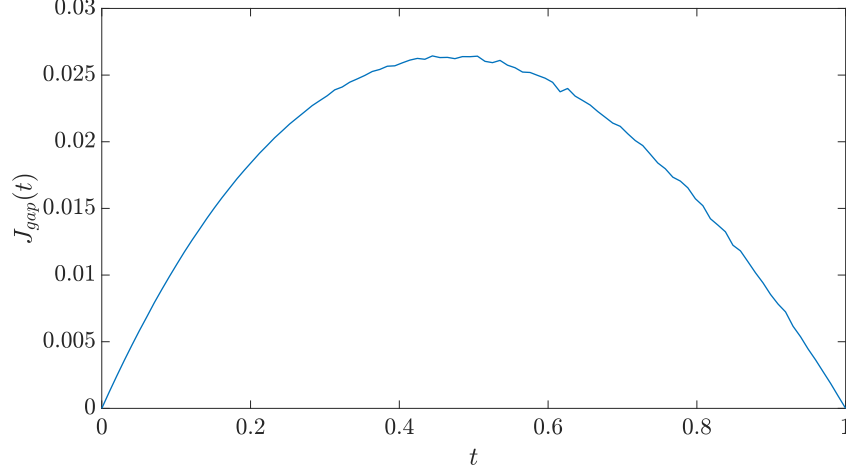
for every  $1 \leq i, j \leq nm, i \neq j$  and  $\alpha > 0$ . Accordingly, the off-diagonal entries of  $\mathbf{C}$  approach zero as  $m \rightarrow \infty$ .

The proof appears in proof 13.

Given the closed-form expression for the matrix  $\overline{\mathbf{C}}$ , deriving a closed-form expression for  $\overline{\mathbf{C}}_s$  is straight-forward since:  $\overline{\mathbf{C}}_s \triangleq \mathbf{S}^{-\frac{1}{2}} \overline{\mathbf{C}} \mathbf{S}^{-\frac{1}{2}}$ . Specifically, the diagonal entries of  $\overline{\mathbf{C}}_s$  are given by:

$$\bar{c}_s(r) = \frac{\bar{c}(r)}{\mu_{xy}} = \begin{cases} 1, & y(r) = 1 \\ 1 - \frac{\cos\left(\frac{2\pi(y(r)-1)}{m}\right)}{2 + \cos\left(\frac{2\pi(x(r)-1)}{n}\right) + \cos\left(\frac{2\pi(y(r)-1)}{m}\right)}, & y(r) > 1 \end{cases} \quad (30)$$

Recall that the common eigenvectors with indices  $r = 1, m+1, 2m+1, \dots$  satisfy  $y(r) = 1$ . By eq. (30), these eigenvectors are preserved, whereas the non-common eigenvectors with indices  $r$  such that  $y(r) \neq 1$  vary. Particularly,

Figure 26: Empirically computed normalized Jensen gap for  $n = 11, m = 31$ .

non-common eigenvectors with indices  $r$  such that  $y(r) < \lfloor \frac{m}{4} \rfloor$  and  $y(r) > \lfloor \frac{3m}{4} \rfloor$  are suppressed, whereas the rest  $\lfloor \frac{m}{4} \rfloor < y(r) < \lfloor \frac{3m}{4} \rfloor$  are enhanced.

In order to derive a closed-form expression for  $\bar{\gamma}(t)$  based on the above derivation, we assume that

$$\bar{\mathbf{C}}_s^t \approx \frac{1}{m!} \sum_{\pi} \mathbf{C}_s^t \quad (31)$$

The accuracy of the approximation is known as the Jensen gap [46, 47]. We define the normalized Jensen gap as follows:

$$J_{gap}(t) = \frac{\|\bar{\mathbf{C}}_s^t - \frac{1}{m!} \sum_{\pi} \mathbf{C}_s^t\|_F^2}{\|\bar{\mathbf{C}}_s^t\|_F^2}$$

At the boundaries  $t = 0$  and  $t = 1$ , we have that  $J_{gap}(0) = J_{gap}(1) = 0$ . Empirically, we report that the values for  $0 < t < 1$  are negligible. For example, in fig. 26, we plot  $J_{gap}(t)$  obtained for the realization considered above, with parameters  $n = 11, m = 31$ . We observe that the Jensen gap is indeed small.

Using the approximation eq. (31) in proposition 6, we obtain

$$\bar{\gamma}(t) \approx \mathbf{V} \mathbf{S}^{\frac{1}{2}} \bar{\mathbf{C}}_s^t \mathbf{S}^{\frac{1}{2}} \mathbf{V}^T$$

Since the matrix  $\bar{\mathbf{C}}_s$  is a diagonal matrix whose entries are given by eq. (30), the eigenvalues of  $\bar{\gamma}(t)$  are the diagonal elements of  $\bar{\mathbf{F}}_t \triangleq \mathbf{S}^{\frac{1}{2}} \bar{\mathbf{C}}_s^t \mathbf{S}^{\frac{1}{2}}$ , explicitly given by:

$$\bar{\mathbf{F}}_t(r, r) = \left( \bar{c}(r) \right)^t \left( \mu_{xy}^{(x(r), y(r))} \right)^{1-t}.$$

By eq. (30), we obtain that if  $y(r) = 1$ , namely, the  $r$ th eigenvalue of  $\bar{\gamma}(t)$  corresponds to a common eigenvector, it equals  $\mu_{xy}^{(x(r), 1)}$ . By eq. (24), we have that  $\mu_{xy}^{(x(r), 1)} = \frac{1}{2} \mu_x^{x(r)} + \frac{1}{2}$ , namely, the  $r$ th eigenvalue of  $\bar{\gamma}(t)$  equals an eigenvalue of the common kernel  $\mathbf{K}_x$  up to an affine constant transformation, independent of  $t$ .

In contrast, for  $y(r) > 1$ , the  $r$ th eigenvalue of  $\bar{\gamma}(t)$  is given by a weighted geometric mean between the  $r$ th eigenvalue of the kernel  $\mathbf{K}_{xy}$  and  $\bar{c}(r)$ . As  $t$  increases and approaches 1, the  $r$ th eigenvalue of  $\bar{\gamma}(t)$  approaches  $\bar{c}(r)$ , and thereby, alleviates the dependency on the non-common eigenvectors.

We conclude this section with another result involving the eigenvectors of  $\mathbf{K}_{xy}$  and the eigenvectors of  $\mathbf{K}_{xz}$ .

**Proposition 9** Let  $v_{xy}^{(k,l)}$  be an eigenvector of  $\mathbf{K}_{xy}$ , and let  $v_{xz}^{(k',l')}$  be an eigenvector of  $\mathbf{K}_{xz}$ . Assume that the permutation  $\pi$  is drawn uniformly at random from the set of all possible permutations of  $m$  elements. If  $k \neq k'$ , then  $\langle v_{xy}^{(k,l)}, v_{xz}^{(k',l')} \rangle = 0$ . If  $k = k'$  and  $l = l' = 1$ , then  $\langle v_{xy}^{(k,l)}, v_{xz}^{(k',l')} \rangle = 1$ . If  $k = k'$  and  $l, l' \neq 1$ , then

$$P(|\langle v_{xy}^{(k,l)}, v_{xz}^{(k',l')} \rangle| \geq \alpha) \leq \frac{1}{\alpha} \sqrt{\frac{2}{m}}$$

In other words, the probability that the absolute value of the inner product  $\langle v_{xy}^{(k,l)}, v_{xz}^{(k',l')} \rangle$  between non-trivial eigenvectors that correspond to the same common component is greater than  $\alpha$  becomes smaller as the size of the non-common graph increases. In addition, in the proof of this result, we observe that the assumption that  $\pi$  is fixed and does not depend on  $x$  actually makes the problem at hand more challenging. If  $\pi$  is not fixed and randomly drawn for any  $x$ , then there exists a larger number of possible permutations, making the Chebyshev inequality used in the proof tighter.

### B.1 Proofs

In this subsection, we present the proofs of the propositions above. We start with several lemmas that will be used in the subsequent proofs of the propositions.

**Lemma 2** *Let  $v \in \mathbb{R}^m$  and let  $\pi$  be a permutation drawn uniformly at random from all possible permutations of  $M$  elements. Define the vector*

$$\bar{v}(y) = \frac{1}{m!} \sum_{\pi} v(\pi(y)).$$

*for  $y = 1, \dots, m$ . We have that  $\bar{v}$  is a constant vector, whose entries are given by*

$$\bar{v}(y) = \frac{1}{m} \sum_{y'=1}^m v(y')$$

*for any  $1 \leq y \leq m$ , independently of  $y$ .*

**Proof 3** *Fix  $y \in \{1, \dots, m\}$ . For each  $y' \in \{1, \dots, m\}$  there exist  $(m-1)!$  possible permutations for which  $\pi(y) = y'$ . Therefore, we have*

$$\bar{v}(y) = \frac{1}{m!} \sum_{\pi} v(\pi(y)) = \frac{1}{m} \sum_{y'=1}^m v(y')$$

**Lemma 3** *Let  $v \in \mathbb{R}^m$  be a non-trivial eigenvector of a diffusion kernel  $\mathbf{K}$  and let  $\pi$  be a permutation drawn uniformly at random from all possible permutations of  $m$  elements. Define*

$$c(y, y') = \frac{1}{m!} \sum_{\pi} v(\pi(y)) v(\pi(y'))$$

*for any  $1 \leq y, y' \leq m$ .*

*Then  $c(y, y')$  is given by:*

$$c(y, y') = -\frac{1}{m(m-1)} + \frac{1}{m-1} \delta(y, y')$$

*where  $\delta(y, y')$  is the Kronecker delta function defined by*

$$\delta(y, y') = \begin{cases} 1 & y = y' \\ 0 & y \neq y' \end{cases}$$

**Proof 4** *Fix  $y \neq y'$ . There exist  $(m-2)!$  possible permutations for which  $\pi(y) = s$  and  $\pi(y') = s'$ . Therefore, we have*

$$\begin{aligned} c(y, y') &= \frac{1}{m!} \sum_{\pi} v(\pi(y)) v(\pi(y')) \\ &= \frac{1}{m!} (m-2)! \sum_{s=1}^m \sum_{s'=1, s' \neq s}^m v(s) v(s') \\ &= \frac{1}{m(m-1)} \sum_{s=1}^m \sum_{s'=1, s' \neq s}^m v(s) v(s') \\ &= -\frac{1}{m(m-1)} \sum_{s=1}^m v^2(s) = -\frac{1}{m(m-1)} \end{aligned}$$

Fix  $y = y'$ . There exist  $(m-1)!$  possible permutations for which  $\pi(y) = \pi(y') = s$ . Therefore, we have

$$\begin{aligned} c(y, y') &= E_\pi [v^2(\pi(y))] \\ &= \frac{1}{m} \sum_{s=1}^m v^2(s) = \frac{1}{m} \end{aligned}$$

Merging these two expressions yields the desired statement:

$$\begin{aligned} c(y, y') &= \frac{1}{m} \delta(y, y') - \frac{1}{m(m-1)} (1 - \delta(y, y')) \\ &= -\frac{1}{m(m-1)} + \frac{1}{m-1} \delta(y, y') \end{aligned}$$

**Lemma 4** Let  $v \in \mathbb{R}^m$  be a non-trivial eigenvector of a diffusion kernel  $\mathbf{K}$ , and let  $\pi$  be a permutation drawn uniformly at random from all possible permutations of  $M$  elements. Define

$$d(y, y') = \frac{1}{m!} \sum_{\pi} [v(\pi^{-1}(\pi(y) \oplus 1)) v(\pi^{-1}(\pi(y') \ominus 1))]$$

for any  $1 \leq y, y' \leq m$ , where  $x \oplus y \triangleq \text{mod}(x + y, m)$  and  $x \ominus y \triangleq \text{mod}(x - y, m)$ . Then  $d(y, y')$  is given by:

$$d(y, y') = \frac{1}{(m-1)(m-2)} \left( v^2(y) + v^2(y') + mv(y)v(y') + \delta(y, y') (1 + mv^2(y)) \right)$$

where  $\delta(y, y')$  is the Kronecker delta function defined in lemma 3.

**Proof 5** Similarly as we did in the proof of lemma 3, also here we recast the expression:

$$\begin{aligned} d(y, y') &= \frac{1}{m!} \sum_{\pi} v(\pi^{-1}(\pi(y) \oplus 1)) v(\pi^{-1}(\pi(y') \ominus 1)) \\ &= \frac{1}{m!} \sum_{s=1}^m \sum_{s'=1}^m N(s, s') v(s) v(s') \end{aligned} \tag{32}$$

where  $N(s, s')$  denotes the number of permutations for which  $s = \pi^{-1}(\pi(y) \oplus 1)$  and  $s' = \pi^{-1}(\pi(y') \ominus 1)$ . We notice that  $\pi(s) = \pi(y) \oplus 1$ , hence  $N(y, s') = 0$  for any  $s' = 1, \dots, m$ . Similarly:  $\pi(s') = \pi(y') \ominus 1$ , hence  $N(s, y') = 0$  for any  $s = 1, \dots, m$ .

Fix  $y = y'$ . Since that  $\pi(s) \neq \pi(s')$  we get that  $s \neq s'$ . As a consequence, the available number of permutations mapping  $(y, y')$  to  $(s, s')$  is:  $m^2 - m - 2(m-1) = (m-1)(m-2)$ , hence:

$$N(s, s') = \begin{cases} 0, & s = y, 1 \leq s' \leq m \\ 0, & 1 \leq s \leq m, s' = y' \\ 0, & s = s' \\ C, & \text{otherwise} \end{cases}$$

where the constant  $C$  is given by dividing the total number of permutations  $m!$  by the total number of non-zeros entries  $(m-1)(m-2)$ :

$$C = \frac{m!}{(m-1)(m-2)} = (m-3)!m$$

Plugging  $N(s, s')$  into eq. (32), we get the following:

$$\begin{aligned} d(y, y') &= \frac{1}{m!} \sum_{s=1}^m \sum_{s'=1}^m N(s, s') v(s) v(s') \\ &= \frac{1}{m!} m(m-3)! \left( \sum_{s=1}^m \sum_{s'=1}^m v(s) v(s') - 2 \sum_{s=1}^m v^2(s) - 2 \sum_{s=1}^m v(s) + 2v(y) \right) \\ &= \frac{1}{m} (2v^2(y) - 1) \end{aligned}$$

Fix  $y \neq y'$ . First we show that there exists no permutation for which  $s = y'$  and  $s' \neq y$ . We prove by contradiction. Assume that  $s = y'$ , recall that  $s = \pi^{-1}(\pi(y) \oplus 1)$ , hence:  $\pi(y') = \pi(y) \oplus 1$ . In additions, recall that:  $s' = \pi^{-1}(\pi(y') \ominus 1)$ , hence  $\pi(s') = (\pi(y') \ominus 1)$ . Substituting  $\pi(y')$  in the previous expression yields:

$$\pi(s') = \pi(y) \oplus 1 \ominus 1 = \pi(y)$$

contradicting that  $s' \neq y$ .

Consider now a permutation that satisfy  $s = y'$ . Such a permutation also satisfies:  $\pi(y) \oplus 1 = \pi(y')$ , hence there exist  $(m-2)m!$  such permutations.

In this case, we get:

$$N(s, s') = \begin{cases} 0, & s = y, 1 \leq s' \leq m \\ 0, & 1 \leq s \leq m, s' = y' \\ 0, & s = y', 1 \leq s' \leq m, s' \neq y \\ 0, & s' = y, 1 \leq s \leq m, s \neq y' \\ (m-2)m!, & s = y', s' = y \\ C', & \text{otherwise} \end{cases}$$

where the constant  $C'$  is given by dividing the remaining number of permutations  $m! - (m-2)m!$  by the number of non-zeros entries  $(m-2)^2$ :

$$C' = \frac{m! - (m-2)m!}{(m-2)^2} = (m-3)m!$$

Plugging  $N(s, s')$  into eq. (32) yields:

$$\begin{aligned} d(y, y') &= \frac{1}{m!} \sum_{s=1}^m \sum_{s'=1}^m N(s, s') v(s) v(s') \\ &= \frac{m(m-3)!}{m!} \left( \sum_{s=1}^m \sum_{s'=1}^m v(s) v(s') - 2v(y) \sum_{s=1}^m v(s) - 2v(y') \sum_{s=1}^m v(s) + 4v(y) v(y') \right) \\ &\quad + \frac{m(m-2)! - m(m-3)!}{m!} v(y) v(y') \\ &= \frac{m+2}{(m-1)(m-2)} v(y) v(y') \end{aligned}$$

To summarize, for any  $y$  and  $y'$ , we have:

$$d(y, y') = \frac{1}{(m-1)(m-2)} \left( v^2(y) + v^2(y') + mv(y)v(y') + \delta(y, y') (1 + mv^2(y)) \right)$$

**Lemma 5** Let  $v \in \mathbb{R}^m$  be a non-trivial eigenvector of a diffusion kernel  $\mathbf{K}$ . Then:

$$\sum_{m=1}^M v(m) = 0$$

**Proof 6** The diffusion kernel  $\mathbf{K}$  is doubly-stochastic, hence - the trivial (constant) vector, denoted by  $v^1$  is an eigenvector of  $\mathbf{K}$ :

$$v^1(m) = \frac{1}{\sqrt{m}}$$

The elements sum of a vector can be recast as the inner-product with the trivial vector:

$$\sum_{m=1}^M v(m) = \sqrt{m} \sum_{m=1}^M v(m) v^1(m) = \sqrt{m} \langle v, v^1 \rangle$$

Due to orthogonality of the eigenvectors  $\langle v, v^1 \rangle = 0$  for every  $v \in \mathbb{R}^m$  which is a non-trivial eigenvector of a diffusion kernel  $\mathbf{K}$ .

**Lemma 6** Let  $v \in \mathbb{R}^m$  be a non-trivial eigenvector of a diffusion kernel  $\mathbf{K}$ , and let  $\pi$  be a permutation drawn uniformly at random from all possible permutations of  $m$  elements. Let  $u = \mathbf{P}_\pi v$  be a permutation of the eigenvector of  $\mathbf{K}$ , where  $\mathbf{P}_\pi$  is the permutation matrix of  $\pi$ . We have

$$\Pr(|\langle u, v \rangle| \geq \alpha) \leq \frac{1}{\alpha} \sqrt{\frac{2}{m}}$$

for any  $0 < \alpha < 1$ . In particular, this inner product approaches zero as  $m$  increases.

**Proof 7** Compute the mean of the inner product, given by

$$\frac{1}{m!} \sum_{\pi} \langle u, v \rangle = \frac{1}{m!} \sum_{\pi} \sum_{y=1}^m v(y) v(\pi(y)) = \sum_{y=1}^m v(y) \left[ \frac{1}{m!} \sum_{\pi} v(\pi(y)) \right]$$

By applying lemma 2, we have

$$\frac{1}{m!} \sum_{\pi} \langle u, v \rangle = \sum_{y=1}^m v(y) \bar{v}(y) = 0$$

since  $\bar{v}$  is a constant vector and sum of elements of  $v$  is zero by lemma 5.

Similarly, compute variance of the inner product:

$$\begin{aligned} \frac{1}{m!} \sum_{\pi} (\langle u, v \rangle)^2 &= \frac{1}{m!} \sum_{\pi} \sum_{y, y'=1}^m v(y) v(y') v(\pi(y)) v(\pi(y')) \\ &= \sum_{y, y'=1}^m v(y) v(y') \left[ \frac{1}{m!} \sum_{\pi} v(\pi(y)) v(\pi(y')) \right] \\ &= \sum_{y, y'=1}^m v(y) v(y') c(y, y') \end{aligned}$$

From lemma 3, we have

$$\frac{1}{m!} \sum_{\pi} (\langle u, v \rangle)^2 = -\frac{1}{m(m-1)} \sum_{y, y'=1}^m v(y) v(y') - \frac{1}{m-1} \sum_{y=1}^m v^2(y)$$

By lemma 5,  $\sum_{y=1}^m v(y) = 0$ , and since the norm of the eigenvector is 1, we have

$$\frac{1}{m!} \sum_{\pi} (\langle u, v \rangle)^2 = \frac{1}{(m-1)}$$

Based on the mean and variance, applying Chebyshev's inequality yields that:

$$P(|\langle u, v \rangle| \geq \alpha) \leq \frac{1}{\alpha} \sqrt{\frac{1}{m-1}}$$

**Proof 8 (Proof of lemma 1)** The Laplacian matrix of a graph  $G$  with affinity matrix  $\mathbf{A}$  is defined by:  $\mathbf{L} = \mathbf{D} - \mathbf{A}$ , where  $\mathbf{D}$  is the degree matrix. We denote the Laplacian matrices of the product graphs by  $\mathbf{L}_{xy}$  and  $\mathbf{L}_{xz}$ . Theorem 4.4.5 in [48] links between the spectral components of  $\mathbf{L}_{xy}$  and the spectral components of  $\mathbf{L}_x$  and  $\mathbf{L}_y$ . Concretely, it entails that the eigenvectors of  $\mathbf{L}_{xy}$  are given by the Cartesian product of the eigenvectors of  $\mathbf{L}_x$  and  $\mathbf{L}_y$ , i.e.:

$$\phi_{xy}^{(k,l)}(t) = \phi_x^k(x(t)) \phi_y^l(y(t)) \quad (33)$$

where  $\phi_{xy}^{(k,l)} \in \mathbb{R}^{mn}$  is an eigenvector of  $\mathbf{L}_{xy}$ ,  $\phi_x^k \in \mathbb{R}^n$  is the  $k$ th eigenvector of  $\mathbf{L}_x$  and  $\phi_y^l \in \mathbb{R}^m$  is the  $l$ th eigenvector of  $\mathbf{L}_y$ . In addition, the eigenvalues of  $\mathbf{L}_{xy}$  are given by the sum of the eigenvalues of  $\mathbf{L}_x$  and  $\mathbf{L}_y$ , i.e.:

$$\xi_{xy}^{(k,l)} = \xi_x^k + \xi_y^l \quad (34)$$

where  $\xi_{xy}^{(k,l)}$  is the eigenvalue corresponding to  $\phi_{xy}^{(k,l)}$ ,  $\xi_x^k$  is the eigenvalue corresponding to  $\phi_x^k$ , and  $\xi_y^l$  is the eigenvalue corresponding to  $\phi_y^l$ . We now link the spectral components of a diffusion kernel  $\mathbf{K}_x$  and the spectral components of the Laplacian  $\mathbf{L}_x$  (and similarly  $\mathbf{K}_y$  and  $\mathbf{L}_y$ ).



For  $d$ -regular graphs:  $\mathbf{L}_x = d(\mathbf{I} - \mathbf{K}_x)$ , specifically for the cycle graphs we consider  $d = 2$ . Hence each eigenvector of  $\mathbf{L}_x$  is also an eigenvector of  $\mathbf{K}_x$ . More concretely, the eigenvalues of  $\mathbf{K}_x$  are given by the following mapping:

$$\mu_x = 1 - \frac{1}{d}\xi_x$$

where  $\mu_x$  is the eigenvalue of  $\mathbf{K}$  corresponding to the eigenvalue of  $\mathbf{L}$ ,  $\xi_x$ . Specifically, in our case:

$$\mu_x^k = 1 - \frac{1}{d}\xi_x^k \quad v_x^k = \phi_x^k \quad (35)$$

$$\mu_y^l = 1 - \frac{1}{d}\xi_y^l \quad v_y^l = \phi_y^l \quad (36)$$

where  $\{(\xi_x^k, \phi_x^k)\}_{k=1}^n$  is the set of eigenvalues and eigenvectors of  $\mathbf{L}_x$  and  $\{(\xi_y^l, \phi_y^l)\}_{l=1}^m$  is the set of eigenvalues and eigenvectors of  $\mathbf{L}_y$ . According to theorem 4.4.5 in [48], the spectral components of  $\mathbf{L}_{xy}$  are given by:

$$\phi_{xy}^{(k,l)}(t) = \phi_x^k(x(t)) \phi_y^l(y(t)) \quad \xi_{xy}^{(k,l)} = \xi_x^k + \xi_y^l$$

The Cartesian product of two  $d$ -regular graphs is a  $2d$ -regular graph. Therefore  $G_{xy}$  is  $2d$ -regular graph and the spectral components of  $\mathbf{K}_{xy}$  are given by:

$$\mu_{xy}^{(k,l)} = 1 - \frac{1}{2d}\xi_{xy}^{(k,l)} \quad v_{x,y}^{(k,l)} = \phi_{x,y}^{(k,l)} \quad (37)$$

Substituting eq. (33) and eq. (34) in eq. (37) we get:

$$\mu_{xy}^{(k,l)} = 1 - \frac{1}{2d}(\xi_x^k + \xi_y^l) \quad v_{x,y}^{(k,l)} = \phi_x^k(x(t)) \phi_y^l(y(t)) \quad (38)$$

Then, substituting eq. (35) in eq. (38), we get:

$$\mu_{xy}^{(k,l)} = \frac{1}{2}(\mu_x^k + \mu_y^l) \quad v_{x,y}^{(k,l)} = v_x^k(x(t)) v_y^l(y(t))$$

**Lemma 7** The matrix  $\mathbf{C}$  is block-diagonal and can be recast as:

$$\mathbf{C} = \mathbf{V}\mathbf{R}\mathbf{V}^T$$

where  $\mathbf{R}$  is a block diagonal matrix of  $n$  blocks, whose  $k$ th block is given by:

$$\mathbf{r}^k(s, s') = \frac{1}{4} \cos\left(\frac{2\pi(k-1)}{n}\right) \delta(s, s') + \frac{1}{4} \sqrt{\frac{m}{2}} \mathbf{r}_\pi(s, s')$$

the matrix  $\mathbf{r}_\pi(s, s')$  depends on the permutation  $\pi$  and is given by:

$$\mathbf{r}_\pi(s, s') = \frac{1}{\sqrt{2m}} \left( \beta^m(\pi(s)) \delta(\pi(s) \oplus 1, \pi(s')) + \beta^2(\pi(s)) \delta(\pi(s) \ominus 1, \pi(s')) \right)$$

and  $\beta^x(s)$  is defined as follows:

$$\beta^x(s) \triangleq \begin{cases} \frac{1}{\sqrt{2}}, & s = 1 \\ \sqrt{2}, & s = x \\ 1, & \text{otherwise} \end{cases}$$

**Proof 9** We denote the blocks of  $\mathbf{B}$  by  $\mathbf{b}$ , such that:  $\mathbf{B} = \mathbf{I}_n \otimes \mathbf{b}$  where  $\otimes$  is the matrix Kronecker product and  $\mathbf{I}_n$  is an  $n \times n$  identity matrix. The matrix  $\mathbf{b}$  is explicitly given by:

$$\mathbf{b}_{i,j} = \begin{cases} 1, & i = j = 1 \\ 0, & (i = 1 \wedge j > 1) \vee (j = 1 \wedge i > 1) \\ \sum_{s=1}^m v_y^i(s) v_y^j(\pi(s)), & 1 < i, j \leq m \end{cases} \quad (39)$$

Since  $\mathbf{B}$  is block diagonal,  $\mathbf{C}$  is block diagonal as well. We denote the  $k$ th block of  $\mathbf{C}$  by  $\mathbf{c}^k \in \mathbb{R}^{m \times m}$ . The entries of  $\mathbf{c}^k$  are given by:

$$\mathbf{c}_{i,j}^k = \sum_{u=1}^m \mu_{xy}^{(k,u)} \mathbf{b}_{i,u} \mathbf{b}_{j,u} \quad (40)$$

where  $\mu_{xy}^{(k,u)}$  are give by lemma 1:

$$\mu_{xy}^{(k,u)} = \frac{1}{2} (\mu_x^k + \mu_y^u)$$

For any  $1 < i \leq m$ , we have

$$\mathbf{c}_{1,i}^k = 0$$

$$\mathbf{c}_{i,1}^k = 0$$

For  $i, j \neq 1$ , substituting eq. (39) into eq. (40) yields:

$$\begin{aligned} \mathbf{c}_{i,j}^k &= \sum_{u=1}^m \mu_{xy}^{(k,u)} \mathbf{b}_{i,u} \mathbf{b}_{j,u} \\ &= \sum_{u=1}^m \mu_{xy}^{(k,u)} \sum_{s=1}^m v_y^i(s) v_y^u(\pi(s)) \sum_{s'=1}^m v_y^j(s') v_y^u(\pi(s')) \\ &= \sum_{s=1}^m v_y^i(s) \sum_{s'=1}^m v_y^j(s') \sum_{u=1}^m \mu_{xy}^{(k,u)} v_y^u(\pi(s)) v_y^u(\pi(s')) \\ &= \sum_{s=1}^m v_y^i(s) \sum_{s'=1}^m v_y^j(s') \mathbf{r}^k(s, s') \end{aligned}$$

where:

$$\mathbf{r}^k(s, s') \triangleq \sum_{u=1}^m s_{xy}^{(k,u)} v_y^u(\pi(s)) v_y^u(\pi(s'))$$

Note that defining  $\mathbf{R}$  to be a block diagonal matrix whose  $k$ th block is  $\mathbf{r}^k$  yields:

$$\mathbf{C} = \mathbf{V} \mathbf{R} \mathbf{V}^T$$

Next we derive the explicit expression of  $\mathbf{r}^k$ . The eigenvalue  $\mu_{xy}^{(k,u)}$  is given by:

$$\mu_{xy}^{(k,u)} = \frac{1}{2} + \frac{1}{4} \cos\left(\frac{2\pi(k-1)}{n}\right) + \frac{1}{4} \sqrt{\frac{m}{2}} v_y^2(u)$$

Then, we substitute this expression into the definition of  $\mathbf{r}^k(s, s')$  and get:

$$\mathbf{r}^k(s, s') = \left(\frac{1}{2} + \frac{1}{4} \cos\left(\frac{2\pi(k-1)}{n}\right)\right) \sum_{u=1}^m v_y^u(\pi(s)) v_y^u(\pi(s')) + \frac{1}{4} \sqrt{\frac{m}{2}} \sum_{u=1}^m v_y^2(u) v_y^u(\pi(s)) v_y^u(\pi(s')) \quad (41)$$

$$= \left(\frac{1}{2} + \frac{1}{4} \cos\left(\frac{2\pi(k-1)}{n}\right)\right) \mathbf{r}_d(s, s') + \frac{1}{4} \sqrt{\frac{m}{2}} \mathbf{r}_\pi(s, s') \quad (42)$$

where

$$\mathbf{r}_d(s, s') \triangleq \sum_{u=1}^m v_y^u(\pi(s)) v_y^u(\pi(s')) \quad (43)$$

and

$$\mathbf{r}_\pi(s, s') \triangleq \sum_{u=1}^m v_y^2(u) v_y^u(\pi(s)) v_y^u(\pi(s')) \quad (44)$$

We note that the matrix  $\mathbf{r}_d(s, s')$  actually equals the eye matrix:

$$\mathbf{r}_d(s, s') = \sum_{u=1}^m v_y^u(\pi(s)) v_y^u(\pi(s')) = \sum_{u=1}^m v_y^{\pi(s)}(u) v_y^{\pi(s')}(u) = \delta(\pi(s), \pi(s')) = \delta(s, s') \quad (45)$$

In order to derive a simplified expression for  $\mathbf{r}_\pi(s, s')$  we first derive a simplified expression for the elements consisting the sum in  $\mathbf{r}_\pi(s, s')$ :

$$\begin{aligned} v_y^2(u) v_y^u(\pi(s)) v_y^u(\pi(s')) &= \sqrt{\frac{2}{m}} \cos\left(\frac{2\pi(u-1)}{m}\right) \frac{\alpha(\pi(s))}{\sqrt{m}} \cos\left(\frac{2\pi(\pi(s)-1)}{m}\right) \\ &= \frac{\sqrt{2}\alpha(\pi(s))}{2m} \left( \cos\left(\frac{2\pi(\pi(s))}{m}(u-1)\right) + \cos\left(\frac{2\pi(\pi(s)-2)}{m}(u-1)\right) \right) \\ &= \frac{\alpha(\pi(s))}{\sqrt{2m}} \left( \frac{1}{\alpha(\pi(s) \oplus 1)} v_y^{\pi(s) \oplus 1}(u) + \frac{1}{\alpha(\pi(s) \ominus 1)} v_y^{\pi(s) \ominus 1}(u) \right) \end{aligned}$$

where  $\alpha(r)$  is defined in eq. (25), and:

$$\begin{aligned} x \oplus y &\triangleq \text{mod}(x + y, m) \\ x \ominus y &\triangleq \text{mod}(x - y, m) \end{aligned}$$

Then, we substitute these expression in eq. (44), and compute a simplified expression for  $\mathbf{r}_\pi$ :

$$\begin{aligned} \mathbf{r}_\pi(s, s') &= \sum_{u=1}^m v_y^2(u) v_y^{\pi(s)}(u) v_y^{\pi(s')}(u) \\ &= \frac{\alpha(\pi(s))}{\sqrt{2m}} \sum_{u=1}^m v_y^{\pi(s')}(u) \left( \frac{1}{\alpha(\pi(s) \oplus 1)} v_y^{\pi(s) \oplus 1}(u) + \frac{1}{\alpha(\pi(s) \ominus 1)} v_y^{\pi(s) \ominus 1}(u) \right) \\ &= \frac{\alpha(\pi(s))}{\sqrt{2m}} \left( \frac{\delta(\pi(s) \oplus 1, \pi(s'))}{\alpha(\pi(s) \oplus 1)} + \frac{\delta(\pi(s) \ominus 1, \pi(s'))}{\alpha(\pi(s) \ominus 1)} \right) \\ &= \frac{1}{\sqrt{2m}} \left( \beta^m(\pi(s)) \delta(\pi(s) \oplus 1, \pi(s')) + \beta^2(\pi(s)) \delta(\pi(s) \ominus 1, \pi(s')) \right) \end{aligned}$$

where

$$\beta^x(s) = \begin{cases} \frac{1}{\sqrt{2}}, & s = 1 \\ \sqrt{2}, & s = x \\ 1, & \text{otherwise} \end{cases}$$

Substituting this explicit form of  $\mathbf{r}_\pi(s, s')$  into  $\mathbf{r}^k(s, s')$  gives:

$$\begin{aligned} \mathbf{r}^k(s, s') &= \left( \frac{1}{2} + \frac{1}{4} \cos\left(\frac{2\pi(k-1)}{n}\right) \right) \delta(s, s') + \\ &\quad \frac{1}{8} \left( \beta^m(\pi(s)) \delta(\pi(s) \oplus 1, \pi(s')) + \beta^2(\pi(s)) \delta(\pi(s) \ominus 1, \pi(s')) \right) \end{aligned}$$

**Proof 10 (Proof for proposition 5)** Recalling that the matrix  $\mathbf{B}$  is defined as the pairwise inner products between the eigenvectors of  $\mathbf{K}_{xy}$  and the eigenvectors of  $\mathbf{K}_{xz}$ , we can write each entry as follows:

$$\mathbf{B}_{i,j} = \langle v_{xy}^{(x(i), y(i))}, v_{xz}^{(x(j), y(j))} \rangle$$

By eq. (24), for  $1 \leq r \leq mn$ , we have:

$$\begin{aligned} v_{xy}^{(x(i), y(i))}(r) &= v_x^{x(i)}(x(r)) v_y^{y(i)}(y(r)) \\ v_{xz}^{(x(j), z(j))}(r) &= v_x^{x(j)}(x(r)) v_z^{z(j)}(z(r)) = v_x^{x(j)}(x(r)) v_y^{y(j)}(\pi(y(r))) \end{aligned}$$

Then, we compute:

$$\begin{aligned}
\langle v_{xy}^{(x(i),y(i))}, v_{xz}^{(x(j),y(j))} \rangle &= \sum_{r=1}^{mn} v_{xy}^{(x(i),y(i))}(r) v_{xz}^{(x(j),y(j))}(r) = \\
&= \sum_{r=1}^{mn} v_x^{x(i)}(x(r)) v_y^{y(i)}(y(r)) v_x^{x(j)}(x(r)) v_y^{y(j)}(\pi(y(r))) = \\
&= \sum_{y=1}^m \sum_{x=1}^n v_x^{x(i)}(x) v_y^{y(i)}(y) v_x^{x(j)}(x) v_y^{y(j)}(\pi(y)) = \\
&= \sum_{x=1}^n v_x^{x(i)}(x) v_x^{x(j)}(x) \sum_{y=1}^m v_y^{y(i)}(y) v_y^{y(j)}(\pi(y)) = \\
&= \delta(x(i), x(j)) \sum_{y=1}^m v_y^{y(i)}(y) v_y^{y(j)}(\pi(y))
\end{aligned}$$

where the last transition is due to the orthogonality of the eigenvectors of  $\mathbf{K}_x$ . Recall that  $x(r) = 1 + \lfloor \frac{r}{m} \rfloor$ , hence,  $\mathbf{B}$  can be recast as:

$$\mathbf{B} = \mathbf{1}_n \otimes \mathbf{b}$$

where  $\otimes$  is the matrix Kronecker product,  $\mathbf{I}_n$  is the  $n \times n$  identity matrix, and  $\mathbf{b} \in \mathbf{R}^{m \times m}$  is given by:

$$\mathbf{b}_{l,l'} = \sum_{y=1}^m v_y^l(y) v_y^{l'}(\pi(y))$$

Since  $v^1$  is the trivial (constant) eigenvector with norm 1, we get that  $\mathbf{b}_{1,l'} = 1$ . If  $l = 1$  and  $l' \neq 1$ , we have  $\mathbf{b}_{1,l'} = 0$  due to lemma 2. If  $l' = 1$  and  $l \neq 1$ , we have  $\mathbf{b}_{l,1} = 0$  due to the orthogonality of the eigenvectors. If  $l, l' \neq 1$ , by lemma 6, we have:

$$P(|\mathbf{b}_{l,l'}| \geq \alpha) = P\left(\sum_{y=1}^m v_y^l(y) v_y^{l'}(\pi(y)) \geq \alpha\right) \leq \frac{1}{\alpha} \sqrt{\frac{1}{m-1}}$$

**Proof 11 (Proof for proposition 6)** The matrix  $\gamma(t)$  on the geodesic path is given by:

$$\gamma(t) = \mathbf{K}^{\frac{1}{2}} \mathbf{M}^t \mathbf{K}^{\frac{1}{2}}$$

where  $\mathbf{M} \triangleq \mathbf{V} \mathbf{C}_S \mathbf{V}^T$ . Since  $\mathbf{V} \mathbf{V}^T = \mathbf{I}$ , the matrix power  $\mathbf{M}^t$  is given by  $\mathbf{M}^t = \mathbf{V} \mathbf{C}_S^t \mathbf{V}^T$ . Using the EVD of  $\mathbf{K}$  yields that  $\gamma(t)$  can be written as:

$$\gamma(t) = \mathbf{K}^{\frac{1}{2}} \mathbf{M}^t \mathbf{K}^{\frac{1}{2}} = \mathbf{V} \mathbf{S}^{\frac{1}{2}} \mathbf{V}^T \mathbf{M}^t \mathbf{V} \mathbf{S}^{\frac{1}{2}} \mathbf{V}^T = \mathbf{V} \mathbf{S}^{\frac{1}{2}} \mathbf{V}^T \mathbf{V} \mathbf{C}_S^t \mathbf{V}^T \mathbf{V} \mathbf{S}^{\frac{1}{2}} \mathbf{V}^T = \mathbf{V} \mathbf{S}^{\frac{1}{2}} \mathbf{C}_S^t \mathbf{S}^{\frac{1}{2}} \mathbf{V}^T$$

**Proof 12 (Proof for proposition 7)** Since  $\mathbf{B}$  is block diagonal also  $\mathbf{C}$  is block diagonal. Similarly as we did in the proof for proposition 8, we denote the  $k$ th block of  $\mathbf{C}$  by  $\mathbf{c}^k \in \mathbf{R}^{m \times m}$ . The entries of  $\mathbf{c}^k$  are given by:

$$\mathbf{c}_{i,j}^k = \sum_{u=1}^m \mu_{xy}^{(k,u)} \mathbf{b}_{i,u} \mathbf{b}_{j,u}$$

where  $\mu_{xy}^{(k,u)}$  can be computed according to lemma 1 and  $\mathbf{b}_{i,j}$  is given by eq. (39). We compute:

$$\mathbf{c}_{1,1}^k = \sum_{u=1}^m \mu_{xy}^{(k,u)} \mathbf{b}_{1,u} \mathbf{b}_{1,u} = \mu_{xy}^{(k,1)} = \frac{3}{4} + \frac{1}{4} \cos\left(\frac{2\pi(k-1)}{n}\right) \quad (46)$$

In order to compute  $\mathbf{c}_{i,j}^k$  for  $i, j > 1$  we utilize the results from lemma 7. According to lemma 7,  $\mathbf{c}_{i,j}^k$  for  $i, j > 1$  is given by:

$$\mathbf{c}_{i,j}^k = \sum_{s=1}^m v_y^i(s) \sum_{s'=1}^m v_y^j(s') \mathbf{r}^k(s, s')$$

Where  $\mathbf{r}^k$  is given by eq. (41). We substitute eq. (41) and eq. (45) in the expression for  $\mathbf{c}_{i,j}^k$  and get the following expression:

$$\mathbf{c}_{i,j}^k = \left( \frac{1}{2} + \frac{1}{4} \cos\left(\frac{2\pi(k-1)}{n}\right) \right) \delta(i, j) + \sum_{s=1}^m v_y^i(s) \sum_{s'=1}^m v_y^j(s') \mathbf{r}_\pi(s, s')$$

We substitute the expression for  $\mathbf{r}_\pi$  from eq. (44) and compute the mean matrix  $\frac{1}{m!} \sum_\pi \mathbf{r}_\pi$ :

$$\begin{aligned} \frac{1}{m!} \sum_\pi \mathbf{r}_\pi &= \frac{1}{m!} \sum_\pi \sum_{u=1}^m v_y^2(u) v_y^u(\pi(s)) v_y^u(\pi(s')) \\ &= \sum_{u=1}^m v_y^2(u) \frac{1}{m!} \sum_\pi v_y^u(\pi(s)) v_y^u(\pi(s')) \\ &= \sum_{u=1}^m v_y^2(u) \left( -\frac{1}{m(m-1)} + \frac{1}{m-1} \delta(s, s') \right) = 0 \end{aligned}$$

Then, we utilize this result in order to calculate the mean expression for  $\mathbf{c}^k$ :

$$\begin{aligned} \frac{1}{m!} \sum_\pi \mathbf{c}_{i,j}^k &= \left( \frac{1}{2} + \frac{1}{4} \cos \left( \frac{2\pi(k-1)}{n} \right) \right) \delta(i, j) + \frac{1}{m!} \sum_\pi \sum_{s=1}^m v_y^i(s) \sum_{s'=1}^m v_y^j(s') \mathbf{r}_\pi(s, s') \\ &= \left( \frac{1}{2} + \frac{1}{4} \cos \left( \frac{2\pi(k-1)}{n} \right) \right) \delta(i, j) + \frac{1}{m!} \sum_{s=1}^m v_y^i(s) \sum_{s'=1}^m v_y^j(s') \sum_\pi \mathbf{r}_\pi(s, s') \\ &= \left( \frac{1}{2} + \frac{1}{4} \cos \left( \frac{2\pi(k-1)}{n} \right) \right) \delta(i, j) \end{aligned}$$

Therefore, the mean matrix  $\frac{1}{m!} \sum_\pi \mathbf{c}^k$  is a diagonal matrix, whose diagonal elements are given by:

$$\bar{c}^k(s) = \frac{1}{2} + \frac{1}{4} \cos \left( \frac{2\pi(k-1)}{n} \right) + \frac{1}{4} \delta(s, 1)$$

where  $1 \leq s \leq m$ . As consequence, the mean matrix  $\frac{1}{m!} \sum_\pi \mathbf{C}$  is a diagonal matrix, whose diagonal elements are given by:

$$\bar{c}(r) = \frac{1}{2} + \frac{1}{4} \cos \left( \frac{2\pi(x(r)-1)}{n} \right) + \frac{1}{4} \delta(y(r), 1)$$

where  $1 \leq r \leq mn$ .

**Proof 13 (Proof for proposition 8)** By lemma 7, for  $i, j > 1$ , we compute:

$$\begin{aligned} \mathbf{c}_{i,j}^k &= \sum_{s=1}^m v_y^i(s) \sum_{s'=1}^m v_y^j(s') \mathbf{r}^k(s, s') \\ &= \left( \frac{1}{2} + \frac{1}{4} \cos \left( \frac{2\pi(k-1)}{n} \right) \right) \delta(i, j) \\ &\quad + \frac{1}{8} \left( \sum_{s=1}^m \beta^m(\pi(s)) v_y^i(s) v_y^j(\pi^{-1}(\pi(s) \oplus 1)) + \sum_{s=1}^m \beta^2(\pi(s)) v_y^i(s) v_y^j(\pi^{-1}(\pi(s) \ominus 1)) \right) \\ &= \left( \frac{1}{2} + \frac{1}{4} \cos \left( \frac{2\pi(k-1)}{n} \right) \right) \delta(i, j) \\ &\quad + \frac{1}{8} \left( \sum_{s=1}^m \beta^m(\pi(s)) v_y^i(s) v_y^j(\pi^{e+}(s)) + \sum_{s=1}^m \beta^2(\pi(s)) v_y^i(s) v_y^j(\pi^{e-}(s)) \right) \end{aligned}$$

where:

$$\begin{aligned} \pi^{e+}(s) &= \pi^{-1}(\pi(s) \oplus 1) \\ \pi^{e-}(s) &= \pi^{-1}(\pi(s) \ominus 1) \end{aligned}$$

Since  $\beta^x(s)$  can be recast as  $\beta^x(s) = 1 + (\sqrt{2} - 1)\delta(s, x) + (\frac{1}{\sqrt{2}} - 1)\delta(s, 1)$ , we have:

$$\begin{aligned} \mathbf{c}_{i,j}^k &= \left( \frac{1}{2} + \frac{1}{4} \cos \left( \frac{2\pi(k-1)}{n} \right) \right) \delta(i, j) \\ &+ \frac{1}{8} \left( \sum_{s=1}^m v_y^i(s) v_y^j(\pi^{e+}(s)) + \sum_{s=1}^m v_y^i(s) v_y^j(\pi^{e-}(s)) \right) \\ &+ \frac{(\sqrt{2}-1)}{8} (v_y^i(m) v_y^j(\pi^{e+}(m)) + v_y^i(m) v_y^j(\pi^{e-}(m))) \\ &+ \frac{(\frac{1}{\sqrt{2}}-1)}{8} (v_y^i(1) v_y^j(\pi^{e+}(1)) + v_y^i(1) v_y^j(\pi^{e-}(1))) \\ &= \left( \frac{1}{2} + \frac{1}{4} \cos \left( \frac{2\pi(k-1)}{n} \right) \right) \delta(i, j) \\ &+ \frac{1}{8} \left( \sum_{s=1}^m v_y^i(s) v_y^j(\pi^{e+}(s)) + \sum_{s=1}^m v_y^i(s) v_y^j(\pi^{e-}(s)) \right) \end{aligned}$$

The off-diagonal entries  $i \neq j$  are given by:

$$\mathbf{c}_{i,j}^k = \frac{1}{8} \left( \sum_{s=1}^m v_y^i(s) v_y^j(\pi^{e+}(s)) + \sum_{s=1}^m v_y^i(s) v_y^j(\pi^{e-}(s)) \right).$$

By lemma 2, the mean of the off-diagonal entries is

$$\frac{1}{m!} \sum_{\pi} \mathbf{c}_{i,j}^k = 0$$

The variance of the off-diagonal entries is:

$$\begin{aligned} \frac{1}{m!} \sum_{\pi} (\mathbf{c}_{i,j}^k)^2 &= \frac{1}{64} \sum_{s=1}^m \sum_{s'=1}^m v_y^i(s) v_y^i(s') \left[ \frac{1}{m!} \sum_{\pi} v_y^j(\pi^{e+}(s)) v_y^j(\pi^{e+}(s')) \right] \\ &+ \frac{1}{64} \sum_{s=1}^m \sum_{s'=1}^m v_y^i(s) v_y^i(s') \left[ \frac{1}{m!} \sum_{\pi} v_y^j(\pi^{e-}(s)) v_y^j(\pi^{e-}(s')) \right] \\ &+ \frac{1}{64} \sum_{s=1}^m \sum_{s'=1}^m v_y^i(s) v_y^i(s') \left[ \frac{1}{m!} \sum_{\pi} v_y^j(\pi^{e+}(s)) v_y^j(\pi^{e-}(s')) \right] \\ &= \frac{2}{64} \sum_{s=1}^m \sum_{s'=1}^m v_y^i(s) v_y^i(s') \left[ \frac{1}{m!} \sum_{\pi} v_y^j(\pi^{e+}(s)) v_y^j(\pi^{e+}(s')) \right] \\ &+ \frac{1}{64} \sum_{s=1}^m \sum_{s'=1}^m v_y^i(s) v_y^i(s') \left[ \frac{1}{m!} \sum_{\pi} v_y^j(\pi^{e+}(s)) v_y^j(\pi^{e-}(s')) \right] \end{aligned}$$

By lemma 3, the first term becomes:

$$\sum_{s=1}^m \sum_{s'=1}^m v_y^i(s) v_y^i(s') \left[ \frac{1}{m!} \sum_{\pi} v_y^j(\pi^{e+}(s)) v_y^j(\pi^{e-}(s')) \right] = \frac{1}{m-1} \sum_{s=1}^m (v_y^i(s))^2 = \frac{1}{m-1}$$

In the second term, we substitute the expression from lemma 4 and get:

$$\begin{aligned}
& \sum_{s=1}^m \sum_{s'=1}^m v_y^i(s) v_y^i(s') \left[ \frac{1}{m!} \sum_{\pi} v_y^j(\pi^{e+}(s)) v_y^j(\pi^{e-}(s')) \right] \\
&= \frac{1}{(m-1)(m-2)} \left[ \sum_{s=1}^m \sum_{s'=1}^m v_y^i(s) v_y^i(s') \left( (v_y^j(s))^2 + (v_y^j(s'))^2 + m v_y^j(s) v_y^j(s') \right) \right. \\
&\quad \left. + \sum_{s=1}^m (v_y^i(s))^2 \left( 1 + m (v_y^j(s))^2 \right) \right] \\
&= \frac{1}{(m-1)(m-2)} + \frac{m}{(m-1)(m-2)} \sum_{s=1}^m (v_y^i(s))^2 (v_y^j(s))^2 \\
&\leq \frac{2}{(m-1)(m-2)}
\end{aligned}$$

Plugging the simplified two terms back into the variance yields:

$$\frac{1}{m!} \sum_{\pi} (\mathbf{c}_{i,j}^k)^2 \leq \frac{2}{64(m-1)} + \frac{2}{64(m-2)(m-1)} = \frac{1}{32(m-1)}$$

Finally, based on the mean and variance, applying Chebyshev's inequality yields that the probability to draw a permutation in which the absolute value of the off-diagonal entries is greater or equal to  $\alpha$  is bounded from above by:

$$P(|\mathbf{c}_{i,j}^k| \geq \alpha) \leq \frac{1}{\alpha} \sqrt{\frac{1}{32(m-1)}}$$

## C Additional simulations and experimental results

In this section we present additional simulations and experimental results. First, we consider a setting with  $\mathcal{M}_x = [-1/2, 1/2]$  and suppose we have samples  $x_i$  from  $\mathcal{M}_x$  drawn uniformly at random.

The measurements are given by:

$$s_i^{(v)} = \ell_x^{(v)} x_i$$

where  $v = 1, 2$  and the scales  $\ell_x^{(v)}$  are set to  $\ell_x^{(1)} = 1$  and  $\ell_x^{(2)} = 5$ . As mentioned in section 5.1, according to [34], the eigenvalues of the continuous diffusion operator defined on each set of measurements are given by:

$$\lambda_v^{k_x} = \left( \frac{k_x \pi}{\ell_x^{(v)}} \right)^2$$

for  $k_x = 0, 1, 2, \dots$ . The eigenvalues of the discrete operator can be derived from the eigenvalues of the continuous operator by:

$$\mu_v^{k_x} = \exp \left( - \frac{(\epsilon^{(v)})^2}{4} \lambda_v^{k_x} \right)$$

where  $\epsilon^{(v)}$  is the scale of the discrete kernel. According to eq. (17) and eq. (19) the eigenvalues of  $\gamma(t)$  and  $\mathbf{L}(t)$  are given by:

$$\mu_{\gamma(t)}^{k_x} = \exp \left( - \left( \frac{\pi}{4\ell^{(\gamma(t))}} \right)^2 k_x^2 \right) \quad (47)$$

$$\mu_{\mathbf{L}(t)}^{k_x} = (1-t) \exp \left( - \left( \frac{\epsilon^{(1)} \pi}{4\ell_x^{(1)}} \right)^2 k_x^2 \right) + t \exp \left( - \left( \frac{\epsilon^{(2)} \pi}{4\ell_x^{(2)}} \right)^2 k_x^2 \right) \quad (48)$$

where  $\ell^{(\gamma(t))}$  is an effective length defined in eq. (18).

We observe in eq. (47) that the eigenvalues of  $\gamma(t)$  coincide with the eigenvalues of the discrete diffusion operator that would have been constructed from uniform samples from a 1D interval  $[0, \ell^{(\gamma(t))}]$ . Conversely, eq. (48) implies



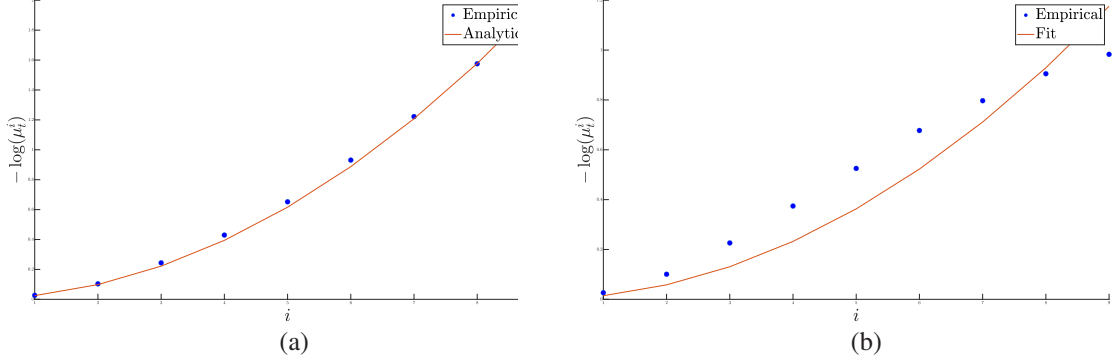


Figure 27: (a) The fit of the eigenvalues of  $\gamma(0.4)$  to the analytic expression. (b) The fit of the eigenvalues of  $\mathbf{L}(0.4)$  to  $\exp(-ck_x^2)$ . The blue dots are the logarithm of the 10 leading eigenvalues, and the red curve is the obtained fit.

that the eigenvalues of  $\mathbf{L}(t)$  cannot be expressed in the form  $\exp(-ck_x^2)$ , where  $k_x$  is the eigenvalue index and  $c$  is a constant.

We demonstrate the above observation in a simulation. We pick two points,  $\gamma(0.4)$  on the geodesic path connecting  $\mathbf{K}_1$  and  $\mathbf{K}_2$ , and  $\mathbf{L}(0.4)$  on the linear path connecting  $\mathbf{K}_1$  and  $\mathbf{K}_2$ . We apply eigenvalue decomposition to  $\gamma(0.4)$  and  $\mathbf{L}(0.4)$ , and depict the logarithm of the obtained eigenvalues in fig. 27. In addition, we depict the analytic expression of the eigenvalues of  $\gamma(0.4)$  given by eq. (17) and the fit of the eigenvalues of  $\mathbf{L}(0.4)$  to the function  $\exp(-ck_x^2)$ , where  $k_x = 1, 2, \dots, 9$ . Indeed, we observe that the eigenvalues of  $\gamma(0.4)$  admit Weyl's law, establishing the correspondence to a diffusion operator of a 1D interval. In contrast, the eigenvalues of  $\mathbf{L}(0.4)$  do not admit such a form. Next, we revisit the setting in section 5.1 and present additional results for different choices of the scale parameters:  $\ell_x^{(1)}$ ,  $\ell_y^{(1)}$ ,  $\ell_x^{(2)}$ , and  $\ell_z^{(2)}$ .

First, we choose the following parameters:

$$\begin{aligned}\ell_x^{(1)} &= 2, \ell_x^{(2)} = 2 \\ \ell_y^{(1)} &= 2, \ell_z^{(2)} = 2\end{aligned}$$

designating the common component to be as dominant as the measurement-specific component in each of the measurements. In other words, the CMR of the two measurements (i.e.  $\text{CMR}(t=0)$  and  $\text{CMR}(t=1)$ ) are the same. We compute the eigenvalues flow diagram using algorithm 1 with  $N_t = 200$  and  $K = 20$ . In addition, we estimate the CMR at each point along the geodesic path using algorithm 4. The eigenvalues flow diagram is depicted in fig. 28, where the point  $t$  along the geodesic path at which the CMR estimate is maximal is marked by a horizontal red line. We observe a symmetric diagram, corresponding to the symmetry of the measurements induced by the choice of scale parameters, where the maximal CMR is obtained at  $t^* = 0.5$ .

fig. 29 is the same as fig. 5, depicting the diffusion patterns at  $t = 0, 0.3, t^*, 1$  obtained in this example. We observe the invariance to the measurement-specific components, conveyed by the saturation along the vertical axes, in the diffusion patterns associated with  $t = 0.3$  and  $t^* = 0.5$ .

Next, we consider another choice of parameters:

$$\begin{aligned}\ell_x^{(1)} &= 2, \ell_x^{(2)} = 2 \\ \ell_y^{(1)} &= 30, \ell_z^{(2)} = 20\end{aligned}$$

In contrast to the previous example, now the measurement-specific component is more dominant than the common component and the scales of the two measurements are different.

We compute the eigenvalues flow diagram by applying algorithm 1 with  $N_t = 200$  and  $K = 20$ . In addition, we estimate the CMR using algorithm 4. The eigenvalues flow diagram is depicted in fig. 30, where the point  $t$  along the geodesic path at which the CMR estimation is maximal is marked by a horizontal red line.

We observe that a common eigenvector is detected as a log-linear curve and coincides with the analytic expressions at the boundaries  $t = 0$  and  $t = 1$ . This clear detection is attained despite the small CMR at both measurements. In addition, we observe that the optimal point is obtained near  $t^* \approx 0.6$ , corresponding to the higher CMR of the measurement at  $t = 1$  than of the measurement at  $t = 0$ .

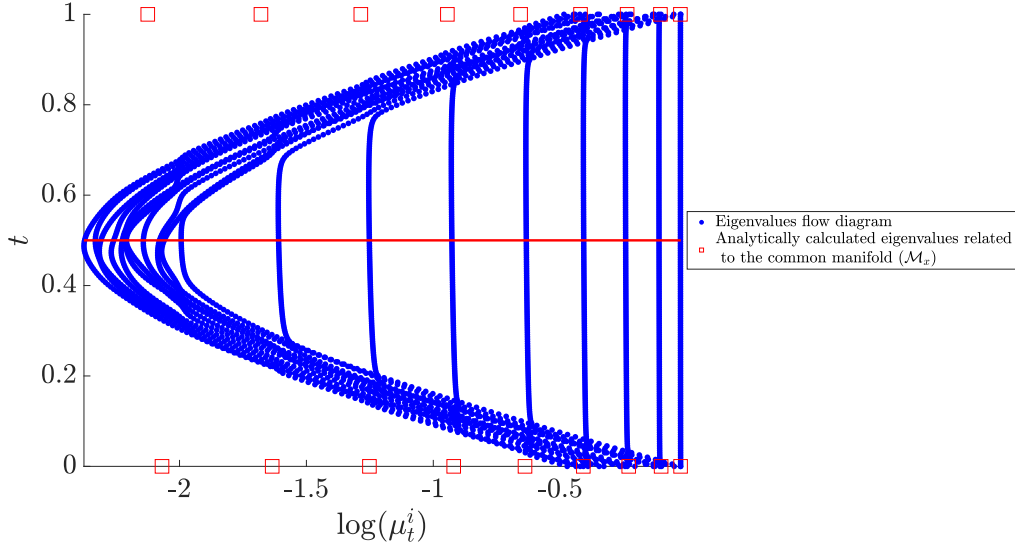


Figure 28: The obtained eigenvalues flow diagram. The point  $t$  at which the CMR is maximal is marked by a horizontal red line.

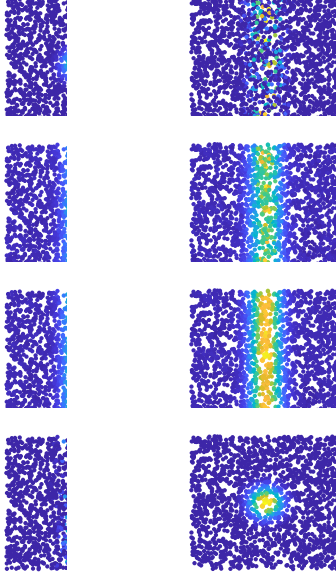


Figure 29: The diffusion patterns obtained along the geodesic path at  $t = 0, 0.3, t^*, 1$ . At the left column, we plot the measurements from  $\mathcal{O}_1$ , and at the right column we plot the measurements from  $\mathcal{O}_2$ . The measurements are colored as follows. The colors from the top row to the bottom row correspond to the diffusion patterns based on  $\gamma(0) = \mathbf{K}_1$ ,  $\gamma(0.3)$ ,  $\gamma(t^*)$ , and  $\gamma(1) = \mathbf{K}_2$ .

fig. 31 presents the diffusion patterns, similarly to fig. 29. Here, we observe the importance of a correct choice for the optimal  $t$  in obtaining a diffusion pattern that saturates along the measurement-specific variable (vertical axis) and diffuses only along the common variable (horizontal axis).

Thus far, the simulations involved only linear measurement functions  $g$  and  $h$ , which led to a smooth isometric embedding of the respective product manifolds  $\mathcal{M}_x \times \mathcal{M}_y$  and  $\mathcal{M}_x \times \mathcal{M}_z$  into the observable spaces. Next, we consider nonlinear measurement functions  $h$ , so that the embedding of the product manifold  $\mathcal{M}_x \times \mathcal{M}_z$  is no longer isometric, and as a consequence, the density of the corresponding measurements  $\{s_i^{(2)}\}$  is no longer uniform.

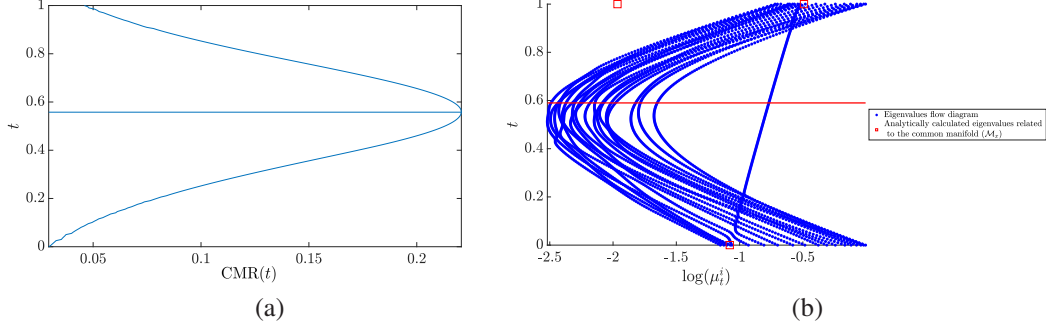
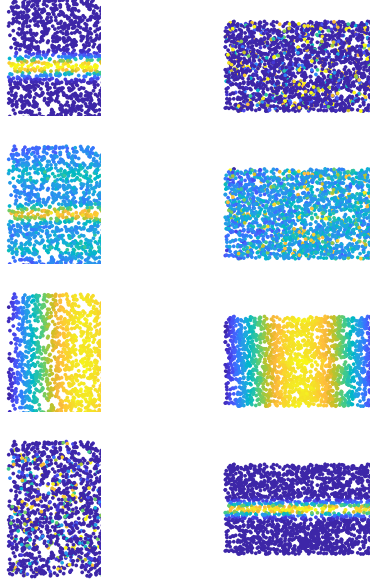


Figure 30: (a) The CMR estimation. (b) The eigenvalues flow diagram.

Figure 31: Diffusion patterns for several points along the geodesic path. At the left column, we plot the measurements from  $\mathcal{O}_1$ , and at the right column we plot the measurements from  $\mathcal{O}_2$ . The measurements are colored as follows. The colors from the top row to the bottom row correspond to the diffusion pattern of  $\gamma(0) = \mathbf{K}_1$ ,  $\gamma(0.3)$ ,  $\gamma(t^*)$ , and  $\gamma(1) = \mathbf{K}_2$ .

Specifically, we consider two measurement functions denoted by  $h_1$  and  $h_2$ . The first function  $h_1$  is given by:

$$h_1(x_i, z_i) = \left( \ell_x^{(2)} x_i, \ell_z^{(2)} (1 - \sqrt{z_i}) \right)$$

where the measurement-specific variable  $z_i$  is non-linearly mapped, and the common variable  $x_i$  is scaled. The second function  $h_2$  is given by:

$$h_2(x_i, z_i) = \left( \ell_x^{(1)} (1 - \sqrt{x_i}), \ell_z^{(2)} z_i \right)$$

where the common variable  $x_i$  is non-linearly mapped, and the measurement-specific variable  $z_i$  is scaled. The observation function  $g$  remains linear, and is given by

$$s_i^{(1)} = g(x_i, y_i) = \left( \ell_x^{(1)} x_i, \ell_y^{(1)} y_i \right)$$

Similarly as before, we consider the following three manifolds  $\mathcal{M}_x = \mathcal{M}_y = \mathcal{M}_z = [0, 1]$ , and the following scaling parameters:

$$\begin{aligned} \ell_x^{(1)} &= 1, \ell_x^{(2)} = 1 \\ \ell_y^{(1)} &= 1, \ell_z^{(2)} = 1 \end{aligned}$$

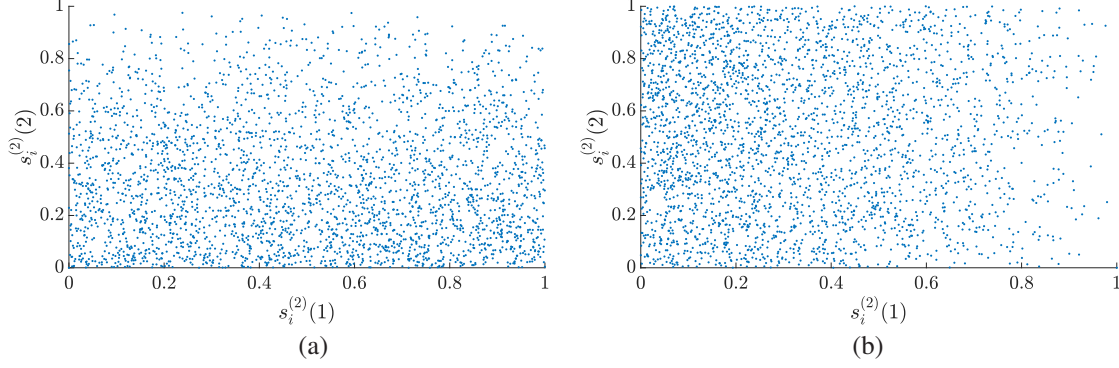


Figure 32: The obtained measurements  $\{s_i^{(2)}\}_{i=1}^n$  with (a)  $h_1$  and (b)  $h_2$ .

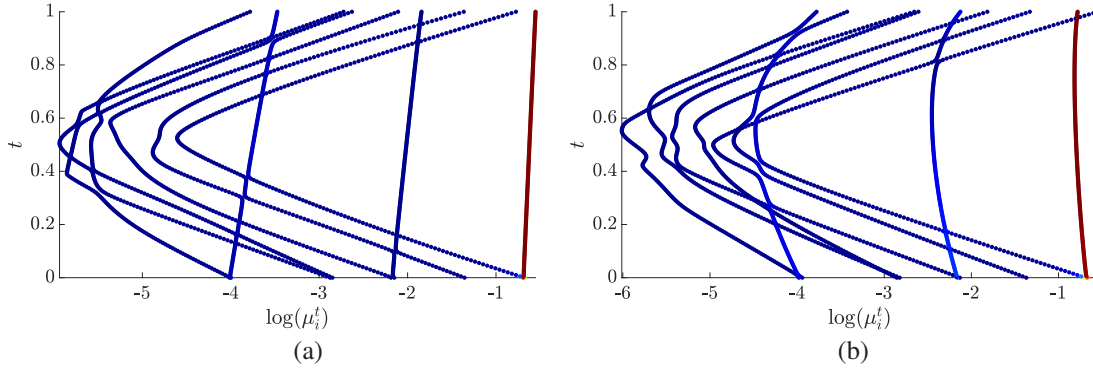


Figure 33: The eigenvalues flow diagrams applied to the measurements with (a)  $h_1$  and (b)  $h_2$ . Each point in the diagrams is colored according to the correlation between its corresponding eigenvector and the vector of common variable realizations  $\{x_i\}_{i=1}^n$ .

We generate  $n = 2,000$  points  $(x_i, y_i, z_i)$  where  $x_i \in \mathcal{M}_x$ ,  $y_i \in \mathcal{M}_y$ , and  $z_i \in \mathcal{M}_z$  are sampled uniformly and independently from each manifold. Then, we calculate the corresponding measurements:  $\{s_i^{(1)}, s_i^{(2)}\}_{i=1}^n$  twice: once with  $h_1$  and once with  $h_2$ . The obtained two sets of measurements  $\{s_i^{(2)}\}_{i=1}^n$  are depicted in fig. 32. Indeed, we observe the non-uniform density along the vertical axis in fig. 32(a) (corresponding to the measurement-specific variable) and along the horizontal axis in fig. 32(b) (corresponding to the common variable).

We apply algorithm 1 to each set with  $N_t = 200$  and  $K = 10$ , and obtain the corresponding eigenvalues flow diagrams, which are depicted in fig. 33.

We observe in fig. 33(a) that the deformation caused by  $h_1$  does not affect the appearance of the common eigenvectors, and they maintain the prescribed log-linear behavior. Conversely, we observe in fig. 33(b) that the deformation caused by  $h_2$  results in an eigenvalues flow diagram, where the common spectral components (which are not strictly common eigenvectors anymore) are characterized by a slightly curved lines. Yet, they are still very distinct compared to the measurement-specific components, and the high correlation of the principal common component with the common variable is maintained.

Next we consider a setting in which the data acquired by each measurement function forms a 2-torus embedded in 3D. The hidden variables are the poloidal and the toroidal angles, and the dominance of the measurement-specific components in each measurement depends on the ratio between the radii. Here we consider the case where the common hidden variable is the poloidal angle, implying that the measurement-specific components are more dominant.

The three hidden angles are drawn uniformly and independently from three manifolds  $\mathcal{M}_x = \mathcal{M}_y = \mathcal{M}_z = [0, 2\pi]$ , giving rise to the tuples  $\{(x_i, y_i, z_i)\}_{i=1}^n$ , where  $x_i \in \mathcal{M}_x$ ,  $y_i \in \mathcal{M}_y$ , and  $z_i \in \mathcal{M}_z$ . The measurements are given by:

$$\begin{aligned} s_i^{(1)} &= ((R_1 + r_1 \cos(x_i)) \cos(y_i), (R_1 + r_1 \cos(x_i)) \sin(y_i), r_1 \sin(x_i)) \\ s_i^{(2)} &= ((R_2 + r_2 \cos(x_i)) \cos(z_i), (R_2 + r_2 \cos(x_i)) \sin(z_i), r_2 \sin(x_i)) \end{aligned}$$

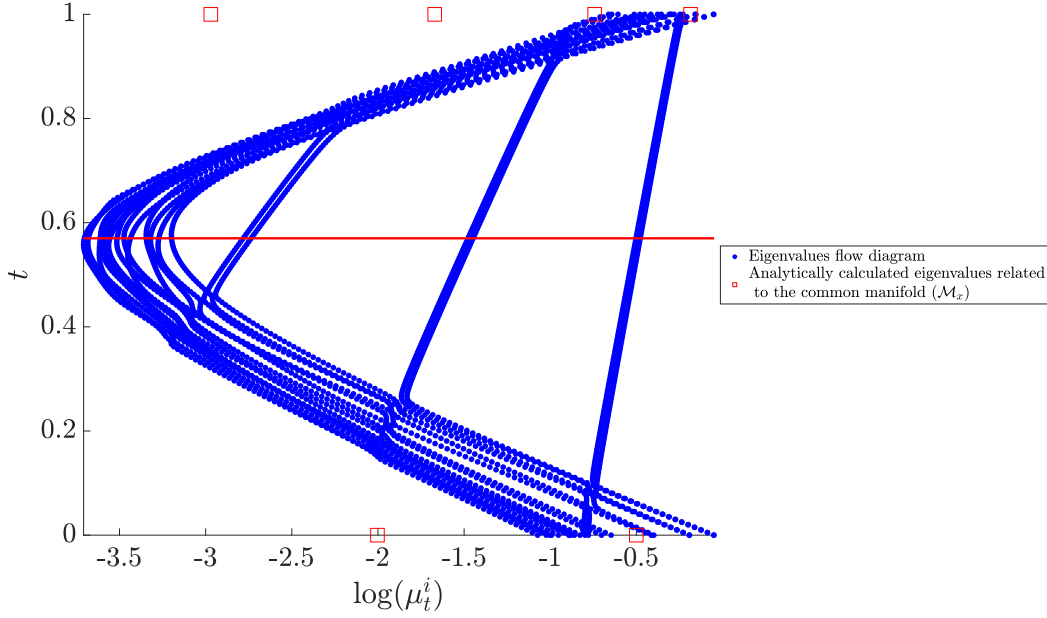


Figure 34: The eigenvalues flow diagram obtained by applying algorithm 1 to  $(s_i^{(1)}, s_i^{(2)})$  in the 2D tori example. The point  $t$  at which the CMR is maximal is marked by a horizontal red line. The analytically calculated eigenvalues at the boundaries of the diagram (at  $t = 0$  and  $t = 1$ ) are computed based on eq. (49).

where the parameters  $R_v$  and  $r_v$  denote the major and minor radii in the measurement  $v = 1, 2$ . Specifically, here we set:

$$\begin{aligned} R_1 &= 10; r_1 = 5 \\ R_2 &= 10; r_2 = 3 \end{aligned}$$

We compute the eigenvalues flow diagram by applying algorithm 1 to the measurements and present it in fig. 34. Same as in the previous example, we analytically compute the eigenvalues of the Laplace-Beltrami operator defined on the sampled manifolds (2-tori) and overlay them on the diagram. The eigenvalues of the Laplace-Beltrami operator (with Neumann boundary conditions) on the manifolds  $\mathcal{O}_1 = \mathcal{O}_2 = \mathcal{T}^2$  are given by (see Lemma 6.5.1 in [49]):

$$\begin{aligned} \lambda_1^{(k_x, k_y)} &= \left( \frac{\lfloor \frac{k_x}{2} \rfloor}{2r_1} \right)^2 + \left( \frac{\lfloor \frac{k_y}{2} \rfloor}{2R_1} \right)^2 \\ \lambda_2^{(k_x, k_z)} &= \left( \frac{\lfloor \frac{k_x}{2} \rfloor}{2r_2} \right)^2 + \left( \frac{\lfloor \frac{k_z}{2} \rfloor}{2R_2} \right)^2 \end{aligned} \quad (49)$$

and the eigenvalues of the discrete operator are computed by eq. (6) (according [34, equation 7]). We note that due to the periodic boundaries of the torus the obtained eigenvalues exhibit multiplicity of 2.

In fig. 34, we observe that eigenvalues with log-linear flow indeed coincide with the analytically computed eigenvalues corresponding to the common variables (with indices  $k_y = 0$  and  $k_z = 0$ ).

The diffusion patterns at  $t = 0, 0.3, t^*, 1$  are shown in fig. 35. We observe that at  $t^*$ , the diffusion is along the poloidal angle, which corresponds to the common variable. In addition, we observe that this is not the case using the other values  $t = 0, 0.3, 1$ .

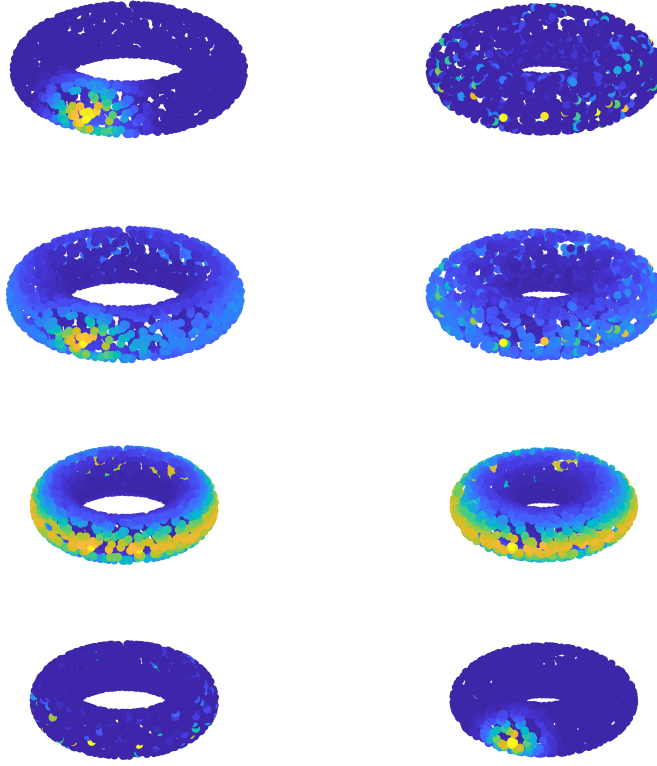


Figure 35: Diffusion patterns for several points along the geodesic path. At the left column, we plot the measurements from  $\mathcal{O}_1$ , and at the right column we plot the measurements from  $\mathcal{O}_2$ . The measurements are colored as follows. From the top row to the bottom row the colors correspond to the diffusion pattern of  $\gamma(0) = \mathbf{K}_1$ ,  $\gamma(0.3)$ ,  $\gamma(t^*)$ , and  $\gamma(1) = \mathbf{K}_2$ .

Next, we repeat the latter simulation, but with a setting in which the common hidden variable represents the torodial angle in each measurement, i.e., the data in each measurement is given by the following expressions:

$$\begin{aligned} s_{1,i}^{(1)} &= (R_1 + r_1 \cos(y_i)) \cos(x_i) & ; & \quad s_{1,i}^{(2)} = (R_2 + r_2 \cos(z_i)) \cos(x_i) \\ s_{2,i}^{(1)} &= (R_1 + r_1 \cos(y_i)) \sin(x_i) & ; & \quad s_{2,i}^{(2)} = (R_2 + r_2 \cos(z_i)) \sin(x_i) \\ s_{3,i}^{(1)} &= r_1 \sin(y_i) & ; & \quad s_{3,i}^{(2)} = r_2 \sin(z_i) \end{aligned}$$

The resulting eigenvalues flow diagram is depicted in fig. 36. We observe that the common eigenvectors are detected and appear as log-linear curves. In addition, with respect to the previous example, we now observe the multiplicity of the eigenvalues.

The diffusion patterns at  $t = 0, t = 0.3, t = t^*$  and  $t = 1$  are shown in fig. 37.

We conclude this section by providing additional results to the real data application described in section 6.1. In section 6.1 we presented the benefits of using the proposed framework for estimating the Acetaldehyde concentrations from sensors 5 and sensor 11. In this subsection we present an additional example based on another pair of sensors: sensor 3 and sensor 14.

In fig. 38, we show the raw data acquired by sensor 3 as a function of the Ethylene concentration for each record in the dataset. We observe that also in this case, when exposed to the same analyte under identical conditions, the responses of the sensors are inconsistent. Hence, the accuracy of estimating the Ethylene concentrations from one sensor only is limited.

We repeat the procedure from section 6.1. The eigenvalues flow diagram of the leading 10 components with the corresponding insets and scatter plots are depicted in fig. 39. Compared to the result presented in the paper, we

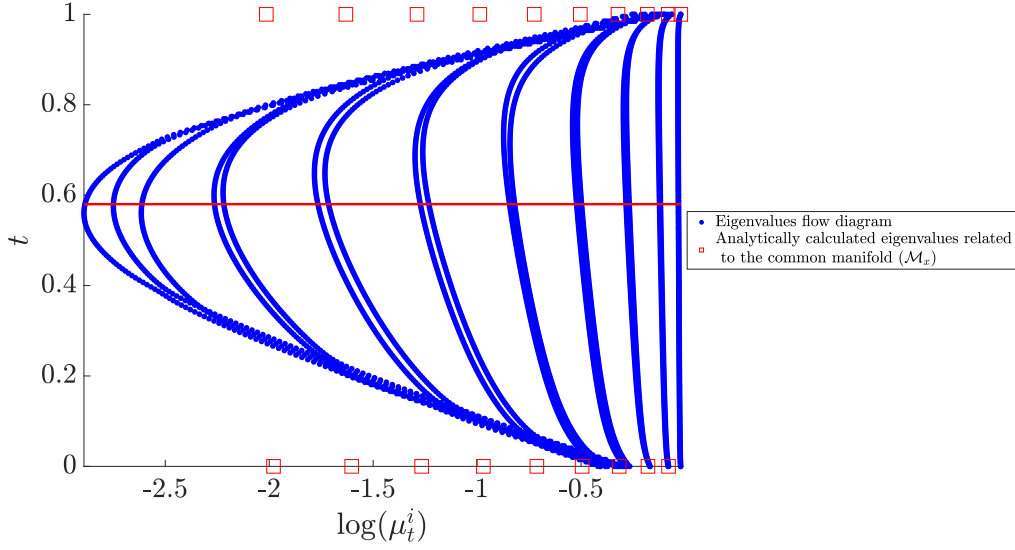


Figure 36: The eigenvalues flow diagram. The point  $t$  at which the CMR is maximal is marked by a horizontal red line.

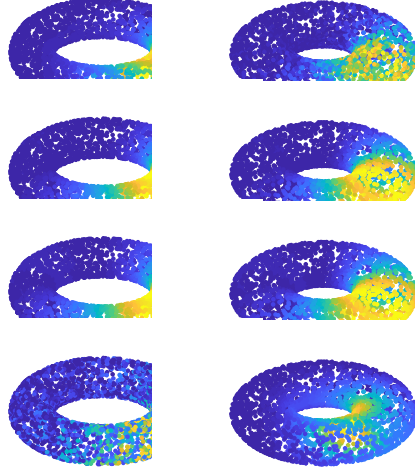


Figure 37: Same as fig. 35 but for the setting where the common variable is the torodial angle.

observe that this case is more complicated because none of the 3 leading components of the kernel  $\mathbf{K}_1$  is related to the Ethylene concentration. Nevertheless, we observe similar trends as in the example of the Acetaldehyde prediction presented in the paper. First, the components which do not decay quickly exhibit high correlation with the Ethylene concentration. Second, the mutual-relationships between the common components and the Ethylene concentration do not change along the geodesic path; for instance, we observe in the insets that the scatter plot of the principal component of  $\gamma(0.5)$  is identical to the scatter plot of the third leading component of  $\gamma(1)$ . Third, the measurement-specific components, i.e. the components which decay quickly, do not exhibit any correspondence with the Ethylene concentration and seem to be related to measurement-specific outliers.

## D Geodesic paths on $\mathcal{S}^+(p, n)$

The metric defined in eq. (1), which is called the affine-invariant metric, is suitable for strictly positive matrices in  $\mathcal{P}(n)$ . In practice, the dimension of the kernel matrices is determined by the size of the dataset  $n$ , which is typically higher than the intrinsic dimensionality of the data. As a result, the matrices might consist of small, negligible eigenvalues, and as a consequence, would not, in effect, be strictly positive.



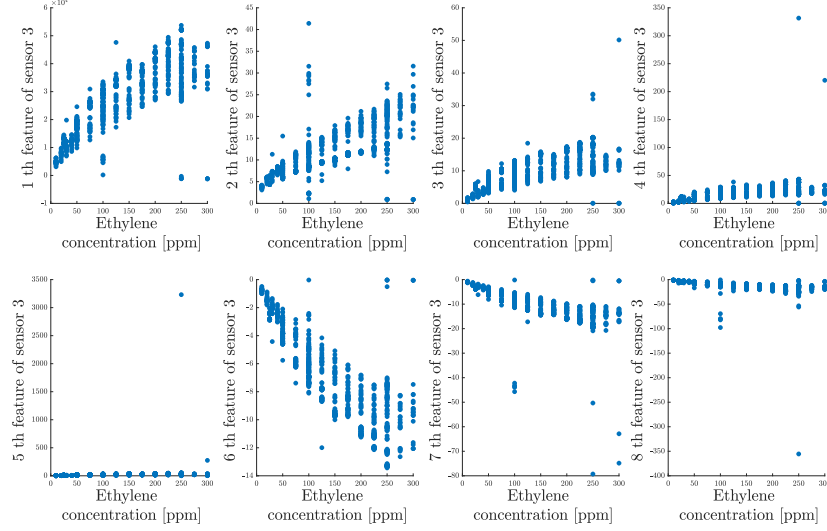


Figure 38: Raw data acquired from sensor 3 in the sensors array as a function of the Ethylene concentration. In each subplot, we present the scatter plot of one out of 8 features (8 different aggregations).

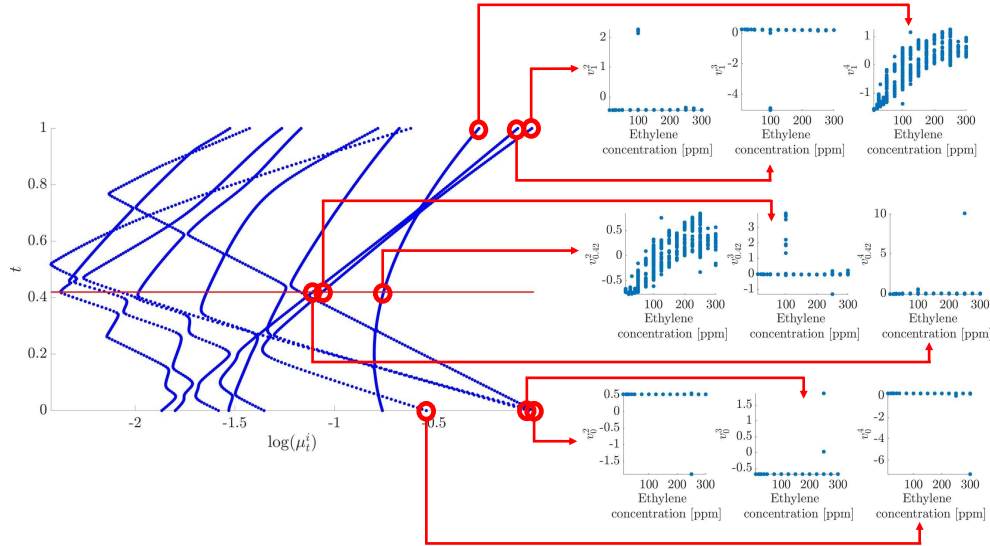


Figure 39: Eigenvalues flow diagram obtained by applying algorithm 1 to the measurements acquired by the 3rd and 11th sensors from the E-Nose dataset. The insets display 9 scatter plots of selected eigenvectors as functions of the Ethylene concentration. The point at which the CMR is maximal is marked by a horizontal line.

In addition, treating small positive eigenvalues as zeros has another important merit. Concretely, restricting the rank of an  $n \times n$  matrix to  $p < n$  reduces the complexity of typical matrix computations such as SVD and EVD from  $O(n^3)$  to  $O(n^2p)$ .

In [37] the authors introduce a metric that extends the affine-invariant metric defined on strictly positive matrices to the set of symmetric positive semi-definite  $n \times n$  matrices  $\mathcal{S}^+(p, n)$  with a fixed rank  $p < n$ . The proposed metric inherits most of the useful properties of the affine-invariant metric, e.g., it is invariant to rotations, scaling, and pseudo-inversion.

Although the exact closed-form expression of the geodesic path is not provided, the authors utilize the fact that the set  $\mathcal{S}^+(p, n)$  admits a quotient manifold representation:

$$\mathcal{S}^+(p, n) \approx (V_{n,p} \times \mathcal{P}(p)) / O(p)$$

where  $V_{n,p}$  is the Stiefel manifold, i.e., the set of  $n \times p$  matrices with orthonormal columns:  $U^T U = I_p$  and  $O(p)$  is the orthogonal group in dimension  $p$ , and propose the following approximation based on the horizontal geodesic path in this space. Consider two matrices  $\mathbf{A}$  and  $\mathbf{B}$  in  $\mathcal{S}^+(p, n)$ , and let  $\mathbf{V}_A$  and  $\mathbf{V}_B$  be two matrices that span the range of  $\mathbf{A}$  and the range of  $\mathbf{B}$ , respectively. The approximation of the geodesic path between  $\mathbf{A}$  and  $\mathbf{B}$  is computed as follows:

1. Calculate the SVD decomposition of  $\mathbf{V}_A^T \mathbf{V}_B$ , such that:

$$\mathbf{V}_A^T \mathbf{V}_B = \mathbf{O}_A \mathbf{S}_{AB} \mathbf{O}_B^T$$

2. Denote:

$$\begin{aligned} \mathbf{U}_A &\triangleq \mathbf{V}_A \mathbf{O}_A \\ \mathbf{U}_B &\triangleq \mathbf{V}_B \mathbf{O}_B \\ \boldsymbol{\Theta} &\triangleq \arccos(\mathbf{S}_{AB}) \\ \mathbf{X} &= (\mathbf{I} - \mathbf{U}_A \mathbf{U}_A^T) \mathbf{U}_B (\sin(\boldsymbol{\Theta}))^{-1} \\ \mathbf{R}_A^2 &= \mathbf{U}_A^T \mathbf{A} \mathbf{U}_A \\ \mathbf{R}_B^2 &= \mathbf{U}_B^T \mathbf{B} \mathbf{U}_B \end{aligned}$$

3. The Grassman geodesic path connecting  $\text{range}(\mathbf{A})$  and  $\text{range}(\mathbf{B})$  is given by:

$$\mathbf{U}(t) = \mathbf{U}_A \cos(\boldsymbol{\Theta} t) + \mathbf{X} \sin(\boldsymbol{\Theta} t)$$

for  $t \in [0, 1]$ .

4. The associated geodesic path in  $\mathcal{P}(p)$  connecting  $\mathbf{R}_A^2$  and  $\mathbf{R}_B^2$  is given by:

$$\mathbf{R}^2(t) = \mathbf{R}_A \exp(t \log(\mathbf{R}_A^{-1} \mathbf{R}_B^2 \mathbf{R}_A^{-1})) \mathbf{R}_A$$

5. Finally, the approximation of the geodesic path between  $\mathbf{A}$  and  $\mathbf{B}$  is given by the following curve:

$$\hat{\gamma}(t) = \mathbf{U}(t) \mathbf{R}^2(t) \mathbf{U}^T(t) \quad (50)$$

According to Theorem 2 in [37],  $\gamma(t)$  admits the following properties:

- $\gamma(t) \in \mathcal{S}^+(p, n)$  for every  $t \in [0, 1]$ .
- The curve  $(\mathbf{U}(t), \mathbf{R}^2(t))$  is a horizontal lift of  $\gamma(t)$  and it is a geodesic path in  $V_{n,p} \times \mathcal{P}(p)$ .
- The total length of  $\gamma(t)$  is given by:

$$\ell^2(\gamma) = \|\boldsymbol{\Theta}\|_F^2 + k \|\log(\mathbf{R}_A^{-1} \mathbf{R}_B^2 \mathbf{R}_A^{-1})\|_F^2$$

where  $k$  is a positive constant. The resulting curve is invariant to pseudo-inversion and to the group action by congruence of orthogonal transformations and scaling.

Viewing matrices in  $\mathcal{S}^+(p, n)$  as flat ellipsoids in  $\mathbb{R}^n$ , the length of  $\gamma(t)$ ,  $\ell^2(\gamma)$ , consists of two independent components: a distance on the Grassman manifold and a distance on  $\mathcal{P}(p)$ . It is worthwhile noting that  $\gamma(t)$  is not necessarily a geodesic path in  $\mathcal{S}^+(p, n)$  because its length is not the Riemannian distance between  $\mathbf{A}$  and  $\mathbf{B}$  since it does not necessarily satisfy the triangle inequality. However, its length provides a meaningful measure of proximity between  $\mathbf{A}$  and  $\mathbf{B}$ .

In practice, when the kernel matrices  $\mathbf{K}_1$  and  $\mathbf{K}_2$  have small negligible eigenvalues, we assume a fixed rank  $p$  that accommodates the kernels significant eigenvalues. In turn, in Step 2a in algorithm 1, we replace the geodesic on the SPD manifold  $\gamma(t)$  with the approximate geodesic path  $\hat{\gamma}(t)$  eq. (50).

## E Relation to AD

Here, we show the relationship between the proposed interpolation scheme and AD [13]. We begin with two important remarks. First, the main goal of the two methods is different – AD aims to build an embedding that represents the common variables between the two sets of measurements and is not restricted to models where the common variable corresponds to common eigenvectors, whereas the current interpolation scheme primarily provides an analysis tool. Second, in order to establish a tractable connection, we consider a variant of AD [13].

Let  $t \in \mathbb{Q}$  in  $(0, 1)$ , and let  $s_1, s_2 \in \mathbb{N}$  be two positive integers such that  $t = \frac{s_2}{s_1 + s_2}$ . Consider a common eigenvector  $v \in \mathbb{R}^n$  of  $\mathbf{K}_1$  and  $\mathbf{K}_2$  with corresponding eigenvalues  $\mu_1$  and  $\mu_2$ . By definition, we have:

$$\begin{aligned}\mathbf{K}_1 v &= \mu_1 v = \exp\left(-\frac{(\epsilon^{(1)})^2}{4}\lambda_1\right)v \\ \mathbf{K}_2 v &= \mu_2 v = \exp\left(-\frac{(\epsilon^{(2)})^2}{4}\lambda_2\right)v\end{aligned}$$

where  $\lambda_1$  and  $\lambda_2$  are the corresponding eigenvalues of the continuous counterparts of  $\mathbf{K}_1$  and  $\mathbf{K}_2$ , respectively [34]. By proposition 1,  $v$  is also an eigenvector of  $\gamma(t)$  with the following eigenvalue:

$$\mu_{\gamma(t)} = \mu_1^{1-t} \mu_2^t = \mu_1^{\frac{s_1}{s_1+s_2}} \mu_2^{\frac{s_2}{s_1+s_2}}$$

For the purpose of AD, construct  $\tilde{\mathbf{K}}_1$  and  $\tilde{\mathbf{K}}_2$  with finer scales given by:

$$\tilde{\epsilon}^{(1)} = \frac{\epsilon^{(1)}}{\sqrt{s_1 + s_2}} \quad \tilde{\epsilon}^{(2)} = \frac{\epsilon^{(2)}}{\sqrt{s_1 + s_2}}$$

similarly to the construction of  $\mathbf{K}_1$  and  $\mathbf{K}_2$ . Namely, we build two kernels with scales smaller by a factor of  $\sqrt{s_1 + s_2}$ . Then, we define the AD operator  $\gamma_{AD}(t)$  by:

$$\gamma_{AD}(t) = \left(\tilde{\mathbf{K}}_1\right)^{s_1} \left(\tilde{\mathbf{K}}_2\right)^{s_2}.$$

In the context of AD, this operator implies applying  $s_2$  diffusion steps using  $\tilde{\mathbf{K}}_2$  followed by  $s_1$  diffusion steps using  $\tilde{\mathbf{K}}_1$ .

Revisiting the common eigenvector  $v$  considered above, we have:

$$\begin{aligned}\tilde{\mathbf{K}}_1 v &= \exp\left(-\frac{(\tilde{\epsilon}^{(1)})^2}{4(s_1 + s_2)}\lambda_1\right)v = \mu_1^{1/(s_1+s_2)}v \\ \tilde{\mathbf{K}}_2 v &= \exp\left(-\frac{(\tilde{\epsilon}^{(2)})^2}{4(s_1 + s_2)}\lambda_2\right)v = \mu_2^{1/(s_1+s_2)}v\end{aligned}$$

namely,  $v$  is an eigenvector of  $\tilde{\mathbf{K}}_1$  and  $\tilde{\mathbf{K}}_2$  with eigenvalues  $\mu_1^{1/(s_1+s_2)}$  and  $\mu_2^{1/(s_1+s_2)}$ . Therefore,  $v$  is also an eigenvector of  $\gamma_{AD}(t)$ :

$$\gamma_{AD}(t)v = \left(\tilde{\mathbf{K}}_1\right)^{s_1} \left(\tilde{\mathbf{K}}_2\right)^{s_2} v = \mu_1^{\frac{s_1}{s_1+s_2}} \mu_2^{\frac{s_2}{s_1+s_2}} v.$$

with eigenvalue given by

$$\mu_1^{\frac{s_1}{s_1+s_2}} \mu_2^{\frac{s_2}{s_1+s_2}} = \mu_1^{1-t} \mu_2^t v.$$

We obtain that  $v$  is an eigenvector of both  $\gamma(t)$  and  $\gamma_{AD}(t)$  with the same eigenvalue.

When  $\mathbf{K}_1$  and  $\mathbf{K}_2$  share the same set of eigenvectors, i.e.  $[\mathbf{K}_1, \mathbf{K}_2] = 0$ , then the relationship to AD becomes tighter.

**Proposition 10** *If  $[\mathbf{K}_1, \mathbf{K}_2] = 0$ , then  $\gamma(t) = \gamma_{AD}(t)$  for every  $t \in \mathbb{Q}$ .*

**Proof 14** *If  $[\mathbf{K}_1, \mathbf{K}_2] = 0$  then they both have the same set of eigenvectors, i.e. we can write:*

$$\begin{aligned}\mathbf{K}_1 &= \mathbf{U}\mathbf{S}_1\mathbf{U}^T \\ \mathbf{K}_2 &= \mathbf{U}\mathbf{S}_2\mathbf{U}^T\end{aligned}$$

*Therefore:*

$$\begin{aligned}\gamma(t) &= \mathbf{K}_1^{1/2}(\mathbf{K}_1^{-1/2}\mathbf{K}_2\mathbf{K}_1^{-1/2})^t\mathbf{K}_1^{1/2} = \\ &= \mathbf{U}\mathbf{S}_1^{1/2}\mathbf{U}^T(\mathbf{U}\mathbf{S}_1^{-1/2}\mathbf{U}^T\mathbf{U}\mathbf{S}_2^{1/2}\mathbf{U}^T\mathbf{U}\mathbf{S}_1^{-1/2}\mathbf{U}^T)^t\mathbf{U}\mathbf{S}_1^{1/2}\mathbf{U}^T = \\ &= \mathbf{U}\mathbf{S}_1^{(1-t)}\mathbf{S}_2^t\mathbf{U}^T.\end{aligned}$$

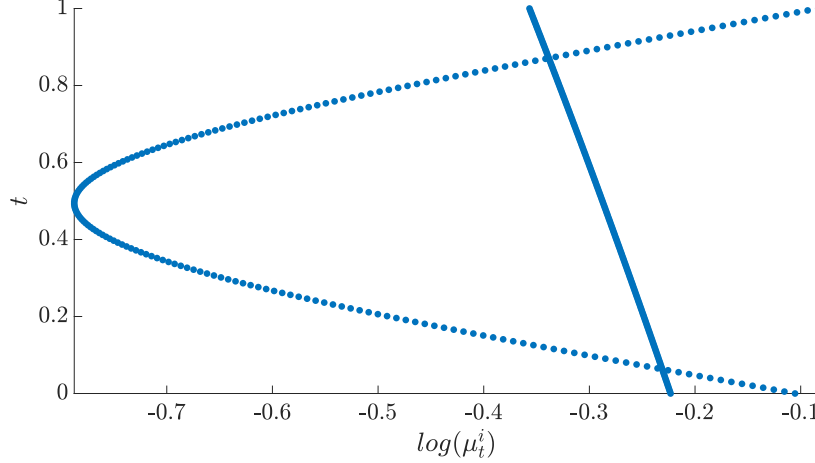


Figure 40: An illustrative eigenvalues flow diagram consisting of two components.

Similarly:

$$\begin{aligned}\tilde{\mathbf{K}}_1 &= \mathbf{U}\mathbf{S}_1^{1/(s_1+s_2)}\mathbf{U}^T \\ \tilde{\mathbf{K}}_2 &= \mathbf{U}\mathbf{S}_2^{1/(s_1+s_2)}\mathbf{U}^T\end{aligned}$$

Therefore:

$$\begin{aligned}\gamma_{AD}(t) &= \left(\tilde{\mathbf{K}}_1\right)^{s_1} \left(\tilde{\mathbf{K}}_2\right)^{s_2} \\ &= \mathbf{U}\mathbf{S}_1^{(1-t)}\mathbf{S}_2^t\mathbf{U}^T = \gamma(t)\end{aligned}$$

We end this section with a couple of remarks. First, the case in which  $[\mathbf{K}_1, \mathbf{K}_2] = 0$  is typically not of interest, since it implies that the two kernels have only common eigenvectors. Second,  $\gamma_{AD}(t)$  is not designed to be symmetric; AD in its original formulation in [13] includes an additional step of constructing a new kernel from a kernel analogous to  $\gamma_{AD}(0.5)$  here. Conversely,  $\gamma(t)$  is symmetric and positive, and therefore, may facilitate spectral embedding directly. In 6 we only present empirical results, yet this direction calls for additional investigation, which will be the subject of future work.

## F Implementations

In this section we describe in detail the procedures mentioned in section 4.4, aiming to automatically resolve the trajectories in the flow diagram and extract the useful information.

### F.1 Common components identification

We use the results presented in section 4.3 and in section 5.1 in order to identify the sequence of the different components along the geodesic path. At each point  $t_0$  along the geodesic path we would like to assign to each component of  $\gamma(t_0)$  a unique identifier which is consistent with adjacent points along the geodesic path  $\gamma(t)$ , where  $t \in [t_0 - \Delta t, t_0 + \Delta t]$  and  $\Delta t$  is a locality parameter. This tracking problem can be defined as a matching or as an assignment problem. For convenience, rather than finding the assignment at each point  $t_0$ , we will find the permutation at each  $t_0$  with respect to a reference order of eigenvalues. This change, which is only semantic, allows us to formulate the problem in a concise and elegant way. In order to illustrate our goal, consider the synthetic eigenvalues flow diagram depicted in fig. 40. Let  $\mu_{t_i}^j$  denote the  $j$ th eigenvalue of  $\gamma(t_i)$ . For simplicity, we set the order of the eigenvalues at  $t = 0$  as our reference order, i.e.,  $1 = \mu_0^0 > \mu_0^1 > \dots > \mu_0^n$ . Note that the reference order consists of an implicit assumption, implying that the eigenvalues at  $t = 0$  have no multiplicity. Let  $\Pi_t : \{1, \dots, N_e\} \rightarrow \{1, \dots, N_e\}$  denote the permutation at point  $t$  with respect to the reference at  $t = 0$ . Accordingly, the permutations we aim to find

matching the diagram in fig. 40 are given by:

$$\Pi_t = \begin{cases} (1, 2), & 0 \leq t \leq 0.06 \\ (2, 1), & 0.06 < t < 0.88 \\ (1, 2), & 0.88 \leq t \leq 1 \end{cases}$$

In general, when considering  $N_e > 2$  components, the component at point  $t$  corresponding to the  $k$ th component ( $1 \leq k \leq N_e$ ) at  $t = 0$  is specified by  $\Pi_t(k)$ . Consider a discrete uniform grid of  $t \in [0, 1]$  along the geodesic path:  $\{t_i\}_{i=1}^{N_t}$ , and their corresponding components at each point  $\{\mu_{t_i}^j, v_{t_i}^j\}$ , where  $i = 1, \dots, N_t$  is the index of the point on the grid along the geodesic path, and  $j = 1, \dots, N_e$  is the index of the component. When estimating  $\Pi_t$  the following considerations should be taken. The first consideration is a local one and address the relation between the permutation at a certain point  $t_i$  to the successive and proceeding permutations at  $t_{i-1}$  and  $t_{i+1}$ , respectively. According to the smoothness of the flow we impose that  $\Pi_{t_{i+1}}$  should be equal to  $\Pi_{t_i}$  and  $\Pi_{t_{i-1}}$  or it may contain only one or two swaps. Second, the difference between two consecutive permutations  $\Pi_{t_{j+1}}$  and  $\Pi_{t_j}$  can only contain swaps between eigenvalues with similar values. The third consideration is global and address the relationship between the permutation at a certain point  $t_i$  and the permutations at each point on the grid. Given two permutations  $\Pi_{t_j}$  and  $\Pi_{t_k}$ , we encode the correspondence between the associated eigenvectors by requiring high correlations

$$\langle v_{t_j}^{\Pi_{t_j}(i)}, v_{t_k}^{\Pi_{t_k}(i)} \rangle,$$

for any  $i = 1, \dots, N_e$ .

Since the log-linear behavior is guaranteed only when there exists a common eigenvector, the proposed implementations do not rely on this log-linear assumption. However, the log-linear flow can be easily incorporated as an additional prior within the proposed framework. Based on these considerations, we propose a criterion and pick the set of permutations that maximize this criterion. Since the permutation at each point depends on the permutations in adjacent points, the proposed criterion is evaluated on the entire set of permutations on the grid. Considering  $N_t$  points on the grid of  $t \in [0, 1]$ , and  $N_e$  components, the number of possible sets to be evaluated is  $(N_e!)^{N_t}$ ; calculating a certain criterion  $(N_e!)^{N_t}$  times is not a feasible. Instead, we propose to find  $\Pi_t$  by solving a dynamic programming problem using a small variant of the seminal Viterbi algorithm [50]. Importantly, the ability to use standard dynamic programming facilitates efficient solutions to the problem, which might have not been feasible to be resolved otherwise. We use a terminology which is commonly used in the context of the Viterbi algorithm. Let  $s$  denote a hidden state which is defined as a tuple of  $L$  successive permutations:

$$s = (\Pi_1, \Pi_2, \dots, \Pi_L)$$

where  $L$  is a tunable scale parameter. Let  $\mathcal{S}$  denote the set of all hidden states, where the total number of states is given by  $N_s = |\mathcal{S}| = (N_e!)^L$ . Access to the  $k$ th permutation in the state (tuple)  $s$  is given by  $s(k)$ . Consider a sequence of hidden states, where  $x_{t_i} \in \mathcal{S}$  is the state at  $t_i$ , and suppose  $x_{t_i} = (\Pi_{t_{i-L+1}}, \Pi_{t_{i-L+2}}, \dots, \Pi_{t_i})$ . The transition probability  $\Pr(x_{t_i}, x_{t_{i+1}})$  between two successive hidden-states in the sequence  $x_{t_i}$  and  $x_{t_{i+1}}$  is determined according to the above considerations. First, given  $x_{t_i}$ , for the consistency of the sequence,  $x_{t_{i+1}}$  must be of the form  $(\Pi_{t_{i-L+2}}, \dots, \Pi_{t_i}, \Pi_{t_{i+1}})$ , i.e., the sequence of hidden states should correspond to a sequence of permutations. Otherwise,  $\Pr(x_{t_i}, x_{t_{i+1}}) = 0$ . Then, non-zero transition probabilities are defined with respect to the first permutation of  $x_{t_i}(1)$ , namely,  $\Pi_{t_{i-L+1}}$ , and the last permutation of  $x_{t_{i+1}}(L)$ , namely  $\Pi_{t_{i+1}}$ . Particularly, we allow only one or two swaps between  $\Pi_{t_{i-L+1}}$  and  $\Pi_{t_{i+1}}$  in order to impose smoothness.

Explicitly, the transition probability is defined by:

$$\Pr(x_{t_i}, x_{t_{i+1}}) = \begin{cases} 0, & \text{if } \exists j = 1, \dots, L-1 \text{ such that } x_{t_i}(j) \neq x_{t_{i+1}}(j+1) \\ p_1, & \text{if } \forall j = 1, \dots, L-1, x_{t_i}(j) = x_{t_{i+1}}(j+1) \text{ and the difference between} \\ & x_{t_i}(1) \text{ and } x_{t_{i+1}}(L) \text{ consist of only one swap} \\ p_2, & \text{if } \forall j = 1, \dots, L-1, x_{t_i}(j) = x_{t_{i+1}}(j+1) \text{ and the difference between} \\ & x_{t_i}(1) \text{ and } x_{t_{i+1}}(L) \text{ consist of two swaps} \\ 1 - p_1 - p_2, & \text{Otherwise} \end{cases}$$

The proposed transition probability, which depends on 2 hyper-parameters ( $p_1$  and  $p_2$ ), serves as a regularization that dominates smoothness of the most likely sequences of permutations. Now, for each hidden state in the sequence  $x_{t_i}$ , we assign a likelihood score. Let  $V_{t_i}$  be an  $N_e \times n$  matrix, whose rows are the eigenvectors  $v_{t_i}^j$ , ordered according to the reference order. We denote by  $\Pi(V_{t_i})$  an  $N_e \times n$  matrix, which consists of the rows of  $V_{t_i}$  permuted according to  $\Pi$ . Namely, the  $k$ th row of  $\Pi(V_{t_i})$  is the  $\Pi(k)$ th row of  $V_{t_i}$ . Let  $y_{t_i}$  denote an observation of a hidden state in the sequence  $x_{t_i}$ , defined by a tuple of two matrices of eigenvectors:

$$(\Pi_1(V_{t_{i-L+1}}), \Pi_L(V_{t_i}))$$

where  $\Pi_1 = x_{t_i}(1)$  and  $\Pi_L = x_{t_i}(L)$ . The likelihood of an observation  $y_{t_i}$  is defined based on the pairwise correlations between the eigenvectors:

$$\Pr(y_{t_i}|x_{t_i}) = \frac{1}{c} \text{Tr}(\Pi_1(V_{t_i-L+1})\Pi_L(V_{t_i}))^T = \frac{1}{c} \sum_{j=1}^{N_e} \langle v_{t_i-L+1}^{\Pi_1(j)}, v_{t_i}^{\Pi_L(j)} \rangle$$

where  $c$  is a normalization factor. Given this formulation we can use the forward-backward algorithm in order to find the most likely sequence of hidden states. This algorithm is described in details in algorithm 2. By construction, since we impose consistency, the most likely sequence of hidden states forms a sequence of permutations  $\Pi_t$ , which resolves the desired assignment problem. Using the above mentioned notation we can easily define the forward steps.

---

**Algorithm 2** Tracking algorithm

---

**Input:** The geodesic path  $\gamma(t)$

**Output:**  $\Pi_t$  - the permutation at point  $t$  with respect to the reference at  $t = 0$ .

---

- 1: Initialize  $T_1$  - a  $N_s \times N_t$  matrix.  $T_1[i, j]$  denotes the log-probability of the most likely sequence of  $j$  states ending at the  $i$ th state -  $s_i$ , this path will be denoted by:  $\hat{X} = (\hat{x}_{t_1}, \hat{x}_{t_2}, \dots, \hat{x}_{t_j})$  where  $\hat{x}_{t_j} = s_i$ .
- 2: Initialize  $T_2$  - a  $N_s \times N_t$  matrix.  $T_2[i, j]$  denotes the most likely previous state index. I.e.  $T_2[i, j]$  is the index of the state of  $\hat{x}_{t_{j-1}}$ .
- 3: For each state  $j = 1, \dots, N_s$ :
  - a:  $T_1[j, 1] \leftarrow -1$
  - b:  $T_2[j, 1] \leftarrow 0$
- 4: For each observation index  $i = 1, \dots, N_t$ :
  - For each state  $s_j, j = 1, \dots, N_s$ :
    - a:  $T_1[j, i] \leftarrow \max_k \{T_1[k, i-1] + \log(P(y_{t_i}|s_j) + \log(P(x_{t_i} = s_k|x_{t_{i-1}} = s_j)))\}$
    - b:  $T_2[j, i] \leftarrow \arg\max_k \{T_1[k, i-1] + \log(P(y_{t_i}|s_j) + \log(P(x_{t_i} = s_k|x_{t_{i-1}} = s_j)))\}$

Then compute the backward steps:

- 1: Initialize  $Z$  - an  $1 \times N_t$  array.  $Z[i]$  denotes the index of the  $i$ th state within the most likely sequence of states:  $\hat{X}$ .
- 2:  $Z[N_t] \leftarrow \arg\max_k T_1[k, N_t]$
- 3: For each  $i = N_t, \dots, 2$ :
  - a:  $Z[i-1] \leftarrow T_2[Z[i], i]$
- 4: Using the obtained sequence  $Z$  derive the corresponding "hidden-states" sequence:

$$\hat{X} = (\hat{x}_{t_1}, \hat{x}_{t_2}, \dots, \hat{x}_{t_{N_t}}) = (s_{Z[1]}, s_{Z[2]}, \dots, s_{Z[N_t]})$$

- 5: The permutation at point  $t_i$  with respect to the origin:  $t = 0$  is given by:

$$\Pi_{t_i} = \hat{x}_{t_i}(L)$$


---

We conclude this section with few remarks on the differences between algorithm 2 and the standard Viterbi algorithm. First, a naïve implementation requires  $N_s = (N_e!)^L$  states. However, the restriction of the transition probabilities section F.1 allows to effectively reduce the number of states considerably. As a consequence, an efficient beam search implementation, which does not include all possible states, is used.

Second, in the standard Viterbi algorithm, the likelihood is typically fixed and depends on the observation and the hidden state. In contrast, according to our choice of formulation, the likelihood varies and depends on the point along the geodesic path ( $t_i$ ). As a consequence, the likelihood cannot be computed a-priori, and must be computed in each forward step.

## F.2 CMR estimation

We describe two approaches for assessing the "commonality" of a given spectral component. The first approach, described in section F.2.1, relies on the log-linear trajectories of common components. This requires resolving the trajectories using algorithm 2. The second approach, which is described in section F.2.2, utilizes the coherence of each spectral component along the geodesic path.

### F.2.1 CMR estimation using tracking algorithm

We utilize the log-linear behavior described in proposition 1 in order to identify the common components and to estimate the CMR eq. (14). Specifically, according to proposition 1 the logarithm of eigenvalues which are related to the common components varies linearly along the geodesic path with respect to  $t$ ; we propose to utilize this property. We apply the tracking algorithm described in algorithm 2. Let  $\tilde{\mu}_t^i$  be the eigenvalues of the  $i$ th spectral component at  $t = 0$  (i.e.  $\tilde{\mu}_t^i = \mu_t^{\Pi_t(i)}$ ). Then, for each spectral component we compute the length of the linear line connecting  $\log(\tilde{\mu}_0^i)$  and  $\log(\tilde{\mu}_1^i)$  and compare it to the arc-length of the computed eigenvalues:  $\log(\tilde{\mu}_t^i)$ . Using this comparison we can get an assessment for the “commonality” of the  $i$ th spectral component. If the  $i$ th spectral component is a common component, then it would exhibit a log-linear behavior, i.e. the trajectory of the computed eigenvalues:  $\log(\tilde{\mu}_t^i)$  would admit the linear line connecting  $\log(\tilde{\mu}_0^i)$  and  $\log(\tilde{\mu}_1^i)$ , and therefore, the above calculation would yield a low difference. Conversely, if the  $i$ th spectral component is a measurement-specific component, it would be quickly suppressed in a non-linear manner and the above calculation would yield high difference. The algorithm is described in detail in algorithm 3.

---

**Algorithm 3** CMR estimation along the geodesic flow using components identification.

---

**Input:** The geodesic path  $\gamma(t)$ .

**Output:** CMR( $t$ ) estimation for any  $t$  within a discrete uniform grid of  $t \in [0, 1]$ .

- 1: Calculate the trace of each component:  $\{\tilde{\mu}_t^i\}_{i=1}^{N_e}$ , where  $\tilde{\mu}_t^i = \mu_t^{\Pi_t(i)}$  and  $\Pi_t$  is computed according to the proposed algorithm for components identification summarized in Algorithm algorithm 2.
- 2: For each component  $i = 1, 2, \dots, N_e$  compute:
  - a: The obtained arc-length of  $\log(\tilde{\mu}_t^i)$  in  $t \in [0, 1]$  using the following expression:

$$a_i = \int_0^1 \sqrt{1 + \frac{d}{dt} \log(\tilde{\mu}_t^i) dt}.$$

where  $\frac{d}{dt} \log(\tilde{\mu}_t^i)$  is estimated by the discrete differentiation along the uniform grid of  $t \in [0, 1]$ , and similarly  $\int_0^1 (\cdot) dt$  is estimated by the discrete summation.

- b: The length of the linear segment connecting  $\log(\tilde{\mu}_0^i)$  with  $\log(\tilde{\mu}_1^i)$ :

$$l_i = \sqrt{1 + (\log(\tilde{\mu}_1^i) - \log(\tilde{\mu}_0^i))^2}$$

- c: The curvature score, which is defined as follows  $w_i = \frac{a(i) - l(i)}{a(i)}$ . We should notice that  $0 \leq w_i \leq 1$ , and that for  $i \in \mathcal{S}_{common}$  then  $a(i) \rightarrow l(i)$  and as consequence  $w_i \simeq 0$ . We use it as a soft measure for the “commonality” of the  $i$ th spectral component.
- 3: The estimated measure of the CMR at each point along the geodesic path:  $t$  is computed using the following expression:

$$\widehat{\text{CMR}}(t) = \frac{\sum_{i=1}^{N_e} (1 - w_i) \cdot \tilde{\mu}_t^i}{\sum_{i=1}^{N_e} w_i \cdot \tilde{\mu}_t^i}.$$


---

### F.2.2 CMR estimation using components dispersion

The proposed algorithm in algorithm 3 requires the extraction the trajectories of the spectral components along the geodesic path. However, in cases where this extraction is not explicitly required, estimating the CMR can be done in a simpler manner by relying on the empirical results presented in section 5.1.

Rather than first resolving the trajectories of the spectral components along the geodesic path and then assessing their “commonality” by examining their lengths, we can directly assess the “commonality” of a single spectral component by observing its “dispersion” along the geodesic path. In section 5.1 we demonstrated the following: given a certain component  $v \in \mathbb{R}^n$ , and the spectral components of  $\gamma(t)$  at a certain point along the geodesic path,  $\{v_t^k\}_{k=1}^{N_e}$ , the inner products between the given component and the spectral components satisfy:

$$\langle v, v_t^k \rangle = \begin{cases} \delta(k - k_0), & \text{If } v \text{ is a common eigenvector} \\ C, & \text{Otherwise} \end{cases}, k = 1, \dots, N_e$$

where  $k_0$  denotes the (unknown) index of the corresponding eigenvector to  $v$  among  $\{v_t^k\}_{k=1}^{N_e}$ , and  $C$  is a constant. This observation was further explained in the case study presented in B. By utilizing this observation we can assess



the ‘‘commonality’’ of each spectral component by observing its inner-products with the spectral components of the points along the geodesic path. The proposed algorithm is described in detail in algorithm 4.

---

**Algorithm 4** CMR estimation along the geodesic flow using components dispersion.

---

**Input:** The geodesic path  $\gamma(t)$

**Output:** Estimation of  $\text{CMR}(t_0)$  for  $t_0 \in [0, 1]$

- 1: Calculate the cumulative geodesic operator:

$$\Gamma = \prod_{i=1}^{N_t} \gamma(t_i) = \gamma(t_{N_t}) \cdot \dots \cdot \gamma(t_1)$$

Where  $\{t_i\}_{i=1}^{N_t}$  is a discrete uniform grid of  $t \in [0, 1]$

- 2: Calculate the spectral components of  $\Gamma$ , denoted by  $\{u_\Gamma^j\}_{j=1}^n$ .
- 3: For each spectral component  $i = 1, 2, \dots, N_e$  of  $\gamma(t_0)$ , denoted by  $v_{t_0}^i$ :
  - a: Calculate the inner-products with the spectral components of  $\Gamma$ :

$$c_j = \langle v_{t_0}^i, u_\Gamma^j \rangle, j = 1, \dots, n.$$

b: The coherence score is as follows:  $w_i = -\sum_{j=1}^n c_j \log(c_j)$ . We should notice that  $w_i$  is the entropy of the inner-products vector of the  $i$ th component, therefore:  $0 \leq w_i \leq \log(n)$ . For  $i \in \mathcal{S}_{\text{common}}$  then  $w_i \rightarrow 0$  and for  $i \notin \mathcal{S}_{\text{common}}$  then  $w_i \rightarrow \log(n)$ . We use it as a soft measure for the ‘‘mutuality’’ of the  $i$ th component.

- 4: The estimated measure of the  $\text{CMR}(t_0)$  is computed using the following expression:

$$\widehat{\text{CMR}}(t_0) = \frac{\sum_{i=1}^{N_e} (\log(n) - w_i) \mu_{t_0}^i}{\sum_{i=1}^{N_e} w_i \mu_{t_0}^i}.$$

where  $\mu_{t_0}^i$  is the corresponding eigenvalue of  $v_{t_0}^i$ .

---

### F.3 Common variable recovery

Extracting the common kernel can be done in a straight forward manner by calculating  $\gamma(t^*)$ , where  $t^*$  is the point along the geodesic path that maximizes the estimation of the CMR, i.e.:  $t^* = \underset{t}{\operatorname{argmax}} \text{CMR}(t)$ . However, given  $t^*$ , a better estimation of the common kernel can be achieved. Consider the spectral representation of  $\gamma(t^*)$ :

$$\gamma(t^*) = \sum_{i=1}^n \mu_{t^*}^i v_{t^*}^i (v_{t^*}^i)^T$$

We note that further filtering can be done by utilizing the weights from the algorithms used for the CMR estimation. For instance, we can use the curvature scores  $w_i$  from algorithm 3 as coefficients for performing spectral filtering of the non-common residuals of  $\gamma(t^*)$ :

$$\hat{\gamma}(t^*) = \sum_{i=1}^n w_i \mu_{t^*}^i v_{t^*}^i (v_{t^*}^i)^T \quad (51)$$

By doing so we further suppress possible measurement-specific components which may still be dominant within  $\gamma(t^*)$ . The same procedure can be carried using the coherence scores when resolving the trajectories in not essential.

The filtering in eq. (51) can be applied at each point along the geodesic path, and not only at  $t^*$ . For example, consider the 2D flat manifolds presented in section 5.1. The kernels of the measurements,  $\gamma(0) = \mathbf{K}_1$  and  $\gamma(1) = \mathbf{K}_2$ , can be written using the spectral composition as follows:

$$\begin{aligned} \mathbf{K}_1(p, p') &= \sum_{k_x, k_y} \mu_1^{(k_x, k_y)} \varphi_1^{(k_x, k_y)}(x, y) \varphi_1^{(k_x, k_y)}(x', y') \\ \mathbf{K}_2(p, p') &= \sum_{k_x, k_z} \mu_1^{(k_x, k_z)} \varphi_2^{(k_x, k_z)}(x, z) \varphi_2^{(k_x, k_z)}(x', z') \end{aligned}$$

where  $p$  is a point on  $\mathcal{M}_x \times \mathcal{M}_y \times \mathcal{M}_z$  that gives rise to two measurements:  $(x, y)$  and  $(x, z)$ , and similarly for  $p'$ .

Now, the kernel of the hidden common manifold,  $\mathbf{K}_x$ , which is therefore inaccessible, is given by:

$$\mathbf{K}_x(x, x') = \sum_{k_x} \mu_1^{(k_x, k_y=0)} \varphi_1^{(k_x, k_y=0)}(x) \varphi_1^{(k_x, k_y=0)}(x')$$

which can be obtained by a spectral filtering applied to  $K_1$ :

$$\hat{\mathbf{K}}_x(x, x') = \sum_{k_x, k_y} w(k_x, k_y) \mu_1^{(k_x, k_y)} \varphi_1^{(k_x, k_y)}(x, y) \varphi_1^{(k_x, k_y)}(x', y')$$

where  $w(k_x, k_y)$  is a mask indicating the common components only:

$$w(k_x, k_y) = \begin{cases} 0, & k_y > 0 \\ 1, & k_y = 0 \end{cases}$$

As discussed above, these weights can be estimated from the log-linear behavior of the common components, or using the coherence scores. Therefore, although  $\mathbf{K}_x$  is not accessible to us, it can be estimated from the spectral decomposition at any point along the geodesic path. In future work, we plan to further investigate this spectral filtering, and specifically, to incorporate estimations from all the points along the geodesic path except the boundaries:  $0 < t < 1$ .

## G Relationship to spectral independent component analysis

Consider the setting described in section 2. The manifold of  $\mathcal{O}_1$  is the image of  $g$  on the product manifold  $\mathcal{M}_1 = \mathcal{M}_x \times \mathcal{M}_y$  and the manifold of  $\mathcal{O}_2$  is the image of  $h$  on the product manifold  $\mathcal{M}_2 = \mathcal{M}_x \times \mathcal{M}_z$ .

We define the graph Laplacian as follows:

$$\mathbf{L}_i = \mathbf{I} - \mathbf{K}_i$$

for  $i = 1, 2$ , where  $\mathbf{K}_i$  is the kernel built from the measurements 10.

By [51], the discrete graph Laplacians  $\mathbf{L}_1$  and  $\mathbf{L}_2$  converge to the continuous Laplace-Beltrami operators  $\Delta_1$  and  $\Delta_2$ , when the number of measurements increases and the kernel scales become smaller. More concretely, for a smooth function  $f : \mathbb{R}^{d_i} \rightarrow \mathbb{R}$ , we have

$$\frac{1}{\epsilon_i} \sum_{k=1}^n L_i(j, k) f(s_k^{(i)}) = \frac{1}{2} \Delta_i f(s_j^{(i)}) + \mathcal{O}\left(\frac{1}{n^{1/2} \epsilon_i^{1/2+d_i/4}}, \epsilon_i\right)$$

where  $d_i$  is the dimensionality of the effective manifold underlying each measurement.

According to [52, Section 6], if in eq. (11) we use a variant of the Mahalanobis distance as the distance in the kernel, then the discrete graph Laplacians  $\mathbf{L}_1$  and  $\mathbf{L}_2$  approximate the Laplacian of the underlying parametric manifolds  $\mathcal{M}_1 = \mathcal{M}_x \times \mathcal{M}_y$  and  $\mathcal{M}_2 = \mathcal{M}_x \times \mathcal{M}_z$ , respectively, rather than their images via  $g$  and  $h$ . In [53, Section 3] the authors further investigated the product manifold:  $\mathcal{M}_1 = \mathcal{M}_x \times \mathcal{M}_y$  (resp.  $\mathcal{M}_2$ ), showing its explicit relation with the operators  $\Delta_x, \Delta_y$  (resp.  $\Delta_x, \Delta_z$ ) and deriving its spectrum. Their analysis is similar to the analysis we provide for the discrete graphs in B.

We emphasize that the continuous asymptotic analysis is presented in order to give meaning for the eigenvectors of  $\mathbf{K}_1$  and  $\mathbf{K}_2$ . Yet, the asymptotic analysis departs from  $\mathcal{P}(n)$  since the finite-dimension matrices become operators in infinite dimension.

In the remainder of this section, we present analysis of the continuous manifold setting in order to highlight the similarity to the analysis of the discrete graph setting presented in B. From [53, Section 3] we have the following two results.

**Proposition 11** *The operator  $\Delta_1$  is separable and can be written as*

$$\Delta_1 = \Delta_x + \Delta_y$$

where  $\Delta_x$  and  $\Delta_y$  are Laplace-Beltrami operators on the manifolds  $\mathcal{M}_x$  and  $\mathcal{M}_y$  respectively. Similarly, the operator  $\Delta_2$  can be written as

$$\Delta_2 = \Delta_x + \Delta_z$$

where  $\Delta_z$  is Laplace-Beltrami operator on the manifold  $\mathcal{M}_z$ .

**Proposition 12** *The eigenfunctions of  $\Delta_1$ , denoted by  $\varphi_1^{(k_x, k_y)}(x, y)$ , for any  $k_x, k_y = 0, 1, 2, \dots$  and  $x \in \mathcal{M}_x, y \in \mathcal{M}_y$ , can be expressed as the following tensor products*

$$\varphi_1^{(k_x, k_y)}(x, y) = \varphi_x^{(k_x)}(x) \varphi_y^{(k_y)}(y) \quad (52)$$

with the corresponding eigenvalues

$$\lambda_1^{(k_x, k_y)} = \lambda_x^{(k_x)} + \lambda_y^{(k_y)} \quad (53)$$

where  $\varphi_x^{(k_x)}(x)$  and  $\varphi_y^{(k_y)}(y)$  are the eigenfunctions of  $\Delta_x$  and  $\Delta_y$ , respectively, with the corresponding eigenvalues:  $\lambda_x^{(k_x)}$  and  $\lambda_y^{(k_y)}$ . The eigenvalues are sorted in descending order, i.e.  $1 = \lambda_x^{(0)} \geq \lambda_x^{(1)} \geq \dots$ . Similarly, the eigenfunctions of  $\Delta_2$ , denoted by  $\varphi_2^{(k_x, k_z)}$  for any  $k_x, k_z = 0, 1, 2, \dots$  and  $x \in \mathcal{M}_x, z \in \mathcal{M}_z$ , can be expressed as the following tensor products

$$\varphi_2^{(k_x, k_z)}(x, z) = \varphi_x^{(k_x)}(x) \varphi_z^{(k_z)}(z)$$

with the corresponding eigenvalues

$$\lambda_2^{(k_x, k_z)} = \lambda_x^{(k_x)} + \lambda_z^{(k_z)}$$

where  $\varphi_z^{(k_z)}(z)$  are the eigenfunctions of  $\Delta_z$  with the corresponding eigenvalues:  $\lambda_z^{(k_z)}$ .

The above propositions have analogous statements in the discrete graph case. Specifically, eq. (52) and eq. (53) in the continuous case are analogous to eq. (24) in the discrete case.

Similarly to the discrete setting, the Laplacians used here are normalized, i.e.  $\lambda_i^{(0,0)} = \lambda_x^{(0)} = \lambda_y^{(0)} = \lambda_z^{(0)} = 0$  and their associated eigenfunctions are the constant function 1. This implies that an eigenfunction  $\varphi_x^{(k_x)}$  of  $\Delta_x$  is common, i.e. it is an eigenfunction of  $\Delta_1$  with a corresponding eigenvalue  $\lambda_1^{(k_x, 0)} = \lambda_x^{(k_x)}$  as well as an eigenfunction of  $\Delta_2$  with the corresponding eigenvalue  $\lambda_2^{(k_x, 0)} = \lambda_x^{(k_x)}$ .

In addition, similar considerations imply that the eigenfunctions  $\varphi_1^{(k_x, k_y)}$  for  $k_y \neq 0$  are not common and that the eigenfunctions  $\varphi_2^{(k_x, k_z)}$  for  $k_z \neq 0$  are not common as well. This result is analogous to proposition 2 in the discrete case.

## Acknowledgements

This work was funded by the European Unions Horizon 2020 research grant agreement 802735.

## References

- [1] Bahador Khaleghi, Alaa Khamis, Fakhreddine O Karray, and Saiedeh N Razavi. Multisensor data fusion: A review of the state-of-the-art. *Information fusion*, 14(1):28–44, 2013.
- [2] Dana Lahat, Tülay Adalı, and Christian Jutten. Multimodal data fusion: an overview of methods, challenges, and prospects. *Proceedings of the IEEE*, 103(9):1449–1477, 2015.
- [3] Raffaele Gravina, Parastoo Alinia, Hassan Ghasemzadeh, and Giancarlo Fortino. Multi-sensor fusion in body sensor networks: State-of-the-art and research challenges. *Information Fusion*, 35:68–80, 2017.
- [4] Joshua B Tenenbaum, Vin De Silva, and John C Langford. A global geometric framework for nonlinear dimensionality reduction. *science*, 290(5500):2319–2323, 2000.
- [5] Sam T Roweis and Lawrence K Saul. Nonlinear dimensionality reduction by locally linear embedding. *science*, 290(5500):2323–2326, 2000.
- [6] David L Donoho and Carrie Grimes. Hessian eigenmaps: Locally linear embedding techniques for high-dimensional data. *Proceedings of the National Academy of Sciences*, 100(10):5591–5596, 2003.
- [7] Mikhail Belkin and Partha Niyogi. Laplacian eigenmaps for dimensionality reduction and data representation. *Neural computation*, 15(6):1373–1396, 2003.
- [8] Ronald R Coifman and Stéphane Lafon. Diffusion maps. *Applied and computational harmonic analysis*, 21(1):5–30, 2006.
- [9] Pierre Bérard, Gérard Besson, and Sylvain Gallot. Embedding riemannian manifolds by their heat kernel. *Geometric & Functional Analysis GAFA*, 4(4):373–398, 1994.

- [10] Peter W Jones, Mauro Maggioni, and Raanan Schul. Manifold parametrizations by eigenfunctions of the laplacian and heat kernels. *Proceedings of the National Academy of Sciences*, 105(6):1803–1808, 2008.
- [11] Yosi Keller, Ronald R Coifman, Stéphane Lafon, and Steven W Zucker. Audio-visual group recognition using diffusion maps. *IEEE Transactions on Signal Processing*, 58(1):403–413, 2009.
- [12] Mark A Davenport, Chinmay Hegde, Marco F Duarte, and Richard G Baraniuk. Joint manifolds for data fusion. *IEEE Transactions on Image Processing*, 19(10):2580–2594, 2010.
- [13] Roy R Lederman and Ronen Talmon. Learning the geometry of common variables using alternating-diffusion. *Applied and Computational Harmonic Analysis*, 44(3):509–536, 2018.
- [14] Ronen Talmon and Hau-tieng Wu. Latent common manifold learning with alternating diffusion: analysis and applications. *Applied and Computational Harmonic Analysis*, 2018.
- [15] Ofir Lindenbaum, Arie Yeredor, Moshe Salhov, and Amir Averbuch. Multi-view diffusion maps. *Information Fusion*, 55:127–149, 2020.
- [16] Tsuyoshi Ando. Concavity of certain maps on positive definite matrices and applications to hadamard products. *Linear Algebra and its Applications*, 26:203–241, 1979.
- [17] Rajendra Bhatia. *Positive definite matrices*, volume 24. Princeton university press, 2009.
- [18] Xavier Pennec. Intrinsic statistics on riemannian manifolds: Basic tools for geometric measurements. *Journal of Mathematical Imaging and Vision*, 25(1):127, 2006.
- [19] Xavier Pennec, Pierre Fillard, and Nicholas Ayache. A riemannian framework for tensor computing. *International Journal of computer vision*, 66(1):41–66, 2006.
- [20] Marc Arnaudon, Le Yang, and Frédéric Barbaresco. Stochastic algorithms for computing p-means of probability measures, geometry of radar toeplitz covariance matrices and applications to hr doppler processing. In *2011 12th International Radar Symposium (IRS)*, pages 651–656. IEEE, 2011.
- [21] Marc Arnaudon, Frédéric Barbaresco, and Le Yang. Riemannian medians and means with applications to radar signal processing. *IEEE Journal of Selected Topics in Signal Processing*, 7(4):595–604, 2013.
- [22] Suvrit Sra and Reshad Hosseini. Conic geometric optimization on the manifold of positive definite matrices. *SIAM Journal on Optimization*, 25(1):713–739, 2015.
- [23] Oncel Tuzel, Fatih Porikli, and Peter Meer. Pedestrian detection via classification on riemannian manifolds. *IEEE transactions on pattern analysis and machine intelligence*, 30(10):1713–1727, 2008.
- [24] Sadeep Jayasumana, Richard Hartley, Mathieu Salzmann, Hongdong Li, and Mehrta Harandi. Kernel methods on the riemannian manifold of symmetric positive definite matrices. In *Proceedings of the IEEE Conference on Computer Vision and Pattern Recognition*, pages 73–80, 2013.
- [25] Alexandre Barachant, Stéphane Bonnet, Marco Congedo, and Christian Jutten. Multiclass brain–computer interface classification by riemannian geometry. *IEEE Transactions on Biomedical Engineering*, 59(4):920–928, 2011.
- [26] Lipeng Ning. Regularization of covariance matrices on riemannian manifolds using linear systems. *arXiv preprint arXiv:1805.11699*, 2018.
- [27] Salem Said, Lionel Bombrun, Yannick Berthoumieu, and Jonathan H Manton. Riemannian gaussian distributions on the space of symmetric positive definite matrices. *IEEE Transactions on Information Theory*, 63(4):2153–2170, 2017.
- [28] Or Yair, Mirela Ben-Chen, and Ronen Talmon. Parallel transport on the cone manifold of spd matrices for domain adaptation. *IEEE Transactions on Signal Processing*, 67(7):1797–1811, 2019.
- [29] Vincent Arsigny, Pierre Fillard, Xavier Pennec, and Nicholas Ayache. Geometric means in a novel vector space structure on symmetric positive-definite matrices. *SIAM journal on matrix analysis and applications*, 29(1):328–347, 2007.
- [30] Ruiping Wang, Huimin Guo, Larry S Davis, and Qionghai Dai. Covariance discriminative learning: A natural and efficient approach to image set classification. In *2012 IEEE Conference on Computer Vision and Pattern Recognition*, pages 2496–2503. IEEE, 2012.
- [31] Alexandre Barachant, Stéphane Bonnet, Marco Congedo, and Christian Jutten. Classification of covariance matrices using a riemannian-based kernel for bci applications. *Neurocomputing*, 112:172–178, 2013.
- [32] Alexandre Barachant and Marco Congedo. A plug&play p300 bci using information geometry. *arXiv preprint arXiv:1409.0107*, 2014.

- [33] Maher Moakher. A differential geometric approach to the geometric mean of symmetric positive-definite matrices. *SIAM Journal on Matrix Analysis and Applications*, 26(3):735–747, 2005.
- [34] Carmeline J Dsilva, Ronen Talmon, Ronald R Coifman, and Ioannis G Kevrekidis. Parsimonious representation of nonlinear dynamical systems through manifold learning: A chemotaxis case study. *Applied and Computational Harmonic Analysis*, 44(3):759–773, 2018.
- [35] Ronald R Coifman and Matthew J Hirn. Bi-stochastic kernels via asymmetric affinity functions. *Applied and Computational Harmonic Analysis*, 35(1):177–180, 2013.
- [36] Nicholas F Marshall and Ronald R Coifman. Manifold learning with bi-stochastic kernels. *arXiv preprint arXiv:1711.06711*, 2017.
- [37] Silvere Bonnabel and Rodolphe Sepulchre. Riemannian metric and geometric mean for positive semidefinite matrices of fixed rank. *SIAM Journal on Matrix Analysis and Applications*, 31(3):1055–1070, 2009.
- [38] Ricardo Gutierrez-Osuna. Pattern analysis for machine olfaction: a review. *IEEE Sensors journal*, 2(3):189–202, 2002.
- [39] Wouter H van Geffen, Marcel Bruins, and Huib AM Kerstjens. Diagnosing viral and bacterial respiratory infections in acute copd exacerbations by an electronic nose: a pilot study. *Journal of breath research*, 10(3):036001, 2016.
- [40] J Gutiérrez and MC Horrillo. Advances in artificial olfaction: Sensors and applications. *Talanta*, 124:95–105, 2014.
- [41] Alexander Vergara, Shankar Vembu, Tuba Ayhan, Margaret A Ryan, Margie L Homer, and Ramón Huerta. Chemical gas sensor drift compensation using classifier ensembles. *Sensors and Actuators B: Chemical*, 166:320–329, 2012.
- [42] Martin Holmberg, Fredrik Winqvist, Ingemar Lundström, Fabrizio Davide, Corrado DiNatale, and Arnaldo D’Amico. Drift counteraction for an electronic nose. *Sensors and Actuators B: Chemical*, 36(1-3):528–535, 1996.
- [43] Philip A Higgs, Rob Parkin, Mike Jackson, Amin Al-Habaibeh, Farbod Zorriassatine, and Jo Coy. A survey on condition monitoring systems in industry. In *ASME 7th Biennial Conference on Engineering Systems Design and Analysis*, pages 163–178. American Society of Mechanical Engineers, 2004.
- [44] Nikolai Helwig, Eliseo Pignanelli, and Andreas Schütze. Condition monitoring of a complex hydraulic system using multivariate statistics. In *2015 IEEE International Instrumentation and Measurement Technology Conference (I2MTC) Proceedings*, pages 210–215. IEEE, 2015.
- [45] N Helwig, E Pignanelli, and A Schütze. D8. 1-detecting and compensating sensor faults in a hydraulic condition monitoring system. *Proceedings SENSOR 2015*, pages 641–646, 2015.
- [46] Xiang Gao, Meera Sitharam, and Adrian E Roitberg. Bounds on the jensen gap, and implications for mean-concentrated distributions. *arXiv preprint arXiv:1712.05267*, 2017.
- [47] Shoshana Abramovich and Lars-Erik Persson. Some new estimates of the ‘jensen gap’. *Journal of Inequalities and Applications*, 2016(1):1–9, 2016.
- [48] Roger A Horn and Charles R Johnson. *Matrix analysis*. Cambridge university press, 2012.
- [49] Daniel Spielman. Spectral and algebraic graph theory. Unpublished, current version available at <http://cs-www.cs.yale.edu/homes/spielman/sagt>, N.D.
- [50] G David Forney. The viterbi algorithm. *Proceedings of the IEEE*, 61(3):268–278, 1973.
- [51] Ronald R Coifman and Nicholas F Marshall. Manifold learning with bi-stochastic kernels. *arXiv preprint arXiv:1711.06711*, 2017.
- [52] Amit Singer and Ronald R Coifman. Non-linear independent component analysis with diffusion maps. *Applied and Computational Harmonic Analysis*, 25(2):226–239, 2008.
- [53] A Singer. Spectral independent component analysis. *Applied and Computational Harmonic Analysis*, 21(1):135–144, 2006.